9-1-2018

Neutron Spectroscopy Using Rubberized Eu:LiCAF Wafers

Michael A. Ford

NEUTRON SPECTROSCOPY USING RUBBERIZED Eu:LiCAF WAFERS

DISSERTATION

Michael A. Ford, Captain, USAF

AFIT-ENP-DS-18-S-024

DEPARTMENT OF THE AIR FORCE
AIR UNIVERSITY

AIR FORCE INSTITUTE OF TECHNOLOGY

Wright-Patterson Air Force Base, Ohio

AFIT-ENP-DS-18-S-024

NEUTRON SPECTROSCOPY USING RUBBERIZED Eu:LiCAF WAFERS

DISSERTATION

Presented to the Faculty

Graduate School of Engineering and Management

Air Force Institute of Technology

Air University

Air Education and Training Command

in Partial Fulfillment of the Requirements for the

Degree of Doctor of Philosophy in Nuclear Engineering

Michael A. Ford, BS, MS

Captain, USAF

September 2018

AFIT-ENP-DS-18-S-024

NEUTRON SPECTROSCOPY USING RUBBERIZED Eu:LiCAF WAFERS

DISSERTATION

Michael A. Ford, BS, MS
Captain, USAF

Committee Membership:

COL B. E. O'Day, Ph.D.
Chair

J. W. McClory, Ph.D.
Member

B. F. Akers, Ph.D.
Member

A. Danagoulian, Ph.D.
Member

Abstract

With the increasing cost and decreasing availability of ^{3}He, there have been many efforts to find alternative neutron detection materials. Lithium calcium aluminum fluoride (LiCAF) enriched to 95% ^{6}Li doped with europium was evaluated here as a replacement material for ^{3}He, based on the absorption of thermalized neutrons by the ^{6}Li and subsequent energy release of the ^{6}Li(n,t)^{4}He reaction. Wafers 0.5 cm thick, consisting of LiCAF crystals in a rubberized matrix, were embedded with wavelength shifting fibers (WSF) and mated to silicon photo-multipliers (SiPMs) to measure the photon response in a flux of neutrons from a DD neutron generator. Excellent discrimination was realized between neutrons and gammas, and both pulse-height discrimination and pulse-shape analysis were explored. A Figure of Merit (FoM) of 1.03 was achieved. Custom electronics were built to bias the SiPMs, then amplify, filter, discriminate, and digitize the LiCAF/WSF scintillation photons, resulting in a digital pulse that can easily be counted with any microcontroller. After evaluation of the Eu:LiCAF, a portable ten-layer neutron spectrometer was fabricated from the rubberized wafers. A layer of high density polyethylene (HDPE) was used as a neuton moderator between each layer. Neutrons entering the spectrometer are downscattered and absorbed by the lithium in a wafer of rubberized Eu:LiCAF; the layer in which the absorption occurs is dependent on the incident neutron's energy. A library of neutron response curves was created using Geant4 and applied with the maximum entropy principle algorithm, MAXED, to unfold the experimentally acquired data. The spectrometer was commissioned using two DD generators and a ^{252}Cf source. This research demonstrated that Eu:LiCAF is a promising potential replacement for ^{3}He and shows excellent promise for neutron spectroscopy applications.

Acknowledgements

I would like to thank my wife and kids for always showing me the true meaning to life. When things get busy, it's easy to get caught up in the laundry list of things-to-do and I am so thankful to have you all to pull me back down to Earth. I love you.

Michael A. Ford

Table of Contents

Page

Page

List of Figures

Figure Page

List of Tables

NEUTRON SPECTROSCOPY USING RUBBERIZED Eu:LiCAF WAFERS

I. Introduction and Research Objectives

The goal of this research was to design and build a neutron spectrometer capable of detecting neutrons in the energy range of 1-10 MeV. Neutron spectroscopy is a historically difficult task because of the low probability of neutron interaction with most materials, especially at high energies. The detection material used herein is Eu:LiCAF (europium doped lithium, calcium, aluminum fluoride). The construction and testing of a neutron spectrometer utilizing Eu:LiCAF will be discussed. This work incorporates a novel material (LiCAF) with silicon photomultipliers (SiPMs), wavelength shifting fibers, and custom electronics to develop a hand-portable neutron spectrometer.

LiCAF has promising material properties that potentially makes it a good alternative to ^{3}He for neutron detection. In September 2015, the Pacific Northwest National Laboratory (PNNL) performed an independent evaluation of the performance characteristics of Eu:LiCAF for the Tokuyama Corporation of Japan. In particular, there were five characterization measurements studied: neutron detection efficiency as a function of flux and source types, efficiency of neutron response as a function of source moderation, sensitivity of neutron detection at 2-meter reference distance, gamma insensitivity measurements, and the Gamma Absolute Rejection Ratio for neutrons (GARRn).

Using a 100 cm $\times$ 26 cm large rubberized Eu:LiCAF detector 3 cm thick, PNNL determined the average absolute efficiency for neutrons from bare and moderated ^{252}Cf at 2m of 1.01 $\pm$ 0.09 and 1.54 $\pm$ 0.23 cps/ng respectively [8]. The Eu:LiCAF

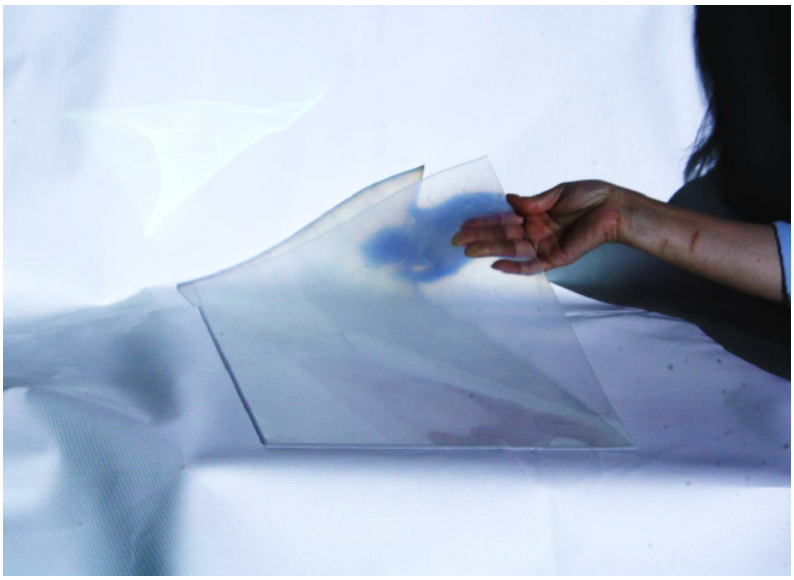

Figure 1. Flexible sheet of rubberized Eu:LiCAF. The LiCAF is non-hygroscopic, can be made into any shape, and has excellent transparency to its own scintillation light [1].

detector was also found to have an average intrinsic gamma-ray efficiency of 2.57 $\times 10^{-7} \pm 5.47 \times 10^{-9}$ over 10, 15, and 30 mR/h exposure rates and a GARRn of 1.01 $\pm$ 0.6%. The other test parameters will be discussed later in this document. Initial testing from PNNL showed that the Eu:LiCAF wafers have desirable characteristics for use in neutron spectroscopy.

Tokuyama produces Eu:LiCAF detectors with a solid-crystal or with ground crystals in a rubberized matrix. This research used ground crystals in a rubberized matrix due to cost advantages and neutron/gamma discrimination advantages (to be discussed later in this document). Rubberized Eu:LiCAF consists of a rubber composite with ground-up Eu:LiCAF crystals with an average diameter of 200 μm suspended throughout. The LiCAF material specifications (to include cerium doped LiCAF not used in this research) are shown below in Table 1, and a picture of the rubberized Eu:LiCAF sheet is shown in Fig. 1. Since light collection in a scintillation based neutron spectrometer is one of the most significant challenges, europium doped

LiCAF's eight-times larger light output provides a significant performance advantage over Ce:LiCAF. A second advantage of using the Eu:LiCAF is that the longer wavelength of its emission photons (360-390 nm) better matches common photomultiplier technology, including SiPMs.

1.1 Motivation

Neutron spectroscopy has been studied for decades. It has many applications, including several in the national defense realm. The Department of Homeland Security's (DHS) Transformational and Applied Research (TAR) Directorate's Research and Development portfolios provided five main detection research areas in the latest report to the Government Accountability Office, as outlined in Table 2: algorithms and modeling, materials development, neutron detection, radiation detection techniques and shielded detection.

This research directly addresses all five DHS TAR portfolio focus areas. In alignment with the algorithms and modeling focus, the Eu:LiCAF was modeled in both Geant4 and MCNP6, and efforts were made to model the optical photons in Geant4. Very little literature is available for modeling of optical photons in Geant4 [9, 10, 11]. In support of the materials development focus area, this research tests and characterizes a novel material for neutron detection in a gamma-rich environment. A website (scintillator.lbl.gov) was created by Stephen Derenzo, Martin Boswell, Marvin Weber,

Table 1. Selected properties of LiCAF. Adapted from Tokuyama Brochure [4, 5].

	Ce:LiCAF	**Eu:LiCAF**
Light Yield (photons/neutron)	5,000	40,000
Decay Constant (ns)	40	1,600
Luminescence wavelength (nm)	280-320	360-390
Transparency (at 10mm thickness)	>90%	>90%

Table 2. DHS' Transformational and Applied Research (TAR) Directorate's Research and Development Portfolios; five main radiation detection research areas to support efforts to find and identify Special Nuclear Material and other potential radioactive threats [6].

Portfolio	Description
Algorithms and modeling	Investigates innovative data processing and analysis techniques to enhance the ability to detect, locate, track and identify potential threats across a broad range of environments; utilizes advanced simulation tools to support personnel training.
Materials development	Investigates improved radiation detection materials, such as scintillators and semiconductors, which are materials that convert the energy of incoming particles to an electronic signal.
Neutron detection	Investigates improved neutron detection capabilities, including alternatives to the neutron detectors used in various portal monitor applications that rely on ^{3}He, which is scarce.
Radiation detection techniques	Investigates new approaches to improve the detection of threats and their localization and tracking based on readings of their unique radiological characteristics (signatures), known as passive detection.
Shielded detection	Investigates methods for detecting nuclear material that is shielded, especially methods using active detection techniques such as radiography and particle interrogation to produce detectable nuclear signatures.

and Kathleen Brennan at the Lawrence Berkeley National Laboratory with support from the Department of Homeland Security to provide the measured inorganic scintillation material properties [12]. Eu:LiCAF does not have an entry on this website. The neutron detection and spectroscopy research undertaken in this work directly supports the neutron detection focus area. Further, this research's focus on identifying the neutron source based on known neutron signatures directly supports the radiation detection techniques priority. Finally, while this research does not directly undertake identification of shielded neutron sources, the neutron spectrometer devel-

oped can be applied in follow-on research for such an effort. For example, for active interrogation, a neutron spectrometer could be used to detect fast or delayed neutrons from induced fission [13].

1.2 ^{3}He Shortage

The gold-standard for neutron detection has historically been ^{3}He. However a continually increasing demand for, and a shortage of supply of, ^{3}He has driven up cost and serves as an impetus to find alternative neutron detection materials [14]. Therefore, this research explores the potential for use of Eu:LiCAF as a cost effective alternative to ^{3}He for neutron detection.

1.3 Previous LiCAF Scintillation Research

Both Viererbl et al and the Pacific Northwest National Laboratory (PNNL) previously evaluated Eu:LiCAF [15, 8]. The Viererbl et al research focused on the ability to use Eu:LiCAF to discriminate signals from neutron and gamma radiation whereas PNNL evaluated the material for application as a neutron detector in a portal monitoring system. Evaluating only the pulse height, Viererbl et al. found that gamma radiation with energies above 1400 keV started to interfere with the neutron peak from a 0.5 cm thick wafer of Eu:LiCAF [15]. This limitation may have been due to the fact that the authors relied entirely on pulse-height discrimination without consideration of any other pulse discrimination or analysis. It should be noted that the discrimination capability for rubberized Eu:LiCAF is highly dependent on the density of the small scintillator crystal grains in the rubber, as well as detector geometry. As previously mentioned, PNNL found that the Eu:LiCAF neutron detector's sensitivity for a bare and moderated ^{252}Cf source is 1.01 $\pm$ 0.09 and 1.54 $\pm$ 0.23 cps/ng respectively with large rubberized Eu:LiCAF detectors measuring 100 cm long, 26 cm wide

and 3 cm thick [8]. This is approximately 40-60% of the neutron detector sensitivity requirement suggested for portal monitors [16].

Sugimoto et al demonstrated that Eu:LiCAF can be used to discriminate between neutrons and gammas, and that the pulse height spectrum shows a clear neutron absorption peak [17]. Additionally, Watanabe et al [2] applied WSFs to rubberized Eu:LiCAF and used pulse-shape discrimination (PSD) to discriminate WSF scintillation events from the Eu:LiCAF scintillation events. It should be noted that integrating WSFs into the rubberized Eu:LiCAF offers a convenient way to extract the scintillation photons, but it also introduces a new scintillator medium which must be accounted for as the polystyrene matrix and organic phosphor WSFs act as plastic scintillators embedded in the Eu:LiCAF rubber. This work by Watanabe et al is directly applicable to this research. Their work supports Viererbl's and PNNL's results while also integrating WSFs. The work presented here furthers the body of Eu:LiCAF research by utilizing SiPMs in conjunction with WSFs for light collection, custom electronics to create a portable system, and creating and studying the use of the material for neutron spectroscopy applications. Prior to delving into this research effort, an explanation of why Eu:LiCAF was selected for this research and the relevant theory behind neutron moderation, detection, and scintillation are addressed.

II. Theory

This section explains why Eu:LiCAF was selected for this research, the theory behind neutron moderation and detection, and how discrimination is achieved in the rubberized Eu:LiCAF wafers.

2.1 Material

Any neutron spectroscopy detection technology must satisfy two basic criteria. Firstly, it must meet absolute and intrinsic neutron detection efficiency requirements. Secondly, it must maintain neutron detection requirements and while simultaneously providing a means to differentiate between neutrons and gammas, either by being insensitive to gammas or through some means of discrimination. Regarding gamma-ray detection, quantitative requirements are specified for the intrinsic gamma ray detection efficiency and the gamma ray absolute rejection ratio (GARRn) [18].

The GARRn measures the detector response in the presence of both a large gamma ray field and a ^{252}Cf neutron source configured for an absolute neutron detection efficiency measurement [18]. The GARRn is defined as the absolute neutron detection efficiency ($\epsilon_{abs,\gamma n}$) in the presence of both neutron and gamma ray sources, divided by the absolute neutron detection efficiency ($\epsilon_{abs,n}$)

$$\text{GARRn} = \epsilon_{abs,\gamma n}/\epsilon_{abs,n} \tag{1}$$

The absolute detection efficiency is the number of pulses recorded per minute of radiation quanta emitted by a source in a specific geometry and the intrinsic efficiency is the number of pulses recorded per number of radiation quanta striking the detector [19]. Correspondingly, the geometry of the detector and the source must be known. For a neutron detector, which consists of some detection medium plus a moderator,

it is assumed that the "detector" is defined as the entire moderated system for measurement of intrinsic efficiency [18]. The acceptance level for GARRn of a neutron detector would be 0.9 < GARRn < 1.1 at a 10 mR/h exposure rate (PNNL experimentally determined the GARRn of Eu:LiCAF to be 1.01 ±0.6%). Other material properties to consider are the neutron interaction cross sections, photon output, and the neutron/gamma discrimination properties.

LiCAF.

The Tokuyama Corporation provides LiCAF doped with either europium or cerium, both of which have an effective Z of 15 and density of 2.99 g/cm^3. There are a few primary differences between the dopants that led to Eu:LiCAF being chosen for this work. First, the light yield of Eu:LiCAF is approximately eight times that of Ce:LiCAF. The decay constant of Ce:LiCAF is 40 ns, while it is >1 μs for Eu:LiCAF. While in many detection applications (medical imaging, for example) a shorter decay constant is desirable, it is not a significant issue for this research or for many security-related neutron detection applications. This research will show that the longer decay time ended up being beneficial since it provided a means to differentiate between fast pulses emitted from WSF events and those occuring in Eu:LiCAF. Finally, the luminescent wavelength of the Eu:LiCAF is 360-390 nm as compared to the Ce:LiCAF at 280-320 nm. This proved beneficial for this research since the SensL C-Series silicon photomultipliers (SiPMs) used in this research have a peak sensitivity of approximately 425 nm where the photon detection efficiency (PDE) is 42% at an overvoltage of 5.0 V [20]. A combination of higher photon yield and longer emission wavelength for the europium doped LiCAF enabled superior light collection by the readout electronics.

Eu:LiCAF/rubber (2x10^{21} ^{6}Li/cm^3) was used throughout this work. The neutron

absorption of the rubber-matrix Eu:LiCAF is approximately 5% higher than ^{3}He at 10 atm for 25 meV neutrons [1]. More details on the detection efficiency of LiCAF are provided in Appendix H. It should be noted that the neutron absorption percentage is much larger for the pure Eu:LiCAF crystal, since it is largely dependent on the number of ^{6}Li atoms, but the cost of the material is an order-of-magnitude higher. The neutron absorption percentage of pure cerium or europium doped LiCAF crystal is ∼60% for a 1 mm thick sample (25 meV neutrons), whereas it is only ∼17% for the Eu:LiCAF/rubber used for this work.

One of the reasons LiCAF is an effective material for neutron detection is the presence of ^{6}Li. The Eu:LiCAF used in this research contained lithium enriched to 95% ^{6}Li. Thermal neutrons have a high cross section for absorption in ^{6}Li resulting in the following reaction:

$$^1_0\mathrm{n} + ^6_3\mathrm{Li} \longrightarrow ^3_1\mathrm{H}\ (2.73\ \mathrm{MeV}) + ^4_2\mathrm{He}\ (2.05\ \mathrm{MeV}). \tag{2}$$

Both the tritium and the alpha particles interact in the Eu:LiCAF crystal scintillator, emitting photons that are transported via the WSFs to the SiPMs, where a current is created. The current is then amplified and converted to a voltage signal, and subsequently filtered and converted to a digital signal using a comparator. The digital signals are then counted/recorded using a field-programmable gate array (FPGA) or microcontroller. Data collection from multiple layers of rubberized Eu:LiCAF, with varying amounts of neutron moderating material placed between the source and each Eu:LiCAF wafer provides the means for neutron spectroscopy. This research unfolds the resulting count data from each Eu:LiCAF wafer to determine the average energy of the incident neutron flux.

A disadvantage of Eu:LiCAF is the relatively low α/β ratio, which characterizes the relative light yield of the detector from heavy charged particles to electrons. The

difference between the ratio of absorbed energy and the light yield for the gamma radiation and heavy charged particles (HCP) is caused by the quenching dependence on the linear energy transfer (LET). The ratio for Eu:LiCAF is 0.2 [17]. This presents an issue for bulk Eu:LiCAF crystals, as the scintillation light created from the high-energy HCPs is approximately equivalent to that produced by a 1 MeV gamma that fully deposits its energy. The discrimination problem can be mitigated by controlling the geometry of the crystals (since the range of the fast electrons induced by gamma rays is significantly longer than the HCP range), or in the case of the rubberized Eu:LiCAF, controlling the size and density of the small Eu:LiCAF grains embedded in the rubber matrix (such that scattered photons have a mean free path much larger than the size of the crystals). Using a lower density of Eu:LiCAF in the rubber matrix is advantageous for discrimination purposes since it allows the fast electrons induced by gamma rays to easily escape the scintillator grain before depositing their full energy [2]. A drawback to the lower density of Eu:LiCAF crystals is the reduced neutron detection efficiency.

Each wafer of rubberized Eu:LiCAF scintillator used in this research is 10 $\times$ 10 cm $\times$ 0.5 cm thick. There are also 30 WSF fibers per side embedded crosshatched in both the X and Y axes directions through the wafer. Although the gamma/WSF signals are an undesirable side-effect of utilizing the wavelength-shifting fibers, scintillation pulses originating in the WSFs are on the order of nanoseconds. The large difference in timing properties between the gamma/WSF ($\sim$50 ns) and Eu:LiCAF scintillation events ($\sim$ 1 μs) enabled use of an active low-pass filter to discriminate between the two pulses.

2.2 Neutron Detection

The primary thermal neutron interaction mechanism in lithium results in energetic triton and alpha particles liberated in opposite directions. An important consideration with this interaction is where the interaction occurs in the crystal. For example, if the neutron absorption occurs near the edge of the material, there is a possibility that the reaction products may escape without creating sufficient photons for detection. In addition to photon generation in the crystal, there is also the issue of photon transport if the interaction happens in a small grain of LiCAF that is located near the edge of a rubberized Eu:LiCAF wafer. Essentially, the active area of the wafer is reduced.

Neutrons may interact anywhere within the Eu:LiCAF wafer. It should be noted that the photon production and collection depends on where in the detector the neutron interacts. Although it may appear that a thicker layer of neutron reactive material is ideal, the voltage signal measured is directly proportional to the number of photons collected. If the neutron reactive layer is too thick, the photons can be absorbed or scattered out before making it to the SiPM, hence not creating sufficient PM current for discrimination. This was considered when the optimal thickness of the Eu:LiCAF wafers was determined. Geant4 simulations were conducted to determine the optimal thickness of the Eu:LiCAF wafers. Simulations showed that 0.5 cm thick wafers offered significantly better light collection than 1 cm thick wafers. The thinner wafers allowed transport of the photons through the rubber matrix and down the WSFs to the SiPMs which creates a current typically proportional to the number of photons detected. The custom geometries and flexibility of the rubberized Eu:LiCAF, which would make use of traditional PMTs difficult to implement, make use of WSF's desirable. It should be noted that the WSFs can interact with gammas and neutrons similarly to plastic scintillation fibers [2]. However, Watanabe found that the spectra

obtained from the WSFs with and without the Eu:LiCAF in the presence of a ^{60}Co gamma source to be nearly the same. This indicates that the gamma interactions that occur in the Eu:LiCAF rubberized wafer are primarily due to the introduction of the WSFs.

2.3 Neutron Moderators

This research led to the creation of a layered neutron spectrometer. The concept is that faster neutrons will penetrate more layers of high-density polyethylene and rubberized Eu:LiCAF before being thermalized and detected, while less energetic neutrons will interact in the first few layers. The idea of the spectrometer is to perform the function of an array of Bonner Spheres of different diameters. But rather than using a Bonner Sphere array, in the case of a layered Eu:LiCAF neutron spectrometer, the moderator layers between the wafers slow the neutrons to thermal energies where they can then interact with the ^{6}Li with greater efficiency. Higher energy neutrons, which have smaller interaction cross sections, will penetrate more matter (more moderator layers) prior to thermalization and interaction in wafers further in the detector. Since the physical process is stochastic it is possible to use simulations such as Geant4 to estimate detection system behavior. An explanation of the neutron kinematics which is an important part of the underlying physics used in simulations is found in Appendix N.

2.4 Scintillation Theory

All scintillation detectors operate using the same basic principle: when radiation strikes the detector, it causes the detection medium to emit visible light photons, which can then be detected via a PMT or SiPM. One important aspect of a good scintillator is that it should be transparent to the wavelength of its own emission

to prevent self-absorption. In this case, LiCAF was doped with europium to produce longer wavelength scintillation light to which the crystal had greater optical transparency. A second important characteristic is that the scintillator should be "light-tight" to prevent external optical photons from creating noise or spurious signals. Thirdly, it should be constructed in a manner that allows collection of the optical photons produced. Finally, the scintillator should have a linear response such that the number of optical photons produced is proportional to the amount of energy deposited.

Two important properties of a scintillation medium are the decay time and the resolution. The decay time is a means of describing of how fast a crystal emits light after the absorption of radiation (either a gamma or neutron interaction). Many crystal materials show decay pulse shapes that are single or multi-exponential [21]. For a single-exponential pulse such as Eu:LiCAF which has only one scintillation mechanism, the decay time is the time it takes for the current generatred to decrease to a value $1/e$ of its initial amplitude.

The energy resolution of a scintillator detector system indicates how well it is able to distinguish different energy events. For the application considered in this research the energy resolution was not critical since the reaction products from neutron absorption in Eu:LiCAF always have approximately the same energy. However, it should be noted that the primary limitation on the energy resolution of a scintillator crystal is the number of photons detected by the photodetector. This number is subject to the Poisson distribution. A higher number of photons gives a lower relative uncertainty, and therefore a better energy resolution. A review of the current generated from scintillation photons is presented in Appendix O. For a given crystal with a known light output, the Poisson distribution results in a theoretical limit on the best energy resolution obtainable.

Pulse-Shape Discrimination Mechanisms in Eu:LiCAF.

An important consideration when using scintillators for neutron spectroscopy is how to effectively discriminate between gammas and neutrons. Several discrimination methods were explored. The most common discrimination methods are amplitude, or pulse-height discrimination, and pulse-shape discrimination (PSD). Another method that was also explored throughout this research is the time-over-threshold method (ToT). Time-over-threshold is semi-analogous to pulse-shape discrimination in that it allows the user to determine the difference between a gamma and a neutron based only on the shape of the pulse. However, the ToT method goes one step further by allowing application of a simple comparator. A comparator is an electronic device that determines if the incoming signal exceeds the threshold and sends out a simple signal for the duration that the signal exceeds the threshold. If, for example, a gamma has a very sharply peaked pulse, and the neutron has a very wide pulse, it is expected that the neutron's pulse will spend more time "over" the threshold that the user sets. A simple algorithm can be implemented to discriminate between the two particles using only the comparator signal.

Even though the relatively low density and low effective Z of the Eu:LiCAF wafers make the materials fairly insensitive to gamma interactions, it is still important to have the discrimination capability in the signal processor. It should be noted that there is no difference in the shape of the signal produced by a gamma or a neutron interacting in Eu:LiCAF, which explains why the Eu:LiCAF is not capable of PSD [1, 17]. In order to discriminate between the gammas and the neutrons in the LiCAF, there must be a different mechanism causing the properties of the scintillation light to vary between the two particles. For example, in CLYC (doped with Ce), PSD is possible because photons are generated by three different processes with varying decay times and the fastest of these (core-valence luminescence) only occurs due to

excitation by gamma rays. Therefore, the excited states generated within the crystal by gamma events will tend to decay faster and produce photons more rapidly than neutron events [22]. This will create a faster rise-time and decay-time for the gamma events. Eu:LiCAF, however, does not have two separate mechanisms for the gammas and the neutrons. It should also be noted that introducing the WSFs to the detector assembly creates the need to discriminate the faster WSF scintillation pulses from the much slower Eu:LiCAF pulses. This research uses custom electronics (discussed later) to do so.

Strong gamma ray fields may thwart neutron spectroscopy efforts due to Eu:LiCAF's poor α/β ratio. Fig. 2 shows the spectra of the solid crystal Eu:LiCAF interacting with ^{60}Co γs and ^{252}Cf neutrons [1]. Tokuyama Corporation also published a spectrum of the rubberized Eu:LiCAF, shown in Fig. 3. There appears to be better discrimination between the γs and the neutrons for the rubberized form of the material than for the solid crystal form. As shown in the figure, neutrons can be differentiated from ^{60}Co 1.3 MeV gamma-rays only by pulse height discrimination [1].

Although Eu:LiCAF does not have two separate scintillation mechanisms that would allow discrimination between a neutron or a gamma interacting in the medium, there is a significant difference in the amount of energy liberated in the material. Thermal neutron capture in ^{6}Li creates two HCPs that deposit 4.78 MeV. Due to the short range of HCPs in matter, this energy is absorbed in the scintillator material and causes emission of scintillation photons. The primary advantage of Eu:LiCAF for the detection of neutrons is that it is very insensitive to gammas because of the low-Z. This low sensitivity is due to the fact that most energetic photons that interact with the Eu:LiCAF will Compton scatter with mean free paths much larger than the crystal dimensions and will escape the crystal without depositing their full energy. It should also be noted that, depending on where the interaction takes place in the

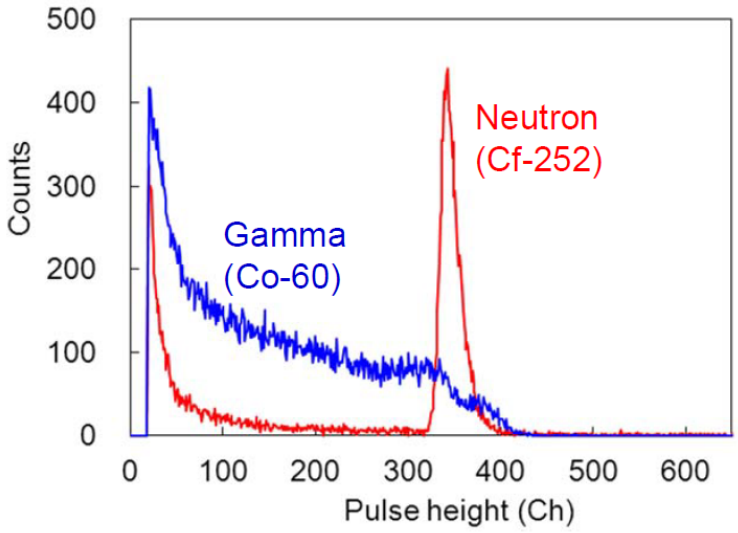

Figure 2. The spectra of both ^{60}Co γ-rays and neutrons from ^{252}Cf (approx 1 MeV). The slight overlap in pulse heights makes it more difficult to discriminate the neutrons from the gammas. [1] ©2014 with permission from Elsevier.

crystal, the range of energetic Compton scattered electrons may allow it to escape the scintillation crystal without depositing its full energy. In addition to the insensitivity of Eu:LiCAF to gammas, the ground-up crystals ($\sim$200 μm diameter) make it unlikely for gammas to deposit their entire energy in the rubberized Eu:LiCAF wafers.

Fast electrons from the gamma interactions have a longer path length than the HCP's created via thermal neutron absorption in ^{6}Li. These electrons may interact with the WSFs emitting a fast photon pulse (on the order of nanoseconds) in addition to the Eu:LiCAF scintillation photons (which are fewer than the number of photons from the neutrons, in most cases, and also much slower than the WSF scintillation photons). Watanabe et al. showed that the WSF response from a ^{60}Co source is nearly identical to the response with rubberized Eu:LiCAF wafer embedded with WSFs (see Fig. 4) [2]. This is indicative of the low gamma sensitivity for even the >1 MeV gammas emitted from the ^{60}Co. One thing to note is that the pulse height of the WSF scintillation events is significant and can surpass the height of the pulses

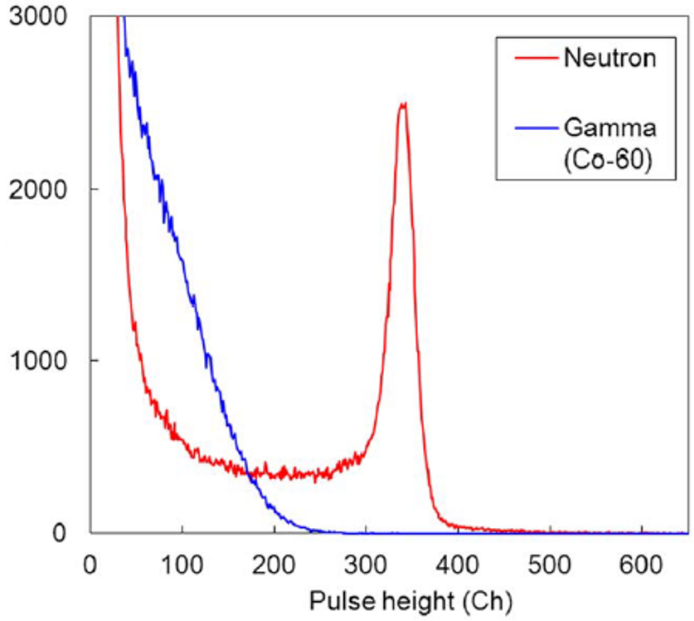

Figure 3. The spectrum of the rubberized Eu:LiCAF bombarded by both γs and neutrons. From this figure, it appears that the rubberized form of LiCAF is better at discriminating the neutrons and γs than the solid-crystal form. [1] ©2014 with permission from Elsevier.

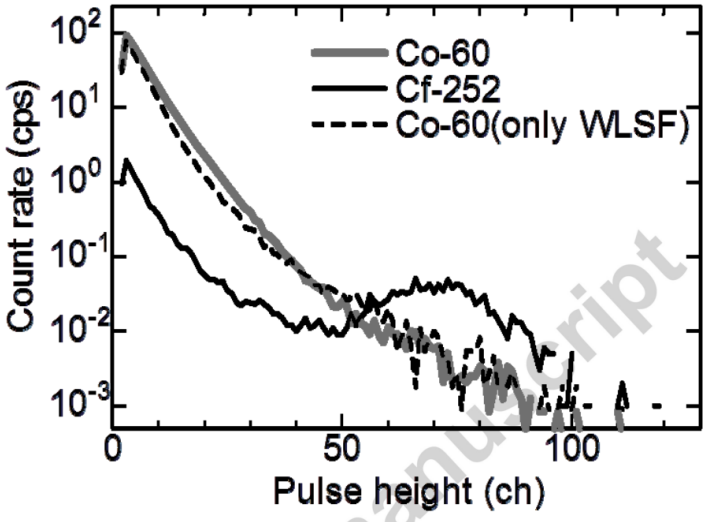

Figure 4. The WSF fiber scintillation signal from ^{60}Co, both with and without Eu:LiCAF, and also ^{252}Cf with Eu:LiCAF. From these results, the signal with and without the Eu:LiCAF is nearly identical, meaning that almost all of the gamma interactions occur in the WSFs. [2] ©2015 with permission from Elsevier.

from the neutron induced scintillation events in the Eu:LiCAF. The difference in timing properties of the WSFs and the Eu:LiCAF scintillation events, however, can be used to discriminate between the two events. Informed by a better understanding of the characteristics and properties of Eu:LiCAF and neutron spectroscopy, the next chapter will address modeling and simulation work that was completed.

III. Modeling and Simulations

Simulations were used for the unfolding of the neutron energy spectrum from the spectrometer count data, to determine the appropriate moderator thickness of the spectrometer, and also to ensure that the amplification and filtering circuit was properly designed. Simulations were necessary to model the response of the spectrometer and to reduce the need to conduct extensive experimental testing. The purpose of the spectrometer simulations during this research was twofold: first, they provided an indication that the spectrometer was operating as anticipated through comparison of experimental and simulated results. Second, the simulations were needed to generate a library of response curves that were used to unfold the resultant experimental spectrometer spectra. The goal was to create response curves such that if experimentally acquired neutron spectrometer counts is most similar to the response curve shown for 1.5 MeV neutrons (Figs. 5 and 6), the unfolding algorithm would report an incident average neutron energy of 1.5 MeV. This is an oversimplified example, as the neutron counts are very rarely "exact", however, the unfolding algorithm is capable of finding the "best" solution by comparing experimentally obtained data against a set of simulated response curves.

When performing the spectrometer simulations (using Geant4 and MCNP6), it was important to consider the requirements for the Maximum Entropy Deconvolution code (MAXED) spectrum unfolding. While spectrometer data was collected in the form of "neutron counts" per layer, unfolding was necessary to determine the energy spectrum of the incident neutrons. Proper and accurate unfolding of the neutron spectra required the simulations to match the experimental conditions as accurately as possible. It was assumed that photon production was linear with energy deposited, and that the fraction of photons collected remained approximately constant. This was a valid assumption since the scintillation mechanism remained constant and linear

regardless of the initial neutron energy (or originating particles).

3.1 Spectrometer Simulations

Simulations were used at several points in the spectrometer construction and evaluation process. Initially, simulations were conducted to determine the appropriate moderator thickness to accurately resolve neutrons in the range of approximately 1-10 MeV. If the moderator was made too thick, many of the neutrons would be stopped before penetrating several spectrometer layers of the spectrometer and insufficient data would be available to gain neutron energy information through unfolding. If the moderator thickness was too thin, the neutrons would not be sufficiently thermalized to interact with the ^{6}Li in the wafers which rely on a dominant thermal neutron capture cross section. Simulation results showed that moderator thickness between 1.25 and 3 cm were sufficient to thermalize neutrons in the region of interest.

An integral part of analyzing the spectrometer data, and unfolding the neutron energy spectrum after data collection, is accurately modeling the spectrometer and its surroundings. Two simulation packages were considered for the detector simulations: Geant4, which is based on a Monte Carlo algorithm [23, 24] and MCNP [25]. The code for the MCNP spectrometer simulations is included in Appendix D. Due to the structure of Geant4 simulations, the code is not provided here, but is available upon request. An overview of Geant4 is provided in Appendix J.

The simulation results from the two programs were statistically indistinguishable. Therefore, Geant4 results were used for the unfolding to capitalize on the results being outputted in ROOT. The simulation results for two moderator thicknesses (1.25 and 2.5 cm) were transferred to a format appropriate for unfolding with MAXED. 23 energy bins were used for unfolding, and the response libraries are shown in Figs. 5 and 6 for the 1.25 cm and 2.5 cm moderator thicknesses, respectively. The response

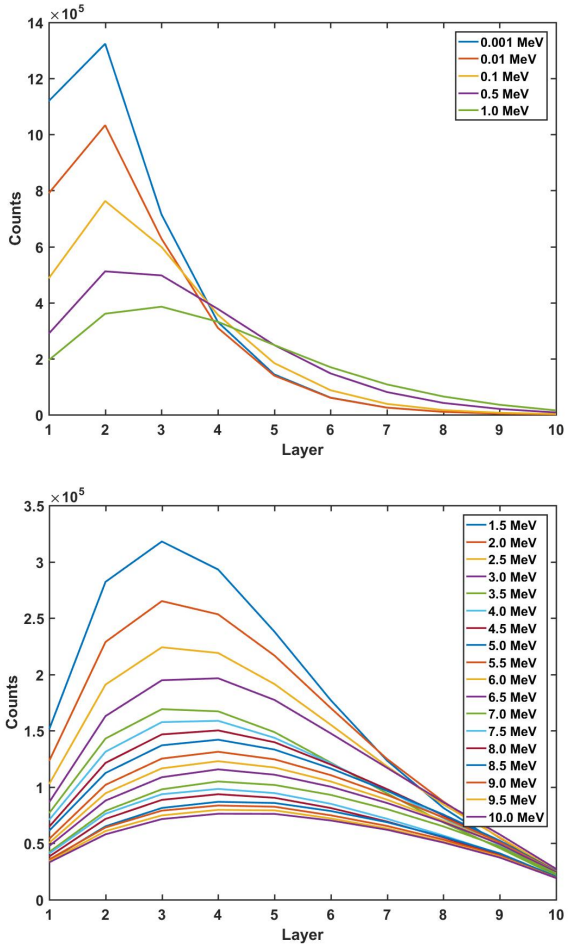

Figure 5. Response libraries created in Geant4 to model the spectrometer response for energies from 0.001 MeV to 10.0 MeV with a moderator thickness of 1.25 cm and the walls/DD generator support table at the Air Force Institute of Technology.

libraries are separated into two energy groups, the top of Figs. 5 and 6 shows energies from 0.001 MeV to 1.0 MeV and the bottom represents the range from 1.5 MeV to 10.0 MeV. The energies were divided this way to better show the response curves behavior from 1.5 MeV to 10.0 MeV. The limited differentiation at these higher energies proves to be a challenge when it comes to identifying neutron energies to within an order of magnitude, due to the statistical and systematic error associated with counting the scintillation photons from the Eu:LiCAF crystals.

While the spectrometer was surrounded by a layer of cadmium to reduce the effect

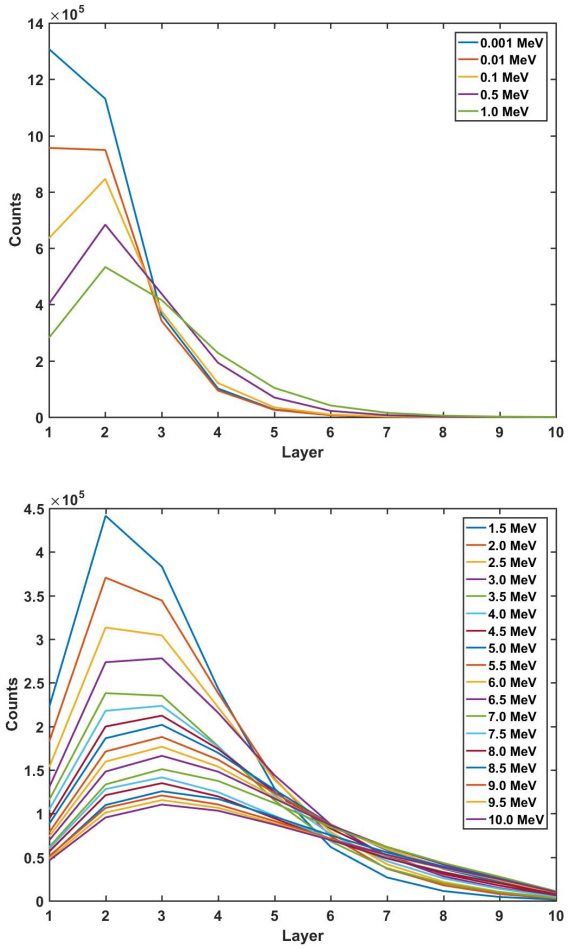

Figure 6. Response libraries created in Geant4 to model the spectrometer response for energies from 0.001 MeV to 10.0 MeV with a moderator thickness of 2.50 cm and the walls/DD generator support structure at the University of Michigan.

of neutron in-scattering from the environment around the DD generators, the walls were still modeled to provide a better representation of neutron interactions with each Eu:LiCAF layer. Fig. 5 represents not only a moderator thickness of 1.25 cm, but also the testing environment of the DD generator at AFIT, where data was taken with the spectrometer. Similarly, Fig. 6 incorporates the testing environment at the University of Michigan, where the 2.5 cm moderator spectrometer was tested.

Geant4 Results.

Within Geant4, it is possible to track an infinite number of parameters. For the purpose of the spectrometer, the most important parameter is the layer in which the neutron is absorbed in the ^{6}Li, creating an α-particle and a triton. A first check of the simulations was the energy of the particles being created. Figure 7 shows the α-particle creation energy for every α-particle initialized during the interaction of 1.0×10^5 2.45 MeV simulated neutrons. As shown in Appendix I, the expected α-particle energy is $\approx$2.055 MeV. The simulation appears to be consistent, hence providing confidence that the simulation physics is accurate. Similarly, Fig. 8, shows a histogram of the triton energy as the particles were created.

Several Geant4 simulations were conducted to ensure accurate modeling. Figures 9, 10, 11, and 12 show some of the initial Geant4 results of mono-energetic neutrons incident on a ten-layer spectrometer. The spectra shown in the figures shows simulations results represent expected spectrometer behavior. For example, it is expected that the initial low energy neutrons are all stopped in the first few layers, and that higher energy neutrons will penetrate further into the spectrometer.

Based on these simulation results, the spectrometer was constructed using two thicknesses of moderator. HDPE was cut into wafers 10 $\times$ 10 $\times$ 0.50 cm thick and 10 $\times$ 10 $\times$ 0.25 cm thick. Simulations were run at thicknesses of both 1.25 cm and 2.50 cm and the results of the simulations are shown in Figs. 13 and 14. The output of these simulations were used for unfolding the experimental spectrometer data.

3.2 Circuit Simulations

Each of the circuits used for the spectrometer were first designed and simulated using KiCad and LTSpice, respectively, to ensure proper gain and stability of the circuit.

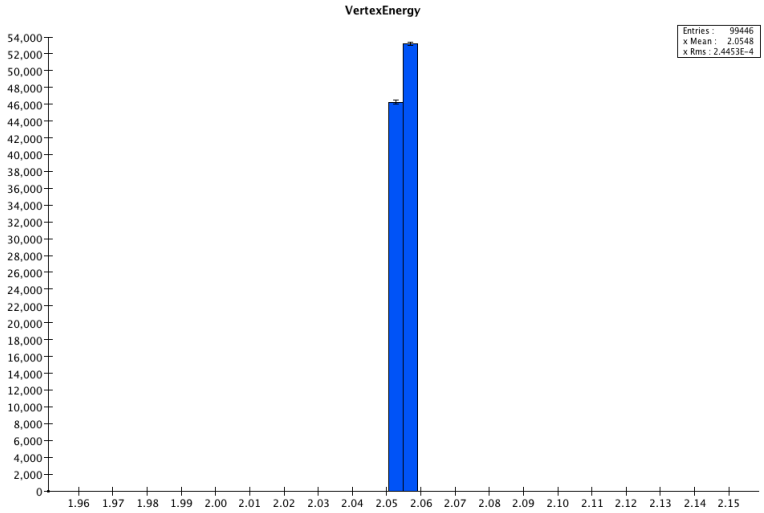

Figure 7. The Geant and ROOT output for a run with 100k thermal neutrons that interacted in a 1 cm layer of LiCAF producing 99446 α-particles with an average energy of 2.0548 MeV.

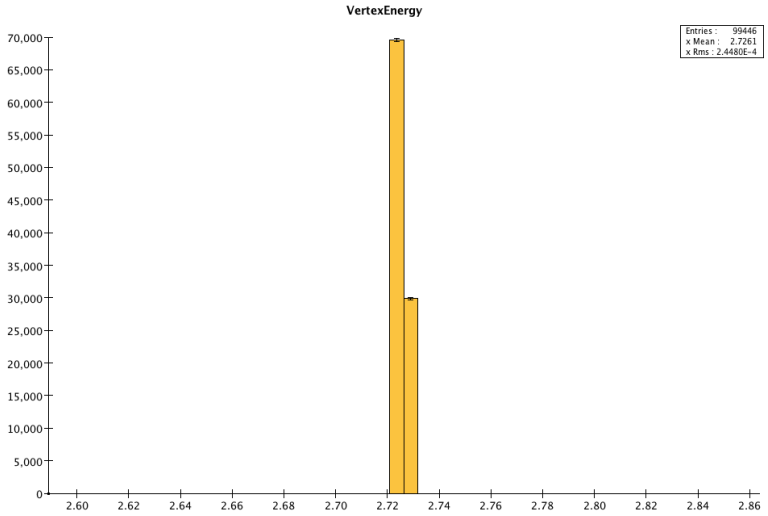

Figure 8. The Geant and ROOT output for a run with 100k thermal neutrons that interacted in a 1 cm layer of LiCAF producing 99446 triton particles with an average energy of 2.7261 MeV.

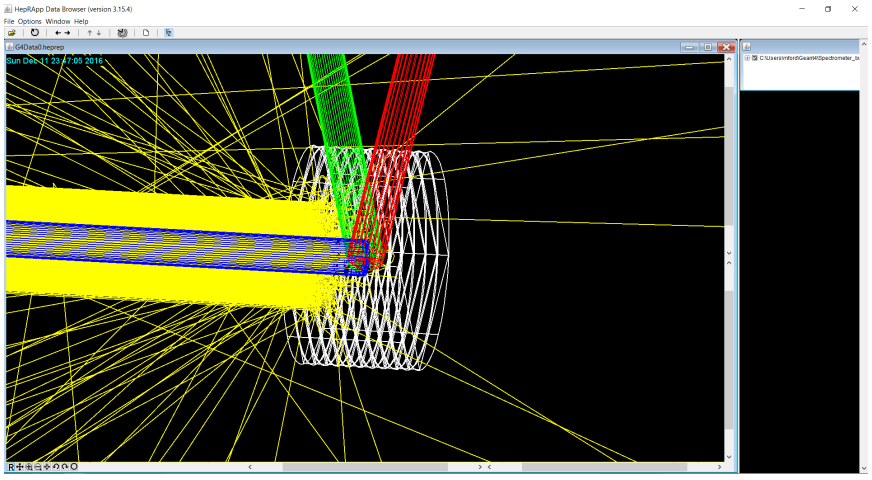

Figure 9. 1000 incident 0.025 keV neutrons interacting with a 10-layer LiCAF spectrometer. It can be seen that most of the neutrons are stopped within the first few layers.

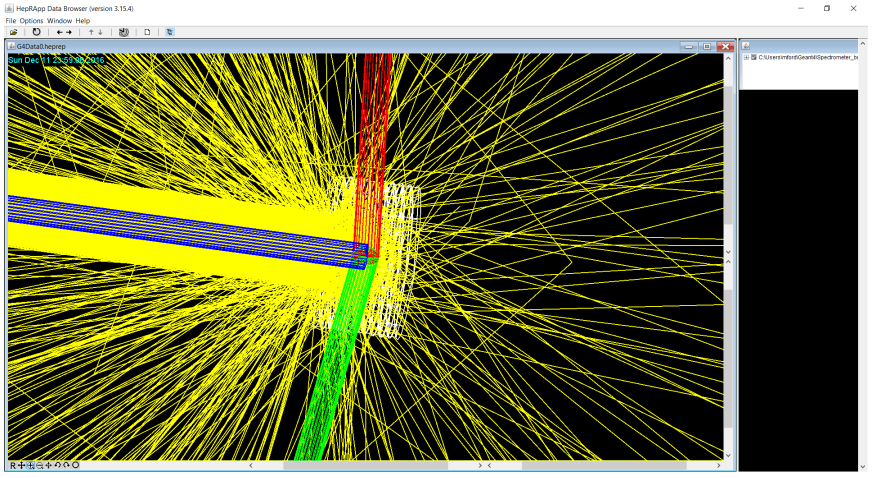

Figure 10. 1000 incident 0.025 MeV neutrons interacting with a 10-layer LiCAF spectrometer. It can be seen that most of the neutrons interact within the 10 cm thickness of LiCAF.

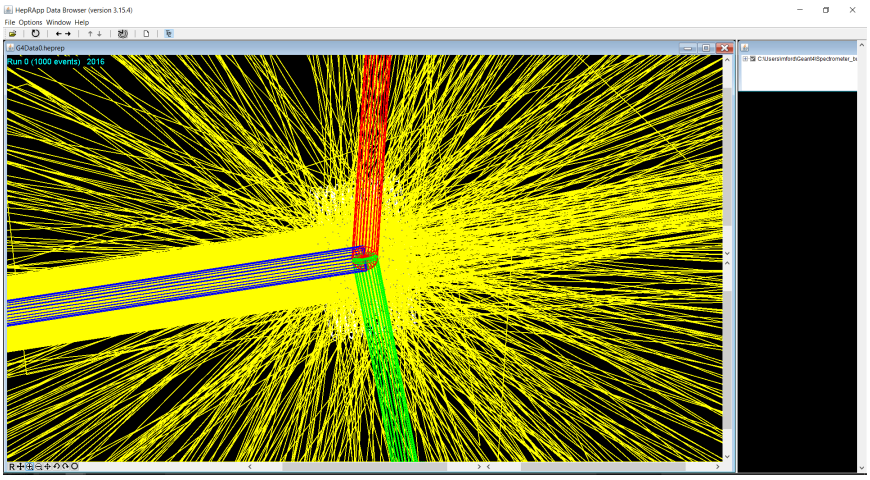

Figure 11. 1000 incident 2.5 MeV neutrons interacting with a 10-layer LiCAF spectrometer. It can be seen that while most of the neutrons still interact in the spectrometer, a significant shine-through flux is beginning to develop. The shine-through is an indication that the spectrometer is not thick enough to resolve the higher energy neutrons.

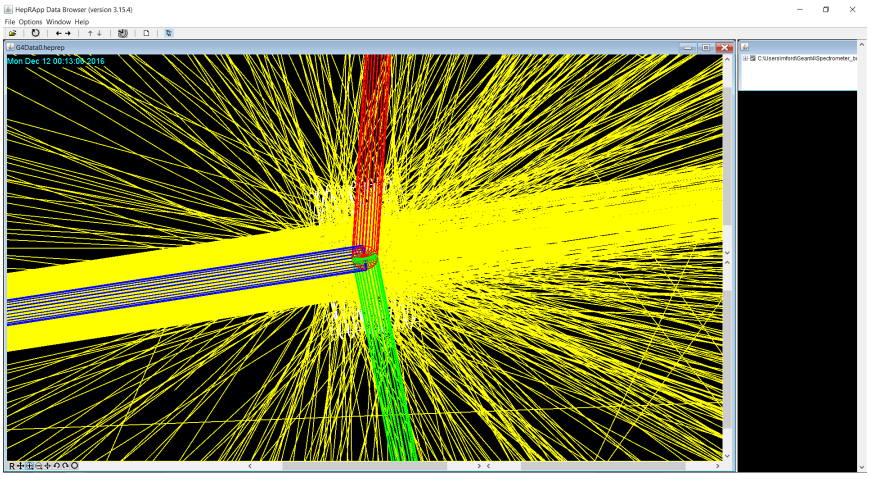

Figure 12. 1000 incident 10 MeV neutrons interacting with a 10-layer LiCAF spectrometer. It can be seen that most of the neutrons shine directly though the spectrometer.

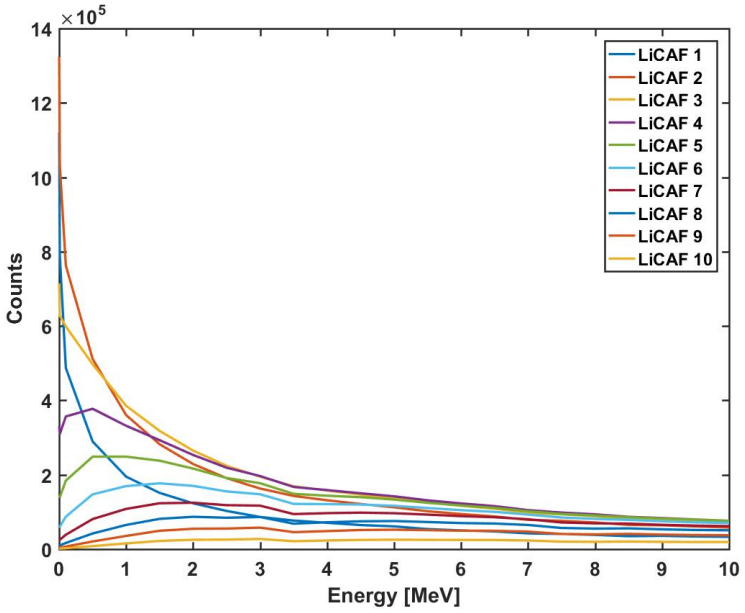

Figure 13. Geant4 response libraries by energy for 1.25 cm moderator thickness. This shows the response that is expected for each of the 10 spectrometer layers as a function of energy. This data was used in MAXED for unfolding of the spectrometer count data for the experiments performed at AFIT.

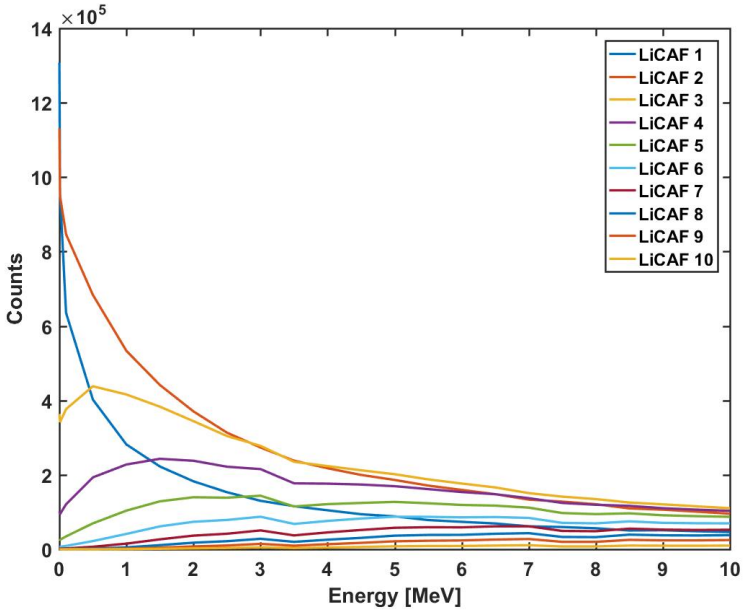

Figure 14. Geant4 response libraries by energy for 2.50 cm moderator thickness. This shows the response that is expected for each of the 10 spectrometer layers as a function of energy. This data was used in MAXED for unfolding of the spectrometer count data for the experiments performed at the University of Michigan.

Fig. 15 shows the simulated signal output of the electronic circuit using a BGO scintillation signal. The BGO signal was used as an input since it has scintillation properties similar to Eu:LiCAF. The circuit simulations ensured that the circuit was stable, without oscillations, and able to discriminate the faster WSF scintillation pulses while simultaneously able to drive a comparator at the output. MATLAB was used to analyze the active filter components. The timing property differences between fast WSF scintillation events and the much slower Eu:LiCAF scintillation events allowed selection of a filter to suppress the faster pulses. Reference Appendix A for the circuit board layout and the LTSpice simulation setup.

While only a first-order active low-pass filter was used for the initial experimental work here, an infinite impulse response (IIR) filter implementation was used in MATLAB to determine the optimal cutoff frequency (f_c) in order to get maximum amplitude separation between the gamma and neutron pulses, which have very different timing properties. Ideal pulses were loaded into MATLAB, and both signals (WSF and Eu:LiCAF scintillation events) were run through the filter at many cutoff frequencies to determine the optimal f_c. The MATLAB code used is shown in Appendix C. At the optimal cutoff frequency, there should be sufficient amplitude separation between the filtered WSF pulse and the filtered Eu:LiCAF pulse, allowing for use of a comparator and pulse-height discrimination. Results of the analysis are shown in Fig. 16. From the figure, the optimal cutoff frequency is 360 kHz. A range of frequencies from 1 Hz to 1.2 MHz was explored and the maximum amplitude of each pulse was found at each frequency iteration. Additional details of the the MATLAB analysis are provided in Appendix L. The next chapter discusses the construction of the spectrometer.

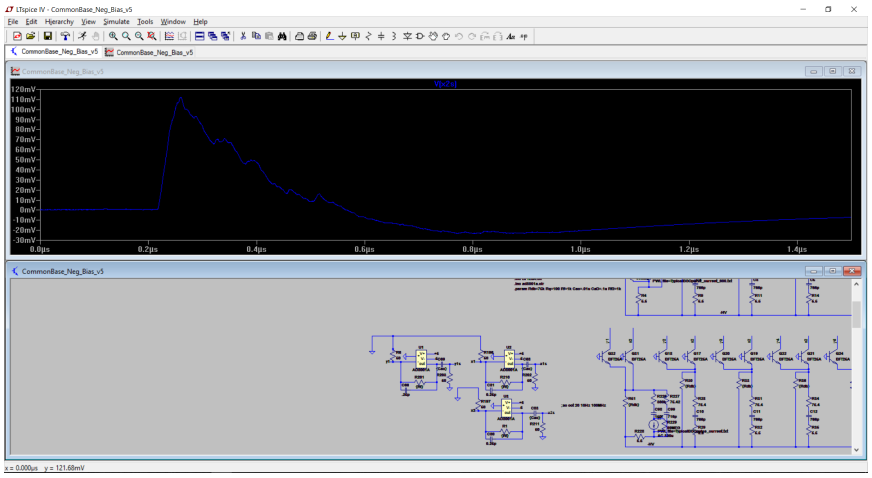

Figure 15. The circuit output as evaluated using LTSpice. This evaluation is extremely useful before fabrication a circuit; it also allows the user to optimize many of the passive component values.

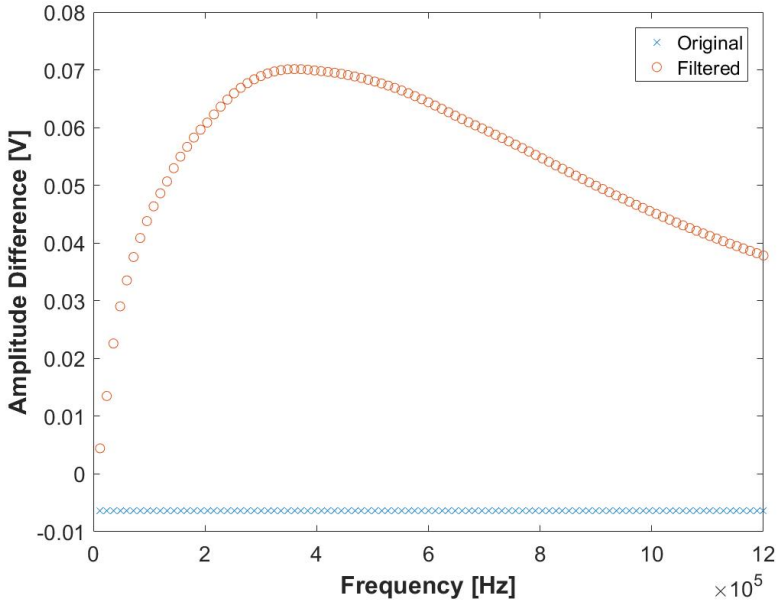

Figure 16. The amplitude difference of the WSF signal and the LiCAF pulse vs. filter cutoff frequency.

IV. Spectrometer Construction

Construction of the spectrometer involved building and testing the electronics, mating the electronics to the WSFs, arranging the Eu:LiCAF wafers in an alternating configuration with HDPE, and routing the comparator digital output signals to an FPGA.

Leo [26] was a valuable source for learning proper techniques for handling, gluing, mating, etc., scintillation materials. One important factor is determining the bias voltage of the amplification device for the photon detection, which applies to both traditional PMTs and the SiPMs used in this research. A SiPM is a single-photon sensitive light sensor that combines the practical advantage of a solid state sensor with performance characteristics that exceed those of a traditional PMT [27]. This solid state device demonstrates a strong correlation between the bias voltage and the output current. The effects on dark current to an increase in bias voltage is something that was considered. An increase in bias voltage produces an increase in the current output of the sensor, however this is also accompanied by an increase in the "noise", or dark current. A range of bias voltages from -28 V to -32 V was evaluated for the SensL-C SiPM used for this research. Optimal performance characteristics were found with a bias voltage of -29.5 V.

Another point in dealing with a scintillator is to minimize scatter of photons outside of the detector, which is typically achieved using an aluminum casing (or other highly reflective surface). It is desirable to lightly wrap the scintillator while maintaining a layer of air between the foil and the scintillator thereby minimizing the Brewster angle (θ_b):

$$\theta_b = \sin^{-1}\left(\frac{n_{out}}{n_{scint}}\right) \tag{3}$$

where n_{scint} is the index of refraction of the scintillator and n_{out} being that of the

surrounding medium. Total internal reflection occurs when all the light is reflected back into the scintillator. At incident angles less than θ_b, partial reflection occurs and the remainder transmitted; this is a significant problem because of the non-uniformity of the scintillator [26]. For example, where the interaction takes place in the medium determines the fraction of light output that reaches the PMT [26].

The spectrometer designed in this research is composed of alternating layers of moderating and detection materials. As previously discussed, the moderator serves to slow the neutrons down enough to be captured by the ^{6}Li (the neutron capture cross section is maximum at thermal neutron energies). The spectrometer is layered in a way that makes it similar to a set of Bonner Spheres with differing diameters. The primary concept of the neutron spectrometer is that lower cross sections at higher energies will allow faster neutrons to travel further in the spectrometer to thermalize. Upon thermalization, neutrons are likely to interact in the adjacent wafers. Thus, for an incident thermal neutron source, most of the neutrons will interact with the ^{6}Li and register counts in the first few wafers of the detector. For higher energy neutron sources, thermalization will take longer and neutrons will be registered in wafers toward the middle or end of the spectrometer.

Maintaining the portability of the detectors was a primary consideration in designing the electronics for the pulse counting and discrimination. Traditional PMTs were not used because of their size and power requirements. SiPMs offer similar specifications as PMTs without many of the disadvantages [28, 29, 30, 31]. Some of the advantages of using SiPMs are that they are extremely small, insensitive to magnetic fields, operate ideally with relatively low voltage (30 V), and the output signal can be easily amplified and filtered with basic electronics. A disadvantage of SiPMs is that their detection efficiency and gain are highly dependent on temperature. Due to the relative stability of environmental conditions during experiments, no cooling and/or

bias voltage control was used here to regulate the stability of the SiPMs, but this is something that should be considered for operation in a more variable environment.

The Eu:LiCAF spectrometer design used herein is shown in Figure 17. The photomultipliers selected, the SensL C-Series, are located on the circuit board (as shown). The C-Series low-light sensors feature an industry-leading low dark count rate combined with a high photon-detection efficiency that is extended much further into the blue part of the spectrum using a high-volume, P-on-N silicon process [20]. The C-Series SiPMs have performance characteristics that are similar to conventional PMTs with the added benefits of: low operating voltage, excellent temperature stability, robustness, compactness, output uniformity, and relatively low cost. Another product that was explored was the SensL J-Series. These SiPMs can be characterized by their photon detection efficiency (PDE) which is a measure of the sensor sensitivity and is defined as the percentage of incident photons that will go on to be amplified by the high internal gain and produce a measurable signal [27]. Although the J-Series has a PDE $\sim$ 10% higher, it was decided that the increased cost of the product did not warrant the slight increase in PDE. The PDE of the two products is shown in Figures 18 and 19.

Optical photon production and collection was one of the most important design parameters for the neutron spectrometer developed in this research. Measures must be taken to minimize the many inefficiencies – to include transport of photons from the Eu:LiCAF to the WSFs and propagation of the photons axially down the fiber– in the photon transport process. There are $\sim$40k photons/neutron generated in the Eu:LiCAF. It is important to consider whether the sensor has sufficient sensitivity at the operating wavelength to produce a measurable signal. The ideal situation is to produce scintillation light at the peak of the PDE curve. However, it should be noted that an advantage of SiPMs is the high responsivity even outside of the peak region.

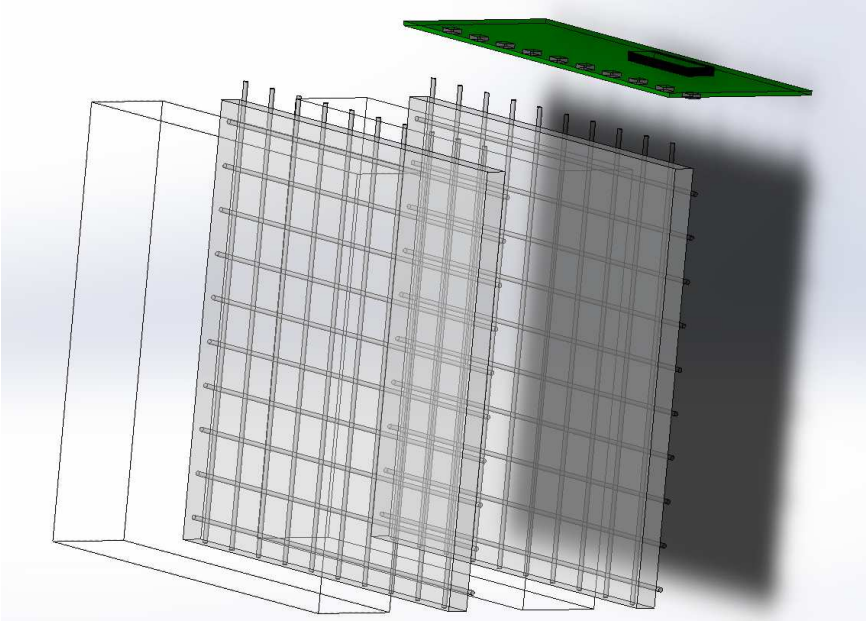

Figure 17. Decomposed model of the LiCAF spectrometer. This figure only shows the first two layers; however the alternating sequence of moderator/detector would continue for ten layers. In addition, the circuit board shown on top is also required on the side in order to get both X and Y axis data.

As shown in Table 1, the primary light output from the Eu:LiCAF is in the range of 360-390 nm, while the peak of the PDE chart is at about 425 nm. Where the peak is at approximately 41%, the PDE in the range of 360-390 nm is still fairly efficient at 32-37%. It should be noted that if the wavelength of the optical photons is too far out of the operating region, it is possible to use wavelength-shifting fibers to lengthen the wavelength to the appropriate range. The use of WSFs to better match the photon wavelength to the SiPMs will be discussed later.

Another consideration is mating the fibers or the crystals to the SiPMs [33]. In Fig. 17, the crosshatched fibers can be seen protruding from the Eu:LiCAF wafers, with 10 fibers per side running parallel to the X and Y axes for the Eu:LiCAF sample piece. Note here that while there are only 10 fibers per side for the sample wafer, the final spectrometer construction utilized Eu:LiCAF wafers with 30 fibers per side. A significant limitation of the photon transfer stems from insufficient light extraction

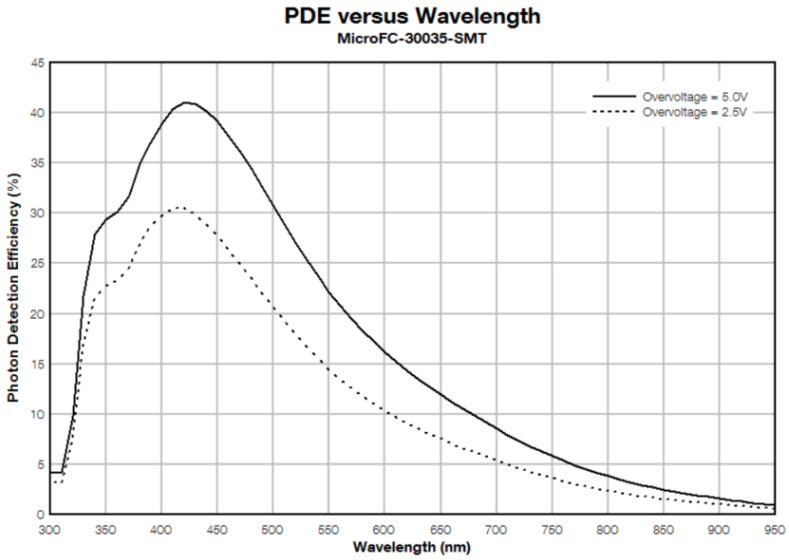

Figure 18. The photon detection efficiency of the SensL C-Series. The peak PDE is located between 400-450 nm, consistent with wavelength shifting fiber (WSF) output [20].

from the scintillators. Trapping of light leads to prolonged photon trajectories which cause increased absorption losses.

In current detectors, light trapping is caused by total internal reflection occurring at the interface of the high refractive index scintillator and the low index optical glue, which is used to couple the scintillator to the photo-sensor [33]. A promising means to increase the light extraction from high index media are slabs of 2D photon crystals (PhCs) which consist of layers that exhibit a bi-periodic modulation of the refractive index with geometric dimensions in the range of the wavelength of the incident light [33]. An example of this is shown in Fig. 20. The product that was used in the original testing of the sample Eu:LiCAF wafer is from Saint-Gobain Crystals, Silicon Grease (BC-630). While PhC slabs are not currently used here, this is a potential option for increasing photon extraction from the fibers.

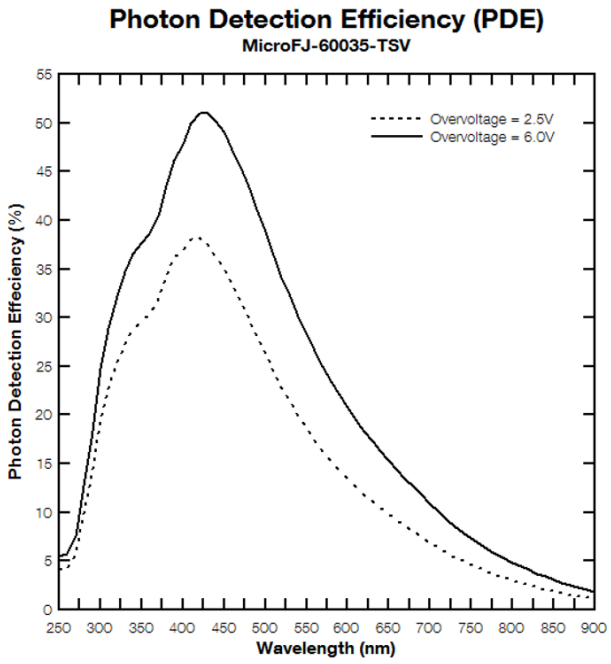

Figure 19. The photon detection efficiency of the SensL J-Series. The peak PDE for the J-Series is significantly higher than that of the C-Series [32].

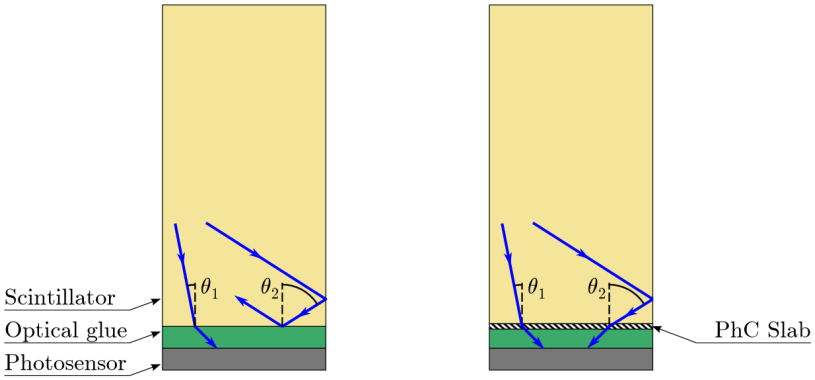

Figure 20. Proposed method to increase the light collection efficiency from the crystal to the SiPM using Photonic Crystals (PhCs) [33].

4.1 Circuit Design

One important goal of this research was to keep the design of the spectrometer minimized in space and weight in order to maintain portability. An important consid-

eration to keeping the design portable is minimizing the instrumentation as much as possible. To minimize the instrumentation, custom electronics were designed so that the entire spectrometer can be operated on a single voltage supply and an appropriate data acquisition system (laptop computer). Several designs were imagined. First, it is possible to use wafers with a layer of silicon photo-multipliers between each of the scintillating-moderating layers. This method works since the layers of SiPMs have minimal interaction with the neutrons and because the SiPMs can be easily made into an array. This design is shown on the right in Fig. 21. One major drawback of this design, however, in that it is expensive, requiring approximately 1000 SiPMs per layer with each SiPM costing approximately $30. An alternate design, shown on the left side of Fig. 21, allows for position information through the wafer by embedding wavelength-shifting fibers through the rubberized Eu:LiCAF wafers. The wavelength shifting fibers are actually embedded into the rubberized Eu:LiCAF and transport the scintillation photons where they can be converted to a current, then subsequently converted into a voltage signal via an amplifier. This current flow of the circuit is shown in Fig. 22.

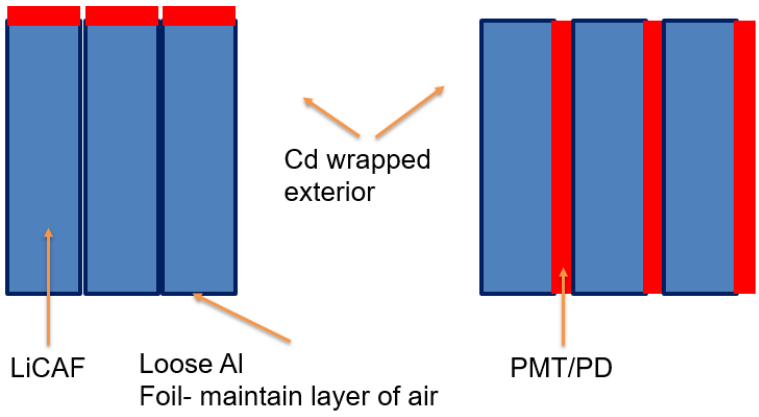

Figure 21. The two primary design proposals for the spectrometer geometry. The left shows the PMTs mounted on the sides (synonymous to the fibers extending out the sides) and the right side shows the SiPM arrays mounted between the detection layers.

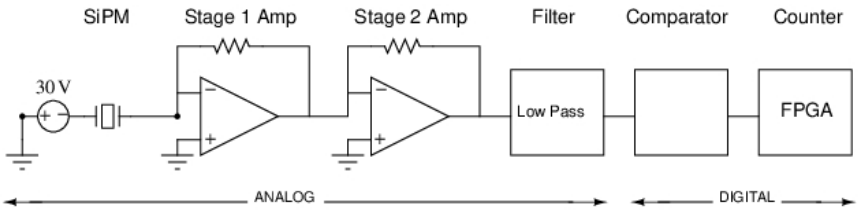

Figure 22. The circuit diagram for the LiCAF detection electronics. A current is generated in the SiPMs, which then gets converted to a voltage signal and is then subsequently filtered and turned into a digital pulse via a CMOS comparator.

The analog signal coming from the SiPM and then subsequently the amplifiers and filter goes into a comparator (MAX995)[34], where the amplitude of the signal will be compared to a threshold voltage, as shown in Fig. 22. Typically, in these situations, it is important to keep the threshold voltage above the noise level, but not so high that actual counts/events are missed. A vital aspect of this threshold voltage is its stability, because the threshold voltage for this application is on the scale of millivolts (mV). In a laboratory environment, it is common to use an external voltage supply to create a stable threshold voltage. However, for the desired application there is simply no room for a bulky voltage supply. This would be an important consideration for future introduction of this system to the field, but this research was performed in a lab environment so an external power supply was used. An additional consideration that must be accounted for if this technology were to be deployed for field use is that SiPM gains are typically susceptible to temperature changes. Both the bias voltage and threshold level could be affected.

In processing the signals, the comparator outputs a "digital high" in the event that the threshold voltage is exceeded, and a zero or "digital low" if the analog signal voltage does not exceed the threshold. Once the comparator outputs a digital high, this signal is input into a low-voltage differential signaling (LVDS) channel of the MAX10 FPGA where it can be decoded. Decoding determines from which comparator the signal originated and tallies the counts in the applicable region. Each

comparator had its own designated channel in the FPGA. Initially, there were only 10 signals in the X-direction and 10 signals in the Y-direction through the rubberized Eu:LiCAF, requiring 20 SiPMs and 20 FPGA channels per spectrometer layer.

4.2 Signal Readout – Wavelength Shifting Fibers

Another important consideration with this (and any scintillator) is the signal readout. WSFs (polystyrene matrix and organic phosphor, Kuraray B-3) were used to propagate the scintillation photons out of the transparent Eu:LiCAF rubber matrix. Ensuring the photons that make it into the fibers do not escape the fiber and also that the shift of the photon frequency is appropriate for the detection by the silicon photo-multipliers is an area of concern. Figure 18 shows that the optimal wavelength of the photons is approximately 425 nm and that the emitted photons from the scintillation events of the Eu:LiCAF are between 360 and 390 nm. The LiCAF wafers were delivered with the Kuraray/B-3 fibers, however, it looks like a better choice for Eu:LiCAF would have been B-2. The peak emission is 437 and 450 nm for the B-2 and B-3 fibers, respectively. The absorption peak is 375 and 351 nm for the B-2 and B-3, respectively.

The concept of using wavelength shifting fibers to reduce the number of necessary SiPMs was proposed by Kentaro Fukuda of the Functional Fluoride Group at Tokuyama [1]. This embedded WSF design for the prototype was chosen due to a significant cost savings as compared to using additional SiPMs. As previously stated, it is also possible to use an array of SiPMs to capture the photons. A disadvantage to using a wafer of Eu:LiCAF with embedded fibers is a reduction of lithium in the material (by volume), which is accompanied by a *small* decrease in the absolute detection efficiency.

The fibers must be mated to the SiPMs using optical grease to ensure optimal

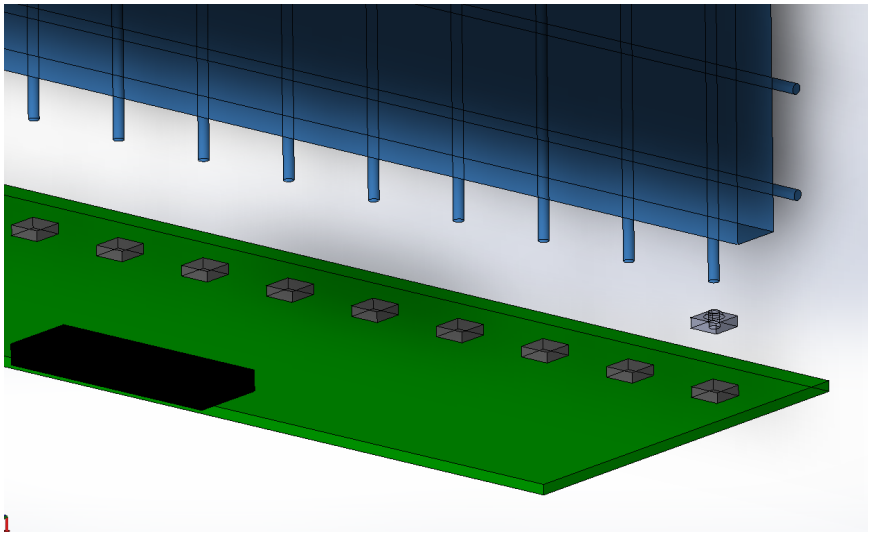

Figure 23. The LiCAF wafer mated to the circuit boards for the initial electronics testing.

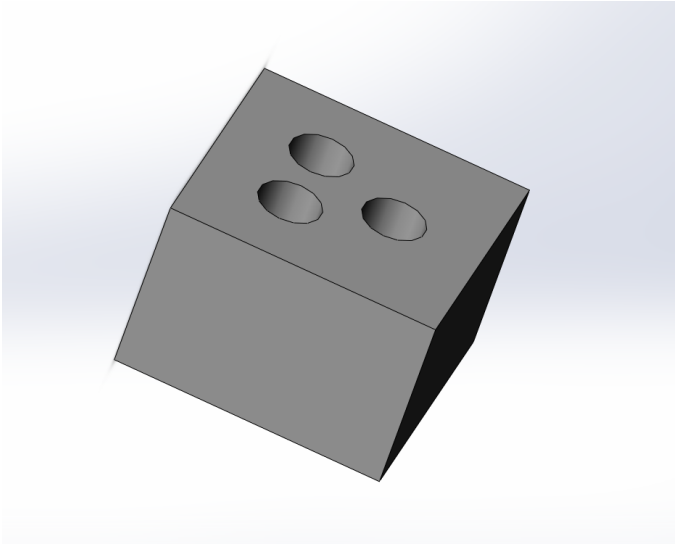

Figure 24. Top view of 3-D printed cap. The cap was designed in SolidWorks and fits tightly over the SiPMs, allowing three fibers to feed into a single SiPM.

propagation of the photons out of the fibers and into the SiPMs. This is depicted in Fig. 23, which shows only one fiber mating to the SiPM. Note this was only the case for the initial electronics testing. After it was verified that the electronics were operating as expected, new SiPM 3-D caps were printed that allowed three fibers to

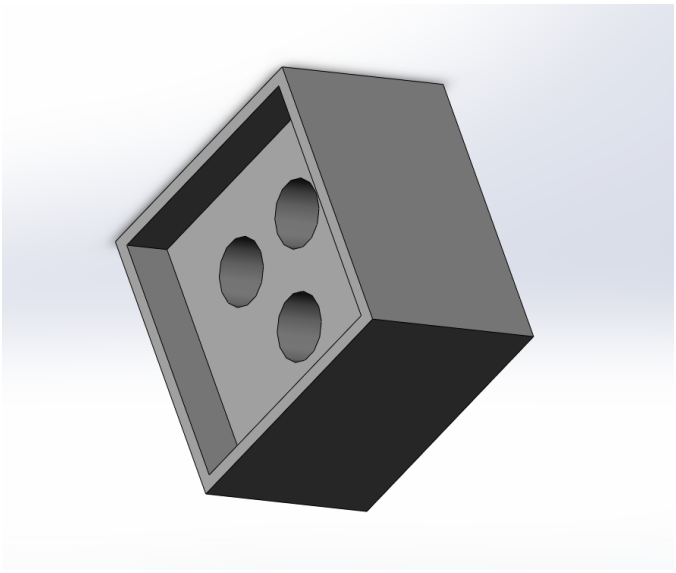

Figure 25. Bottom view of 3-D printed cap. The cap was designed in SolidWorks and fits tightly over the SiPMs, allowing three fibers to feed into a single SiPM.

be mated to each SiPM.

Figures 24 and 25 show the top and bottom view of the cap that fits tightly over the SiPMs. When installing the caps, the first step was to put a light layer of optical glue. Loctite 349 was used here; it is an acrylic, high viscosity, UV light cure adhesive which bonds and seals glass to glass or glass to metal components such as precision optical instruments/devices, furniture and industrial devices. Once the optical glue was applied, the next step was to gently insert three adjacent fibers into the cap, making sure that the fiber is seated all the way down to the SiPM. It was important to ensure that there are no air gaps between the fibers and the face of the SiPMs. After the SiPMs were firmly seated, another drop of adhesive was applied to the top of the cap. Once all 30 fibers were mated to the SiPMs, the assembly was placed under a UV lamp for approximately 24 hours to ensure a rigid assembly.

4.3 Circuit Testing

The first test with the electronics, regarding discrimination techniques, was to determine how well the electronics/crystals captured the energy spectrum of the 511 keV peak from ^{22}Na. The results of this are shown in Fig. 26. This was important to ensure that there is a linear response of the crystal/electronics.

The results of the initial tests with the BGO and the LYSO are as expected. Because of the quicker decay time and the higher light output of the LYSO, it was expected that the peak would have higher resolution. The BGO on the other hand, has a moderate light output but much slower decay time. The expected result is that the BGO would exhibit a lower resolution. The decay time for a BGO crystal is about 300 ns and the decay time for LYSO is 41 ns [21]. The results give good indications that the energy resolution is high enough for pulse-height or pulse-shape discrimination. A second trial run was accomplished to determine how well digital and/or post-analysis filters work to shape the output signal. The initial results of this testing are shown in Fig. 27.

Figure 27 shows both the Fourier transform of the spectrum and also the results of applying a Butterworth filter to the LYSO signal. The filter parameters are shown on the figure: first order, low-cutoff of 10 MHz, and a high-cutoff of 100 MHz. The 10 MHz cutoff reduces any slow-rising component. This would be effective if the goal was to separate two particles that interact differently with the crystal and have well-separated timing properties. The high-cutoff of 100 MHz is effectively to filter out the high frequency noise and increase the signal to noise ratio (SNR). Using the two test crystals, BGO and LYSO, the electronics and crystals configuration demonstrated that it is capable of resolving energy peaks with varying timing properties. This is an important capability for utilizing pulse-shape analysis (which will be discussed later in the paper).

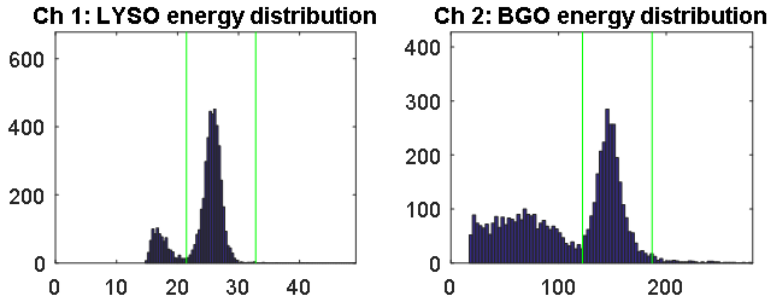

Figure 26. The output from the fabricated circuit board being evaluated with both BGO and LYSO crystals. The BGO was used because it has a slower decay signal with high light output (similar to LiCAF) and the LYSO was used to evaluate the timing performance of the circuit since it has a very fast decay time.

Once it was decided that the wavelength shifting fibers would be used to transport the photons to the SiPMs to created a current, and the appropriate circuit was designed and fabricated, the next step was testing it. At this stage, the Eu:LiCAF had not yet been acquired so the initial testing was performed using both BGO and LYSO crystals. Fig. 28 shows the setup that was used for the testing of the circuits. These crystals work well for the electronics testing because of their opposite characteristics. BGO has low light output and a long decay time, while LYSO emits a bright, fast, pulse of light. A comparison of the signals from the two crystals is shown in Figures 29 and 30.

A schematic of the pulse counter circuit was previously shown in Fig. 22. The timing and gain of each component was carefully chosen to ensure that proper pulse-shape filtering and amplification can be achieved. The first essential component is the Sensl C-Series SiPM, which has a microcell size of 35 μm and a peak sensitivity of 425 nm. The stage 1 is a simple npn transistor used to buffer the current (unity gain) from the SiPMs and the stage 2 amplifier is an Analog Devices AD8007 (ultralow distortion high-speed amplifier, 650 MHz, 1000 V/μs slew rate) with a gain of +2. Initial testing was conducted with the SensL evaluation board (MicroFC-SMA-300xx-

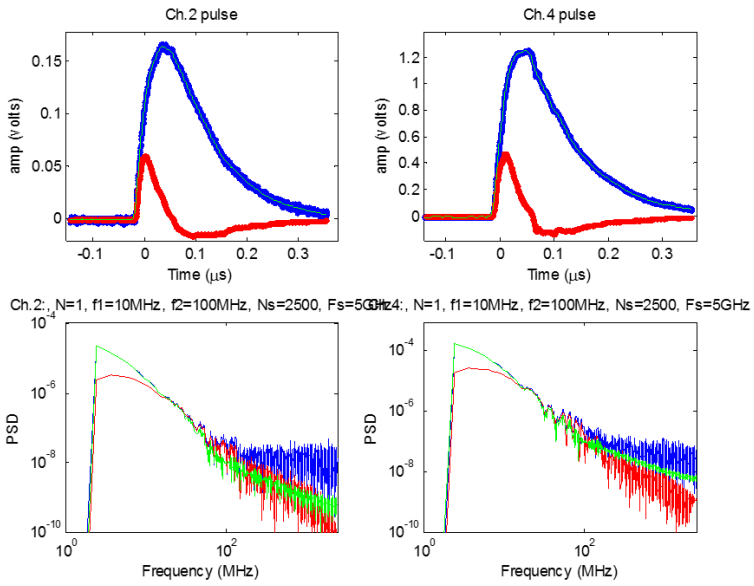

Figure 27. The fourier decomposition of the BGO waveform (bottom) and the original/filtered output (top) of the BGO signal. The Butterworth filtering accomplished here was done using MATLAB as a post-process. The MATLAB code used to filter the spectra is included in Appendix B.

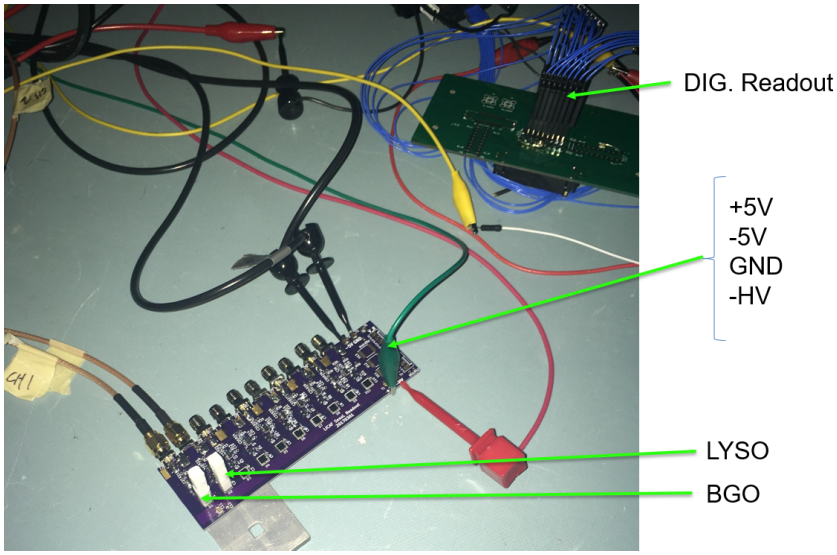

Figure 28. The fabricated circuit board being evaluated with both BGO and LYSO crystals. The BGO was used because it has a slower decay signal with high light output (similar to LiCAF) and the LYSO was used to evaluate the timing performance of the circuit since it has a very fast decay time.

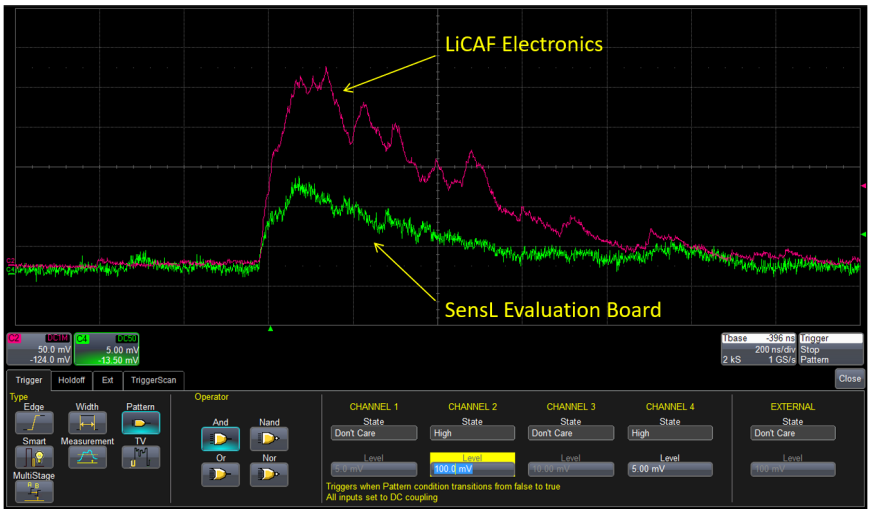

Figure 29. The analog test signal from a 4 mm × 4 mm BGO crystal after the circuit shown in Fig 22. The BGO signal has oscillations in the falling edge, likely resulting from the relaxing time of the photocells internal to the SiPMs.

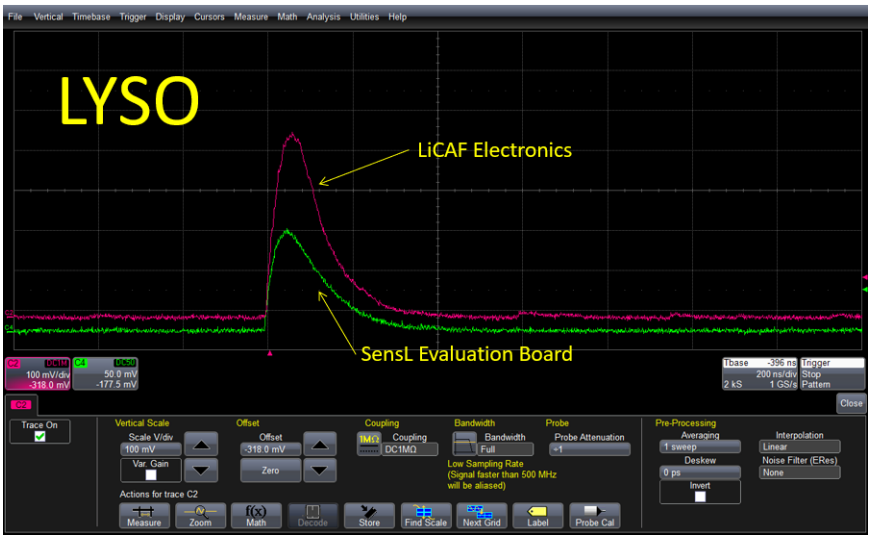

Figure 30. The analog test signal from a 4 mm × 4 mm LYSO crystal using both the SensL evaluation board, and the custom electronics.

35u) to ensure that the light emitted from the Eu:LiCAF would result in a sufficiently high signal-to-noise ratio (SNR) after the inefficiencies from both the WSFs and the photon detection efficiency of the SiPMs (maximum of 42%). Fig. 29 shows the results from comparing the SensL evaluation board to the custom circuit using a

BGO crystal and ^{68}Ge gamma source. A BGO scintillator was used for the early electronic testing because it has a well-documented light output from the 511 keV annihilation gammas that could be used for comparison in simulations. The original signal from the evaluation board (green trace, 5 mV/div) had a peak amplitude of about 10 mV, whereas the custom circuit using the AD8007 amplifier (red trace, 50 mV/div) had a peak amplitude of approximately 250 mV and a faster slew rate with the same BGO crystal.

The signal shown in Fig. 31 is collected at the output of the stage 2 amplifier; it then must go through a filter, comparator, and finally a counter. Fig. 31 shows the persistent oscilloscope traces of the output of the stage 2 amplifier (left column of scope image), and the right column of the scope image shows the comparator output due to the gamma interactions in the BGO. The digital output of Fig. 31 (right) is not in persistence mode and only shows a pulse each time the comparator threshold voltage is exceeded. The purpose of the filter after the amplifiers was to suppress the faster pulses in the rubberized Eu:LiCAF wafer and WSFs. The gamma/WSF pulses have a larger high-frequency component than the neutrons, thus filtering the faster pulses in conjunction with pulse-height discrimination allowed most of the gamma/WSF pulses to be rejected.

An active low-pass filter was developed using the Analog Devices ADA4857-1 Operational Amplifier. This amplifier was chosen because of its desirable properties: ultralow distortion, low power, low noise, and high speed. The next step after the filter was to perform pulse-height discrimination. This was done with the Maxim Integrated MAX995, high speed, low voltage comparator. The comparator outputs a digital pulse anytime the user-defined threshold was exceeded. Using a micro-controller or field programmable gate array, the rising edges of the comparator output can be counted to determine the number of neutrons that interacted with the Eu:LiCAF. The

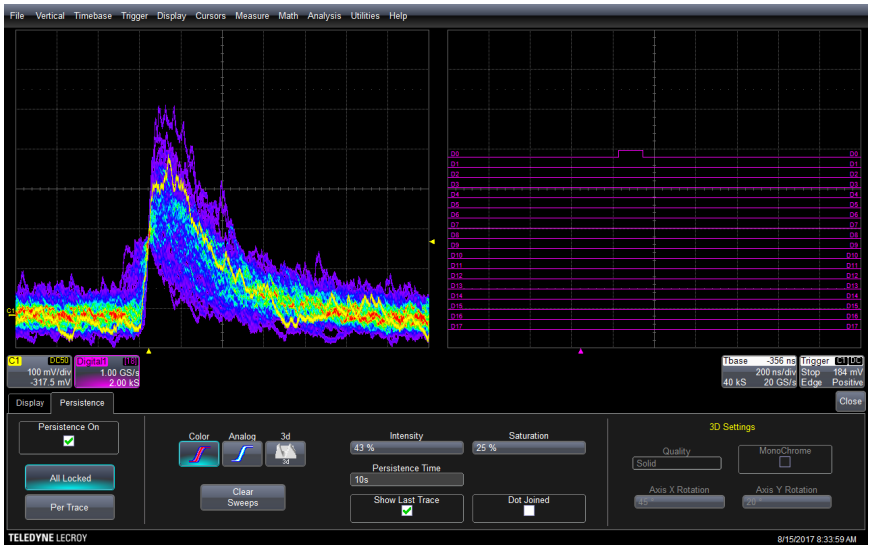

Figure 31. Persistent oscilloscope traces of electronic circuit mated to a 4mm × 4mm BGO crystal with a ^{68}Ge gamma source, and the output digital pulse from the MAX995 comparator.

comparator was setup in burst guard mode, which limits pulse pile-up. Counts were only recorded when the pulse signal amplitude exceeded the user-defined threshold.

After testing with the SiPMs, it was evident from the oscilloscope trace that there were oscillations in the signal from the long decay time of the light in the BGO crystal. This oscillatory nature was not seen in the LYSO crystals. The oscillations are likely from the size of the photocell in the SiPM. The recovery time, or decay time of the pulse, is primarily determined by the microcell reset period, given by the product of the effective capacitance of the microcell and the value of the quench resistor. Since the capacitance of the microcell will depend on its area, the reset time will vary for different microcell sizes. An additional factor that can affect the recovery time is the series resistance from the rest of the sensor that will be more significant in larger sensors [27]. These effects may be insignificant in lower flux neutron fields but would need to be considered in high flux environments.

4.4 Data Acquisition

Because of the large number of data channels associated with the data acquisition, an FPGA was used to count the neutron pulses. An Altera MAX10 FPGA offers secure on-die flash memory, instant-on support, an integrated analog-to-digital converter, programmable logic levels (PLLs) and high-density general purpose I/Os. It can be powered via a USB cable and fits in the palm of your hand. A main disadvantage of the FPGA is that it required firmware to be written, however the firmware is fairly basic in this case and was written in Verilog. The current firmware is setup so that for each neutron absorption that takes place in the spectrometer, the comparators will be triggered, sending a digital "high" signal to the FPGA. Once the signal is seen by the FPGA, it will send 1 byte (XXXX_XXXX) of data to a computer via Serial Peripheral Interface (SPI) with an encoded address depending on which I/O pin received the digital "high" signal. The firmware is operated on a 100 MHz internal clock and looks every 10 ns to determine if any of the channels has a "high" signal. If the channel is active, the firmware then waits until the next clock cycle to see if the same channel is still high, if it is, the signal gets counted as a single hit. If the channel is no longer active on the adjacent clock cycle, the count is discarded. This limits spurious signals or noise from getting counted as a signal. In addition to the noise rejection, the counter also discounts neutron hits of adjacent channels. For example, each layer of the spectrometer has 30 fibers, and these are grouped into sections of 3 fibers each, for a total of 10 SiPMs. If SiPM-2 receives a neutron "hit" (indicated by a comparator "high" signal), and the signal lasts for two clock cycles, and during the same two clock cycles, SiPM-3 receives a comparator "high" signal, then only one neutron count is tallied even though two valid signals were received. An overview of the basic counting algorithm is shown in Table 3. Table 3 is, by no means, inclusive. There are many physical situations that have not been

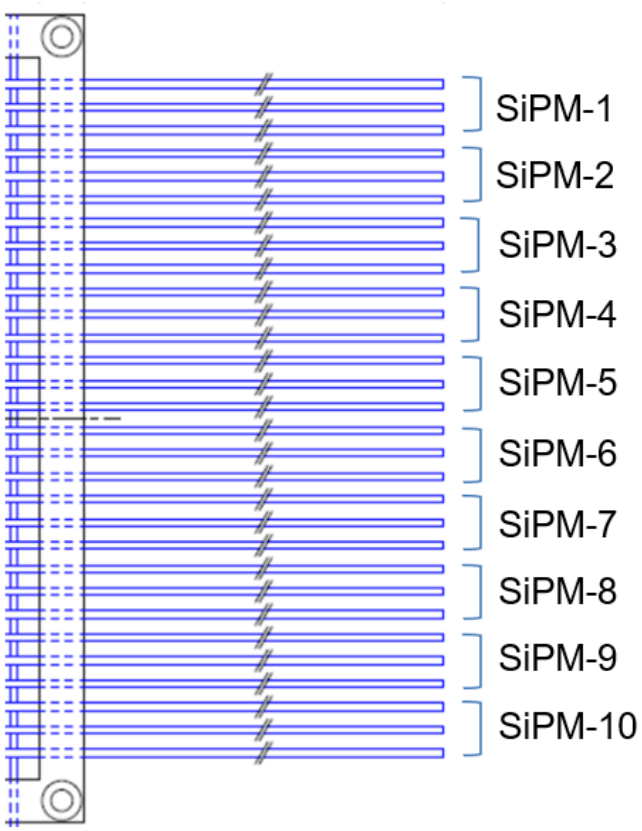

Figure 32. The numbering of the SiPMs for the firmware architecture.

covered, such as signal debouncing, however these situations are handled internally in the firmware. Fig. 32 shows how the SiPMs are numbered in the firmware.

Table 3. Firmware counting architecture.

Condition 1	Condition 2	Count? (#)
Hit in SiPM 2	1 CC (Clock Cycle)	0
Hit in SiPM 2	2 CC (Clock Cycle)	1
Hit in SiPM 2	Hit in SiPM 3	1
Hit in SiPM 2	Hit in SiPM 4	2

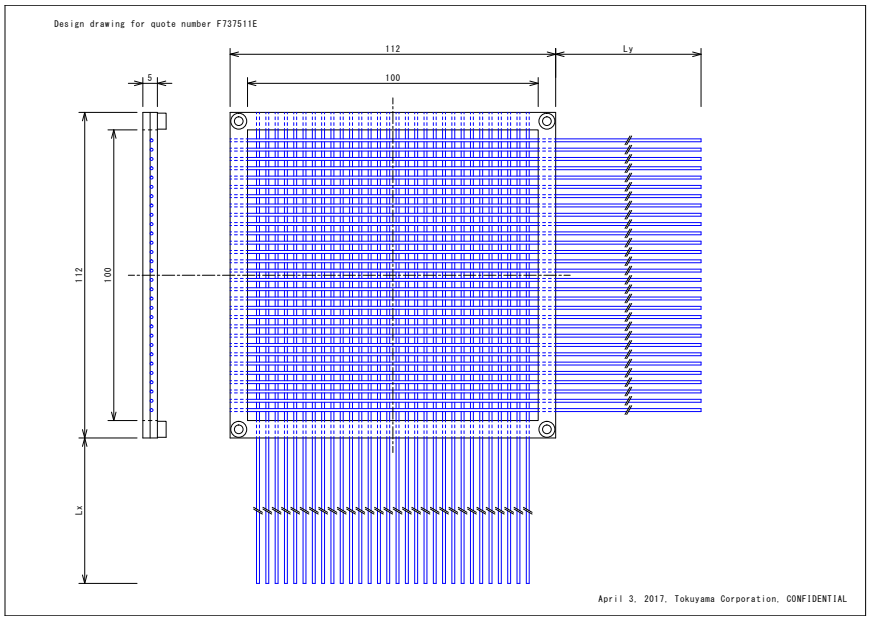

Figure 33. The design of the sample LiCAF piece (100 mm x 100 mm x 5 mm) with 30 wavelength shifting fibers in both the X and Y directions. The fibers were bundled in groups of three so that there are 10 readouts in both the X and Y axes.

4.5 Detector Calibration

Each 10 × 10 cm wafer of rubberized Eu:LiCAF was evaluated. The wafers were 0.5 cm thick and had WSFs embedded crosshatched along both the X and Y-axes. There were 30 one mm diameter fibers embedded on each axis (Fig. 33) to allow for position-dependent readout, and to provide a sufficient number of photons reaching the SiPMs. It is generally accepted that only about 1% of the wavelength shifted photons will reach the SiPMs after accounting for the collection efficiency and re-emission of photons along the axial direction of the fibers [35]. A light-tight box was placed around the entire wafer/electronics assembly to minimize the number of ambient photons interacting with the SiPMs, which served to keep the signal-to-noise ratio as large as possible. To further reduce the number of ambient photons that have the potential to decrease the SNR, caps were 3-D printed out of a black nylon (PA 11) to fit tightly over the SiPM, while only having one extrusion at the top to

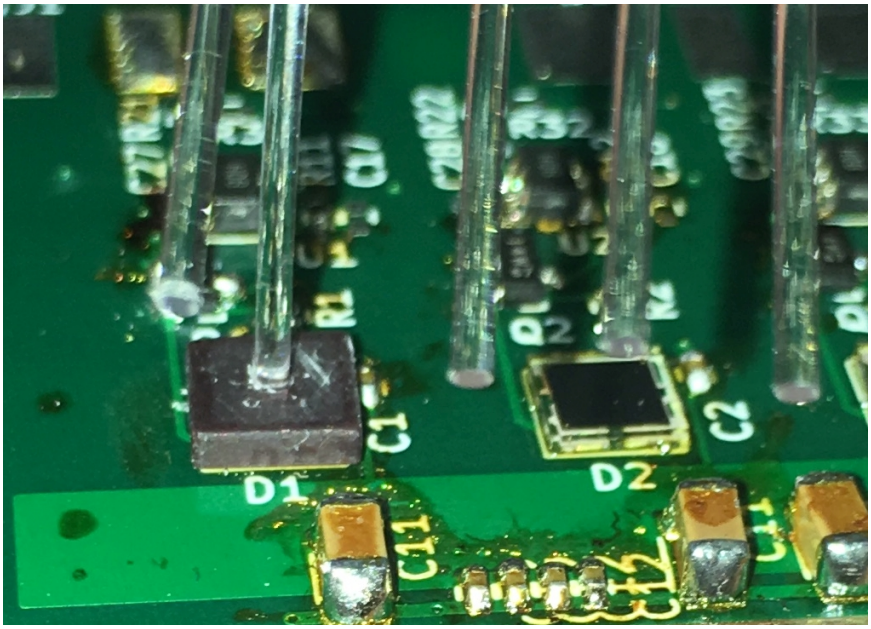

Figure 34. The mating of the fibers to the SiPMs using 3-D printed caps and optical glue.

allow the fiber to fit tightly (Fig. 34). (The caps with one extrusion were used for the initial testing, then the three-extrusion caps were used for collecting data with the spectrometer (Figs. 24 and 25)). The 3-D cap was also used as a way to mount and hold the fiber in place while the optical glue dried (Loctite 349). The electronics used to amplify the SiPM signal required +/-5 V, ground, negative high voltage (approximately 30 V [20]), and a variable reference voltage for the comparator. The output of the electronics was either an SMA cable or a single wire for the digital pulse, depending on the analysis being performed. The SMA cable allowed output of the waveforms for post-processing, or the digital pulses can be used if neutron counts are the only interest. The digital neutron count pulses were used for the normalization of the wafers.

Determining the efficiency of the detectors requires knowledge of the flux of radiation incident on the detectors. However, the detection efficiency of the Eu:LiCAF was not evaluated here since a shadowcone was not available [36]. A shadowcone is typi-

cally fabricated for a specific detector and allows for accurate efficiency measurements by blocking scattered radiation from entering the active area of the detector. Instead, the important parameter was relative efficiency of the ten layers. To determine relative efficiency, each layer was placed 20 cm from the core of the DD generator with the face of the Eu:LiCAF normal to the core. The same electronics were used for each layer and the generator was run for 5 minutes with each layer. The counts were recorded, and each layer was normalized to the lowest performing layer. The results are shown in Table 4. The errors of the normalization factors are not shown in the table, but are generally on the order of 0.0001%.

The construction of the spectrometer began after the normalization of the Eu:LiCAF wafers was completed. A SolidWorks model of the completed spectrometer is shown in Fig. 35. Each of the wafers was built at Tokuyama Corporation in Japan and had four mounting holes (one of each corner), which is shown in Fig. 36. Standoffs were used to rigidly secure the layers so that the spectrometer can be laid on its side. Sufficient space was left to allow enough room to insert wafers of high-density polyethylene between the spectrometer layers. Figure 37 shows how each layer was

Table 4. Eu:LiCAF Wafer Normalization Parameters

Wafer	**Correction Factor** [#]	**Neutron Detection Rate** $\mathbf{s^{-1}cm^{-2}}$
1	0.8659	19.4
2	0.9837	17.1
3	0.9448	17.8
4	1.0000	16.8
5	0.8622	19.5
6	0.9289	18.1
7	0.9553	17.6
8	0.9489	17.7
9	0.9367	18.0
10	0.8883	19.0

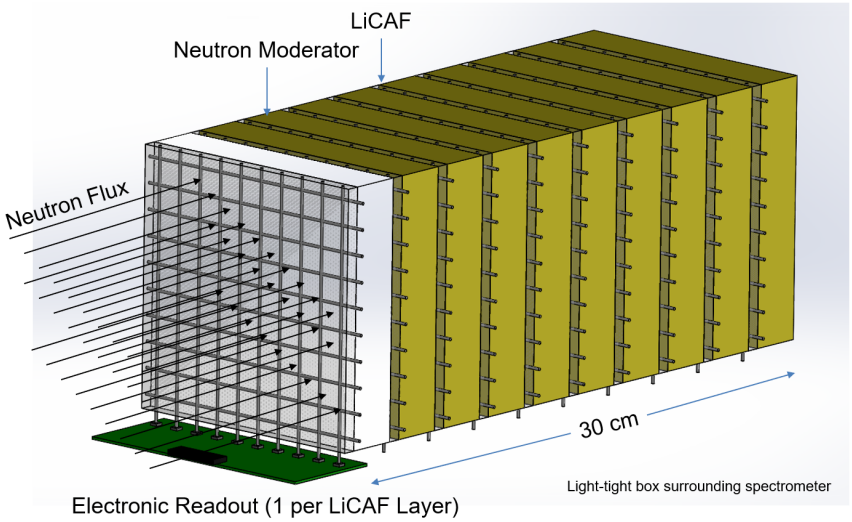

Figure 35. Depiction of the ten-layer spectrometer assembly. Only one layer of electronics is shown. The entire assembly is enclosed in a light-tight box and wrapped in a 1.25 mm layer of cadmium.

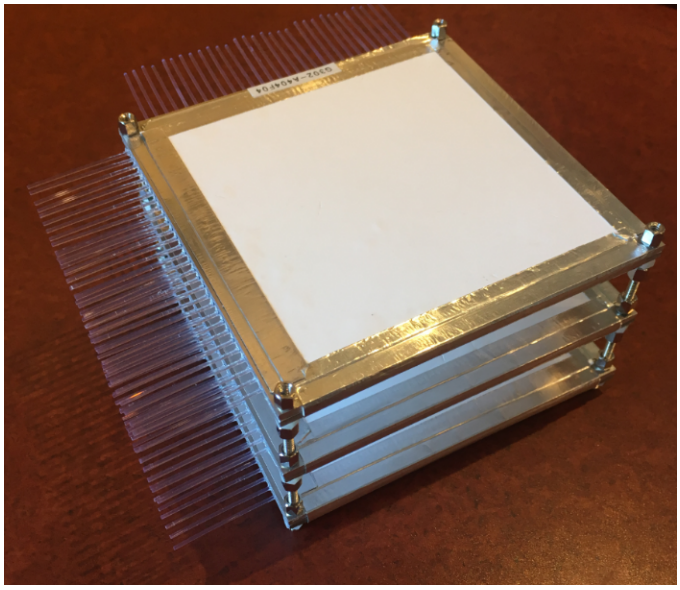

Figure 36. The first three assembled layers of the spectrometer. The standoffs are secured at the four corners of the spectrometer through the mounting holes, and an appropriate gap is left between the layers to allow wafers of neutron moderating material to be inserted.

mounted to the electronics, and how three fibers are mounted to the SiPMs using the 3-D printed caps. The final spectrometer consisted of 10 HDPE moderating layers

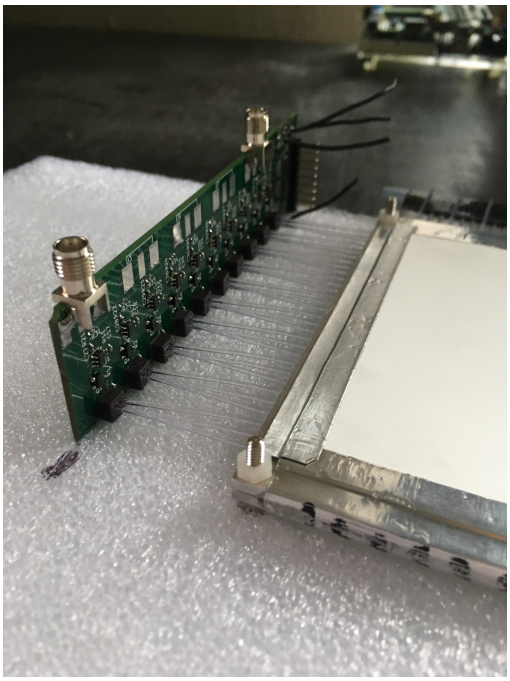

Figure 37. The fibers protruding from the wafer on the X-axis side are mated to the SiPMs (three/SiPM) and the fibers on the Y-axis side are taped off.

and 10 Eu:LiCAF rubberized wafers.

V. Neutron Detection with Eu:LiCAF

Testing with the Eu:LiCAF wafers and the spectrometer assembly was accomplished in several separate experiments. The first experiment was conducted using the thermal neutron port at Ohio State University's test reactor to validate that the electronics were working properly. The next experiment was conducted at AFIT using a DD generator to normalize each of the ten Eu:LiCAF wafers using a fast neutron spectrum. After normalization, the wafers were individually evaluated for their discrimination capability and then a set of count data was taken with each layer (1.25 cm moderator) to obtain a ten-layer spectrometer data set. The next set of experiments occurred at the University of Michigan, again with a DD generator to evaluate the pulse-shape analysis capability of the Eu:LiCAF wafers. An additional set of count data was also taken to obtain spectrometer results with 2.5 cm moderator thickness. Finally, a 15-hour experiment was setup with a single wafer and a ^{252}Cf source at the University of Michigan to get better pulse-shape analysis statistics. The details of these experiments will be discussed in this chapter.

5.1 Testing at Ohio State

The first experiment that was conducted with the Eu:LiCAF test wafer occurred at Ohio State University in the thermal neutron port with a single wafer of the Eu:LiCAF attached to a prototype electronics board. The purpose of the testing at Ohio State was to verify that the assembled electronics were operational. With the thermal neutron beam closed, there were negligible neutron counts. Once the beam was open, there were a significant number of the slower and wider neutron pulses (more than 20 cps for a single fiber). Since only one fiber was mated to the SiPMs, and the data acquisition system was not yet completed for this testing- the only data

that was collected was screenshots of pulse shapes. The experimental setup is shown in Fig. 38 and the pulse screenshots are shown in Figs. 39, 40, and 41.

It is interesting to note the shapes of the pulses in the figures. The shapes and decay times of the various pulses vary significantly depending on the type of particle and interaction medium. Figure 39 shows a scintillation pulse from the wavelength shifting fibers. The pulse is considerably higher in amplitude than the noise but has a very fast decay time relative to the published decay time of the Eu:LiCAF. Figure 40 shows the pulse from a gamma interaction in the Eu:LiCAF, where some of the energy was deposited in a Eu:LiCAF grain, while there was a simultaneous fast electron that scattered and interacted in the WSFs. In this event, there were scintillation photons collected from both the Eu:LiCAF, and from the WSF. If pulse-height discrimination were being used in this case, the event would be counted as a neutron even though it is not. This signal is read-out before the filter, however, after this pulse gets filtered-the fast signal from the WSFs will be suppressed and the probability of the gamma exceeding the pulse-height threshold is significantly lower. Figure 41 is a pulse caused by a neutron capture in a Eu:LiCAF crystal.

5.2 Spectrometer Commissioning

Commissioning of the spectrometer occurred over several trials with the deuterium-deuterium (DD) neutron generator at AFIT. Information and theory about the DD generator can be found in Appendix M. Spectrometer data was taken through two main experiments. The first experiment used the AFIT Adelphi Technology DD108 Neutron Generator. The specifications of the DD108 are shown in Table 5 [37]. The second set of tests were conducted at the University of Michigan using a Thermo Scientific MP320 DD neutron generator with a rated flux of 1×10^6 n/s, and also a ^{252}Cf source with a calculated activity of 2.77×10^6 Bq [38]. For the neutron generators, the

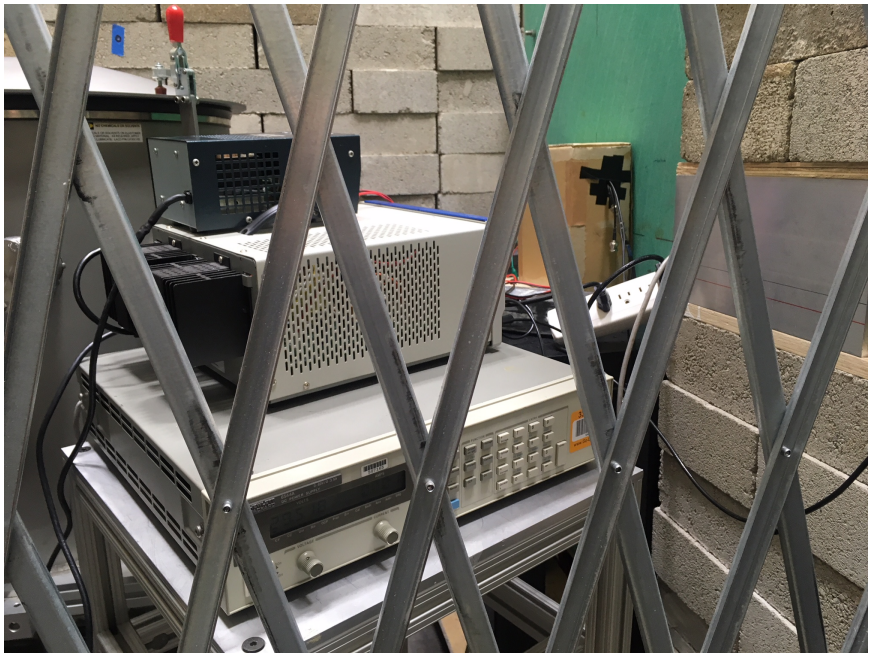

Figure 38. The setup used at Ohio State University. The thermal neutron port is perpendicular to the test Eu:LiCAF wafer, which is located in the box that is adjacent to the far wall. The three pieces of equipment on the cart are power supplies.

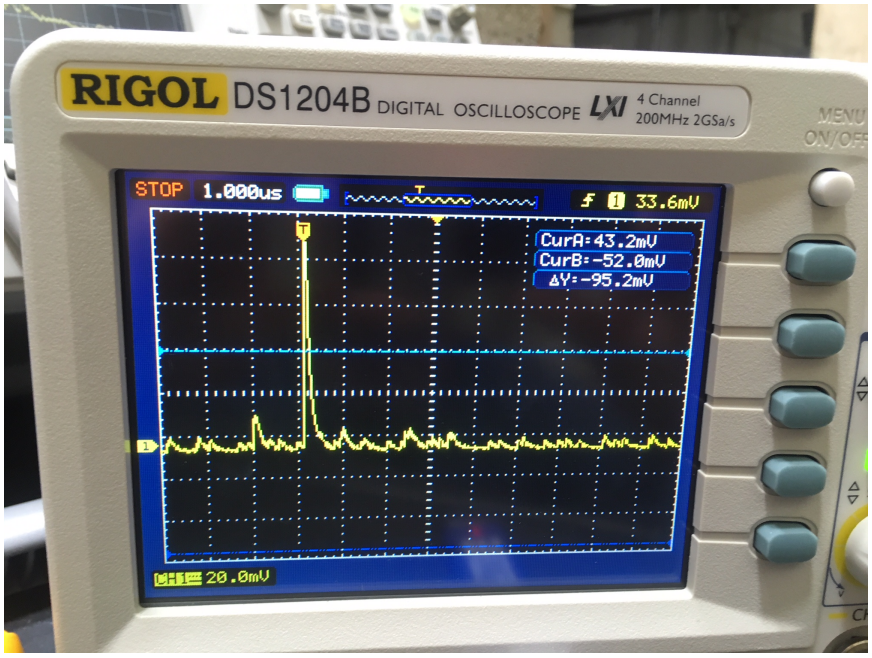

Figure 39. A gamma/WSF pulse on the Rigol DS1204B Oscilloscope from the LiCAF test wafer during a test at Ohio State University.

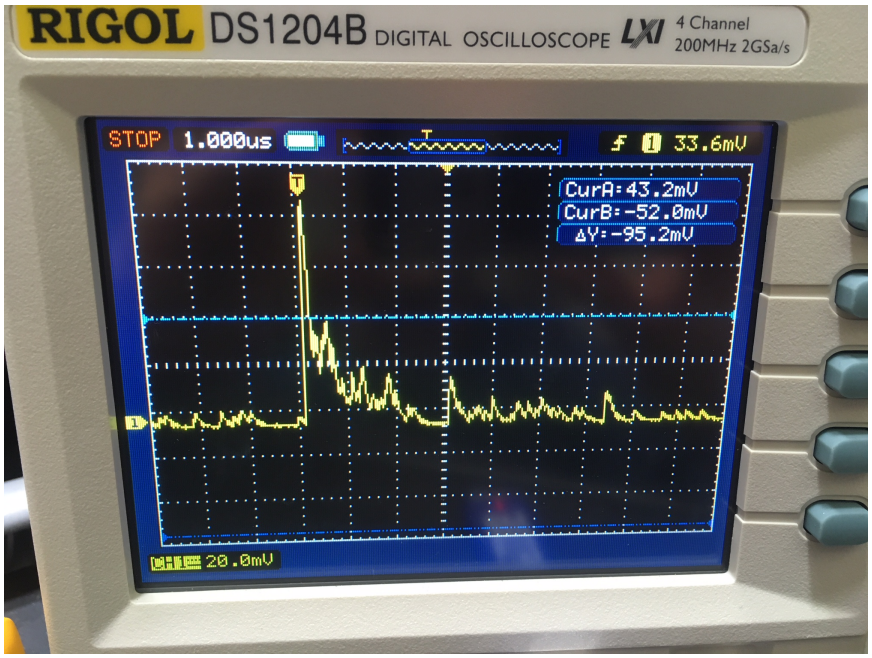

Figure 40. A gamma/WSF pulse on the Rigol DS1204B Oscilloscope from the LiCAF test wafer during a test at Ohio State University.

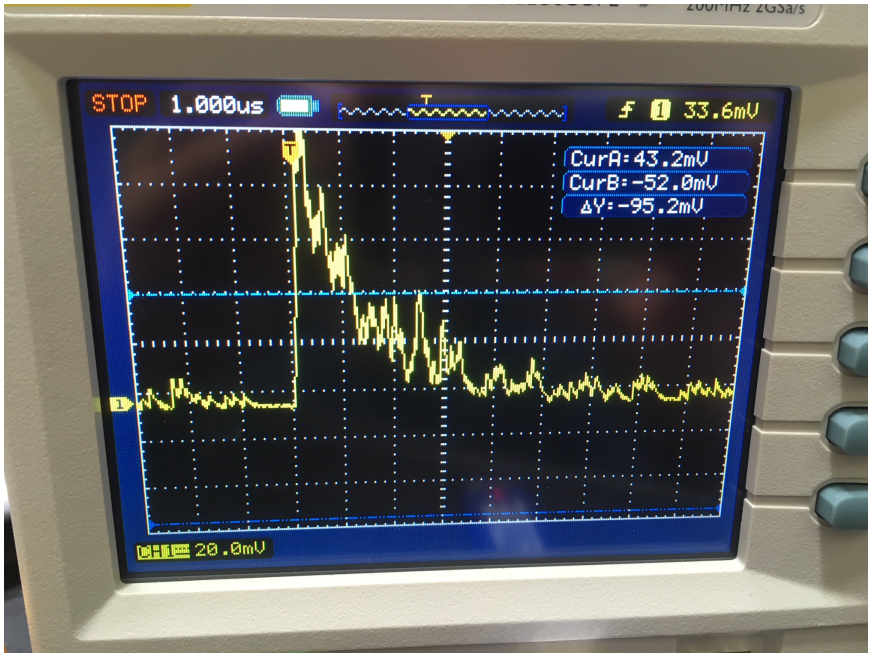

Figure 41. A neutron pulse on the Rigol DS1204B Oscilloscope from the LiCAF test wafer during a test at Ohio State University.

Eu:LiCAF wafers were placed perpendicular to the isotropic flow of neutrons from the core of the generator. The neutron flux was monitored by tracking the pressure of the deuterium gas, and the accelerator voltage. Testing with the ^{252}Cf source was conducted with the source 25 cm from the front face of the Eu:LiCAF wafer. Raw data from the generator runs is shown in Appendix G.

Table 5. Specifications of the Adelphi Technology Incorporated DD108 Neutron Generator.

Property	Value
DD neutron yield	1×10^9 n/second maximum
Neutron energy	≈2.45 MeV
Operating mode	Continuous
Accelerator voltage	100 kV
Operating beam current	3 mA

5.3 Pulse-Height Discrimination

AFIT's DD generator was used to test the detector assembly. Initial discrimination testing with the rubberized Eu:LiCAF wafer concentrated on using pulse-height discrimination, in conjunction with pulse-shape filtering, to allow a simple neutron count output. Three sets of data were taken using a single WSF in the center of an Eu:LiCAF wafer. Background neutron counts were negligible. The first test collected 3000 digitized traces using a ^{137}Cs source placed directly adjacent to the wafer to acquire data from gamma interactions. Data was taken with an SMA cable output terminating into a Teledyne WaveRunner 620Zi oscilloscope. MATLAB was used for post-processing and the area under each of the pulses was integrated (integrated energy) and plotted. Integrated energy was used as a metric since the current generated by the SiPM is proportional to the number of photons collected; integrating the area of the pulse gives a linear correlation to the energy deposited in the scintillator. The

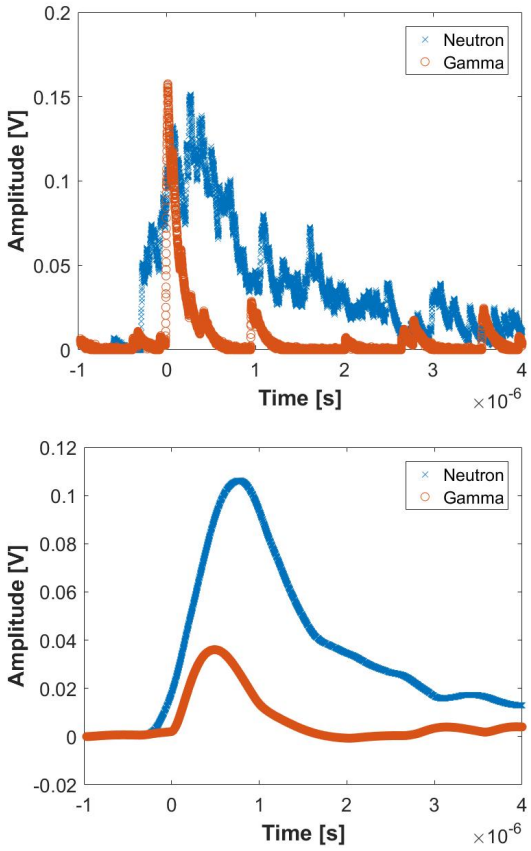

Figure 42. Digitization of the gamma and neutron pulse before being filtered (top) and after a low-pass filter (bottom). In this case, the pre-filter pulse amplitude of the neutron is less than the pre-filter amplitude of the gamma. After filtering, pulse-height discrimination can be used to eliminate the gamma because of the fast-pulse suppression [39]. Filtering makes the use of pulse-height discrimination possible.

next test recorded 3000 traces again, this time using only the DD generator to collect neutron waveforms. Fig 42 shows that the area of the neutron pulses is significantly larger than the area of the gamma/WSF pulses. As shown in Fig. 42 (top), the original amplitude of the gamma/WSF and neutron pulses is approximately the same, which makes pulse-height discrimination impractical. However, as shown in Fig. 42 (bottom), after filtering the two pulses with an $f_c = 360$ kHz active low-pass filter, the amplitude of the higher frequency gamma/WSF pulse is reduced to less than half the amplitude of the neutron pulse, thereby making pulse-height discrimina-

tion practical. The cutoff frequency of 360 kHz was selected to maximize the signal amplitude post-filtering between the gamma/WSF and the Eu:LiCAF scintillation events. The threshold value was experimentally adjusted with the Eu:LiCAF until the gamma/WSF counts were minimized without significantly affecting the number of neutron counts. For simplicity, the threshold value was decreased until the gamma/WSF counts were less than the square root of the neutron counts during the time of data collection.

A final data set was collected for 5-minutes with both the ^{137}Cs source and the DD generator. Figure 43 shows the processed data, with counts versus integrated pulse area. Because of the differences in timing properties of the gamma/WSFs and neutrons in the wafers, the high-energy reaction products of the neutron interaction with ^{6}Li, and the relatively low Eu:LiCAF density in the rubberized matrix, good discrimination can be accomplished. The lower energy counts (left peak of Fig. 43) are the faster pulses from the gammas/WSFs and the peak on the right is the result of the larger, slower neutron pulses. The peak on the right side of Fig. 43 has a total of 3204 counts, whereas the peak on the left has 63. The total counts from the digital output for both gamma/WSFs and neutrons is 3267, and this is the value that would be used for "neutron counts" in a spectroscopy application using the current configuration and settings. It should be noted that when setting a pulse-height threshold, it is not advisable to raise the threshold so high as to eliminate all of the gamma/WSF counts; instead, the goal is to raise it only enough to keep the gamma/WSF counts at or below the square root of the total counts (below counting statistics). For this test, the reported counts are 3267 $\pm$ 58 neutrons, which is a good estimate of the neutrons in the peak of Fig. 43. An overview of the testing results is shown in Table 6. The results show that the presence of the ^{137}Cs source has a negligible impact on the neutron count rate. This validates the GARRn of 1.01 $\pm$0.6%

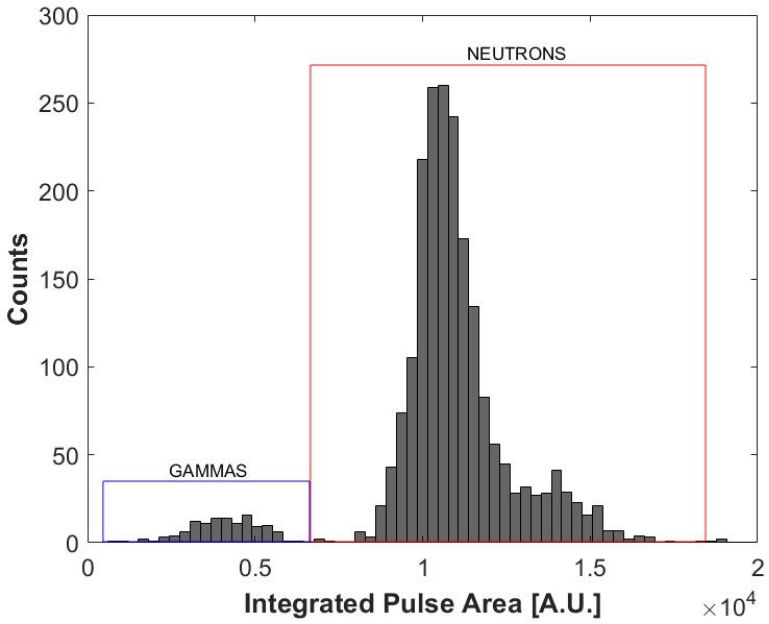

Figure 43. The LiCAF detector is able to discriminate neutrons from gammas using pulse-shape filtering followed by pulse-height discrimination. This is the result of capturing waveforms for a 5 minute test run with both ^{137}Cs and the DD generator.

that was discussed in the Theory section of this document and was expected due to the insensitivity of the Eu:LiCAF to gammas and the ease of filtering gamma/WSF pulses from the data.

Table 6. Neutron/gamma discrimination performance using a comparator threshold of 70 mV.

Test	cps
Background	<0.01
^{137}Cs	0.103
DD Generator	10.7
DD Generator + ^{137}Cs	10.7

The comparator's threshold voltage was set with an HP 3245A precision voltage supply. The electronics have the ability to output the pulse waveform via an SMA cable, however, once the threshold value is determined it is no longer necessary to

use the waveform output. The comparator will output a CMOS pulse anytime the threshold voltage is exceeded. For use in spectroscopy, only the digital output is necessary, and any pulse counter could be employed to tally the number of neutrons captured in the Eu:LiCAF. The use of digital logic makes this methodology desirable in applications where portability is required; there is no need to analyze individual waveforms or store large amounts of data and the Eu:LiCAF wafers and SiPMs are both compact and lightweight.

5.4 Pulse Shape Analysis

Testing at the University of Michigan focused on two goals. First, the ability of the detection system to differentiate WSF and Eu:LiCAF scintillation events using only pulse-height analysis. Second, ten independent measurements were taken with the wafers for one complete set of spectrometer data to evaluate the performance of the spectrometer.

The first focus of testing at the University of Michigan was to determine the rubberized Eu:LiCAF wafer's ability to discriminate neutrons from gammas and WSF scintillation events using only pulse-shape analysis. Pulse-shape analysis was applied to separate gammas and WSF scintillation events from neutron waveforms based on the traditional charge integration method using the SMA output of the electronics. The peak of each waveform was found, and an integration window on each side of the peak was selected to find the area of the peak down to a user-specified threshold level. A Figure of Merit (FoM) was used to evaluate the ability of the detection system to discriminate the neutrons from the gammas and WSF scintillation events. The FoM was defined as:

$$\text{FoM} = \frac{d}{FWHM_n + FWHM_\gamma} \tag{4}$$

where d is the distance between the centroids (μ_n-μ_γ) of the neutron and gamma

peaks when the integrated energy of the waveforms are plotted on the same axis via a histogram, and the $FWHM_n$ and $FWHM_\gamma$ are the full width half-maximum (2.35σ) of the neutron and gamma peaks of the histogram, determined by approximating each peak with a Gaussian fit.

A one-hour DD neutron generator run was first conducted to evaluate the effectiveness of pulse-shape analysis with the rubberized Eu:LiCAF. An Eu:LiCAF wafer was placed adjacent to the target plane of the generator with 2.5 cm of HDPE placed between the Eu:LiCAF wafer and the generator tube. The waveforms were digitized with a Hantek 6074BE PC oscilloscope and post-processing was accomplished using MATLAB. The resulting histogram is shown in Fig. 44 (top). There are three visible peaks. The leftmost peak (blue) is a result of the gamma interactions in the Eu:LiCAF crystal or WSFs which cause scintillation photons to be emitted, or fast-electron interactions in the WSFs. The central peak (red) is a result of neutron (and a few gamma) interactions in the Eu:LiCAF. The tail of the neutron pulses is, on average, much longer than the tail of the gamma/WSFs resulting in a larger area. Finally, the rightmost peak (green) is a result of pulse pile-up in the rubberized wafer and is indicative of deadtime in the electronics. To compute the FoM, the peaks were separated into respective histograms for neutrons and gammas (Fig. 45 shows the neutron histogram). After fitting the histograms with Gaussian curves, the FoM can be calculated. An overview of the fitting parameters is shown in Table 7.

The gamma histogram is partially skewed at lower energies. This is a result of the discrimination method used to calculate the integrated energy. With a low-level discrimination, there is a minimum area that will be represented. Using the parameters from the Gaussian fits, the FoM of the discrimination was calculated to be 1.03 for the DD generator. Plotting the integrated energy versus the pulse-height represents the capability of pulse-shape analysis using rubberized Eu:LiCAF.

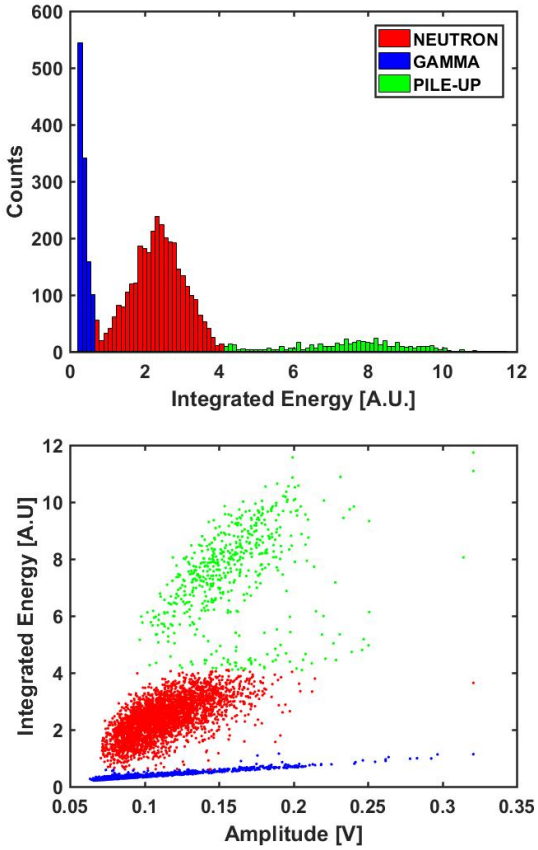

Figure 44. Histogram showing the integrated energy of each waveform from a one-hour DD neutron generator run at the University of Michigan (top). Scatter plot showing integrated area versus pulse height of each waveform from the one-hour DD neutron generator run (bottom). Regardless of the gamma/WSF pulse height, the faster rising edge and lower integrated area allows the neutrons to be easily discriminated from the gammas.

Table 7. Specifications of discrimination and Gaussian fit parameters.

Property	DD	^{252}Cf
Baseline Discrimination Level	10 mV	10 mV
μ_n	2.433	2.678
μ_γ	0.410	0.507
σ_n	0.664	0.0.610
σ_γ	0.169	0.182
FoM	1.033	1.167

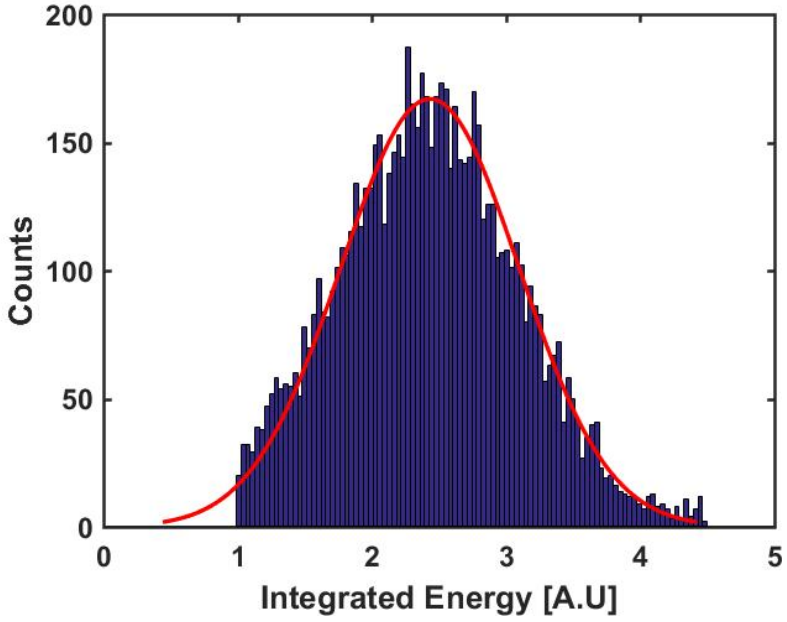

Figure 45. When the neutron pulses are separated from the gamma pulses in Fig. 44 (top), the histogram can be fitted to a Gaussian curve allowing extraction of μ_n and σ_n to determine the FoM.

Fig. 44 (bottom) shows a clear distinction between the gamma/WSF waveforms (bottom), the neutron waveforms (middle) and the pile-up waveforms (top). Table 7 also includes data from the ^{252}Cf source. The FoM of the ^{252}Cf is better than the DD generator because of the lower average energy neutrons and longer data collection time. It is also noteworthy that the scatter plot for the ^{252}Cf (Fig. 46), which was a much weaker source, does not have the "pile up" region that is evident in Fig. 44 (right) from the DD generator.

For neutron spectroscopy applications, this analysis shows that pulse-shape analysis is possible. However, a disadvantage of using pulse-shape analysis is that it requires digitization and/or integration of each waveform to determine if the pulse was a result of a neutron or gamma/WSF interaction. Since each layer of rubberized Eu:LiCAF has 60 optical fibers for signal read-out, the amount of instrumentation required to analyze each waveform and perform real-time pulse-shape analysis is dif-

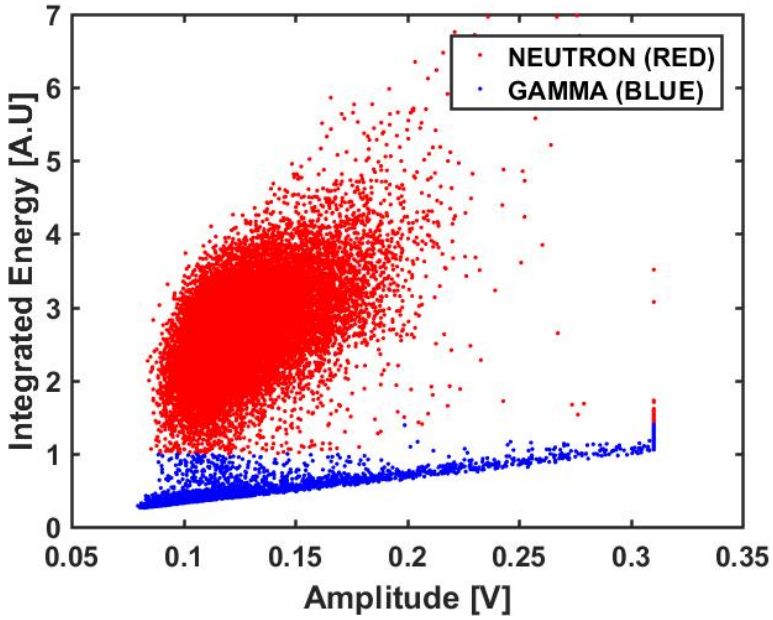

Figure 46. Scatter plot showing integrated area versus pulse height of each waveform from a 15-hour data collection period with a ^{252}Cf source.

ficult in practice. Thus, pulse-height discrimination may be the preferred method in a layered spectrometer system since the same results are achieved with much less computational power.

VI. Neutron Spectroscopy with Eu:LiCAF

The spectrometer data discussed in the previous chapter was in the form of neutron counts. This data can be unfolded to determine the source neutron energy spectrum.

6.1 MAXED

Determining the neutron source energy spectrum requires unfolding the experimental count data. The program MAXED (MXD_FC33), obtained from the Radiation Safety Information Computational Center (RSICC), was used to unfold the spectrum. MXD_FC33 applies the maximum entropy principle to the unfolding problem and has the ability to be run in 'few-channel' mode (*FC*) or 'multi-channel' mode (*MC*). The *FC* program can analyze sets with up to 100 measurements and process fluence vectors with up to 1000 energy bins. The *MC* program can analyze data sets with up to 4096 measurements and can handle fluence vectors up to 4096 energy bins. Since unfolding procedure required for the validation of the spectrometer needed only ten data sets (one for each wafer) each with less than 100 energy bins; the *FC* program was selected [40]. The MAXED input decks for the AFIT and University of Michigan unfolds are shown in Appendices E and F, respectively.

The most significant disadvantage of unfolding is that there is no unique solution. This can be understood intuitively, without further assumptions, as it is clearly not possible to uniquely determine a continuous function like a spectrum from only a finite number of measurements (in this case, 10). Unfortunately, in the case of unfolding data from a layered spectrometer, which is characterized by response functions that are not sharply peaked and can change gradually over many orders of magnitude of neutron energy, there are no unique solutions [41]. The problem becomes one of inference, with the best estimate of the spectrum limited by the available information

[41]. A priori information, referred to as the default spectrum, is used to provide a starting point for the unfold. This reformulates the unfolding problem: given a default spectrum, what algorithm should be used to modify that default spectrum to obtain a final spectrum that accounts for the new information contained in the measurements and best fits the data [41]? A formal argument using concepts that originate in information theory shows that for this type of measurement, the maximum entropy method is the only general method of solving this problem that does not lead to inconsistencies [42].

Error Analysis.

The primary figure used here to determine the fit of the energy spectrum to the default spectrum is χ^2. This is often referred to as the "goodness of fit" test. If ν independent variables x_i are each normally distributed with mean μ_i and variance σ_i^2, then the quantity chi-squared (χ^2) is defined by: [43]

$$\chi^2 \equiv \frac{(x_1-\mu_1)^2}{\sigma_1^2} + \frac{(x_2-\mu_2)^2}{\sigma_2^2} + ... + \frac{(x_\nu-\mu_\nu)^2}{\sigma_\nu^2} = \sum_{i=1}^{\nu} \frac{(x_i-\mu_i)^2}{\sigma_i^2} \qquad (5)$$

Ideally, given random fluctuations of the values of x_i about their mean values, each term in the sum will be of order unity. In this case, there is a set of N experimentally measured quantities x_i and how well they fit with the hypothesized values in the default spectrum (μ_i) must be determined. It can be noted in Tables 12 and 13 (Appendix J) that the requested χ^2/D.O.F. is 1.0. This is because, if μ_i and σ_i were chosen correctly (the energy of the DD generator, and uncertainty), then χ^2 will be approximately equal to ν. If it is, it can be concluded that MAXED has unfolded a spectrum that fits well with the hypothesized default spectrum. If the χ^2 value is too high, it may be concluded that the unfold does not accurately represent the default spectrum. A $\chi^2 \ll 1.0$ may conclude only that either (i) the model is valid but that

a statistically improbable excursion of χ^2 has occurred, or (ii) the values of σ_i was overestimated, or (iii) the data is "too good to be true" or fraudulent [43]. If the data here were "too good to be true", MAXED would output a spectrum of exactly 2.5 MeV neutrons (the value used as a hypothesis).

In MAXED, sensitivity analysis and the propagation of uncertainties are accomplished by considering the effect of variations δN_k in the measurements and δf_i^{DEF} in the default spectrum. For the deconvolution, the σ_k were defined as the square roots of N_k:

$$\sigma_k = \sqrt{N_k} \tag{6}$$

It is estimated here that the relatively large statistical errors dominated other sources of error. The response function errors were also defined as the square root of number of counts. Considering only the changes in the measured counts in each layer results in the following set of equations from Equations (27), (26), (30), and (31): (See Appendix K)

$$\delta N_k + \delta \epsilon_k = \sum_i R_{ki} \delta_{fi} \tag{7}$$

$$\sum_k \frac{\delta N_k}{\sigma_k} - \sum_{k,i} \frac{R_{ki} \delta f_i}{\sigma_k} = 0 \tag{8}$$

$$\delta f_i = -\sum_k R_{ki} f_i \left(\delta \lambda_k + \frac{\delta \gamma}{\sigma_k} \right) \tag{9}$$

$$\delta \epsilon_k = \sum_m \left[\frac{1}{2} \left(\frac{4\Omega}{\sum_j (\lambda_j \sigma_j)^2} \right)^{1/2} \left(\delta_{km} \sigma_k \sigma_m - \frac{\lambda_k \sigma_k^2 \lambda_m \sigma_m^2}{\sum_j (\lambda_j \sigma_j)^2} \right) \right] \delta \lambda_m. \tag{10}$$

The variation of γ (a MAXED output parameter used to define the energy spectrum)

can be expressed in terms of the λ_k and the N_ks:

$$\delta\gamma = \frac{-\left(\sum_k \frac{\delta N_k}{\sigma_k} + \sum_{k,i,l} \frac{R_{ki}R_{il}f_i\delta\lambda_l}{\sigma_k}\right)}{\sum_{k,i,l} \frac{R_{ki}R_{il}f_i}{\sigma_k\sigma_l}} \tag{11}$$

This can all be repeated for the error in the default spectrum, while keeping the error of the measured counts at zero. Adding the two sources of uncertainty together yields an uncertainty matrix U, given by [41]:

$$U_{ij} = \sum_{a,b} \frac{\delta f_i}{\delta N_a} K_{ab} \frac{\delta f_j}{\delta N_b} + \sum_{c,d} \frac{\delta f_i}{\delta f_c^{DEF}} K'_{cd} \frac{\delta f_j}{\delta f_d^{DEF}} \tag{12}$$

The uncertainties reported in MAXED are a result of propagating the correlated uncertainties with Eqn. 12. The correlation matrices K and K′ are discussed in the next section.

6.2 MAXED Unfolding Results

Three dimensional surfaces of the spectrometer counts were constructed and are shown in Figs. 47 and 48. Figure 47 shows the neutron counts for each layer for the experiment conducted at AFIT, with a moderator thickness of 1.25 cm (HDPE). Figure 48 shows the neutron counts for each layer for the experiment conducted at the University of Michigan, with a moderator thickness of 2.5 cm. The spectrometer was configured as shown in Fig. 35. The electronics were moved back one layer for each successive generator run. While the Eu:LiCAF is segmented via embedded fibers in both the X and Y axes, only the X-axis was used. For both moderator thicknesses, there is an increase in counts toward the center of each layer. This was expected and verifed in Geant4 simulations. This phenomenon is due to the increased neutron escape from scatters that happen toward the edges of the layers. The fibers

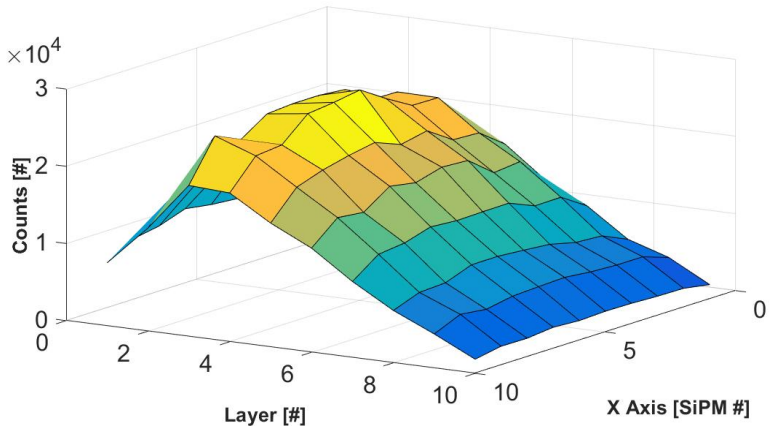

Figure 47. 3-dimensional representation of spectrometer counts after 5-minute spectrometer run at AFIT's DD generator. Layer #1 is closest to the generator, and there are more counts toward the center of the spectrometer, as opposed to the boundaries.

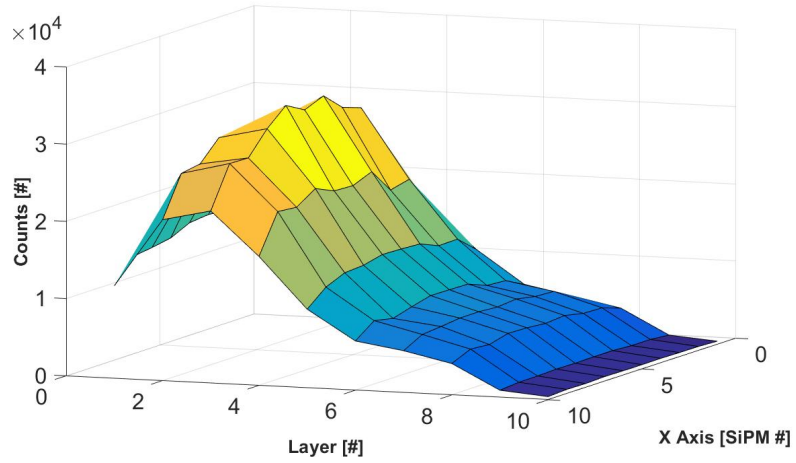

Figure 48. 3-dimensional representation of spectrometer counts after 1-hour spectrometer run at University of Michigan's DD generator. Layer #1 is closest to the generator, and there are more counts toward the center of the spectrometer, as opposed to the boundaries

along the Y-axis were sealed with opaque tape. Total counts for each layer were obtained by summing each of the counts along the X-axis, then corrected using the normalization factors in Table 4. The results of each layer for the AFIT and University of Michigan testing are shown in Figs. 49 and 50, respectively. In Fig. 49, the AFIT experimental data very closely resembles the Geant4 simulation data. This was the

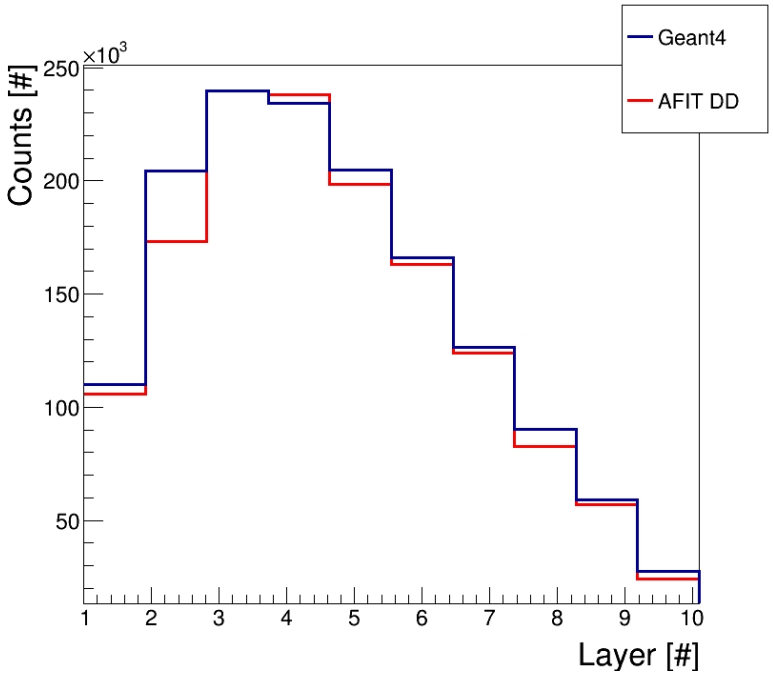

Figure 49. Comparison between Geant4 simulation and data taken after a 5-minute spectrometer run at AFIT's DD generator using ROOT. With the exception of layer two, the experimentally obtained count data is within 5% of the response function. Due to the small magnitude of the error bars, they are not represented in the plot.

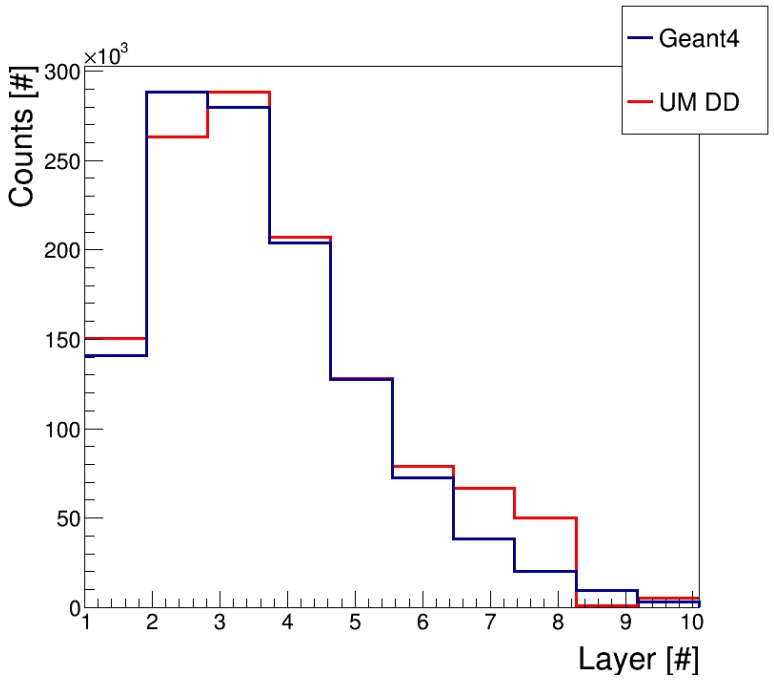

Figure 50. Comparison between Geant4 simulation and data taken after 1-hour spectrometer run at University of Michigan's DD generator using ROOT. The experimental data matches the response function very well (within $\sim 10\%$) until layers 7 and 8, where a significant increase in experimenally obtained counts is shown. The increase is likely due to backscattering of epithermal neutrons. Due to the small magnitude of the error bars, they are not represented in the plot.

experimentally obtained count data used in MAXED to determine the energy of the DD generator neutrons. Likewise, Fig. 50 shows the results of a 1-hour spectrometer run with a moderator thickness of 2.5 cm. While the data does closely resemble the simulations for the first 5 layers, layers 6-9 start to show deviation from the simulated response functions. The deviations are likely due to backscattered neutrons that enter the spectrometer from the rear. Layer 10 did not show an increased number of counts because of the cadmium layer surrounding the spectrometer; only the higher-energy backscattered neutrons made it past the cadmium and thermalized in the spectrometer. The DD generator at the University of Michigan was located in a larger experimental bay that had auxiliary equipment around the generator that was unaccounted for in the Geant4 response function simulations.

After collecting the neutron count data from each of the spectrometer layers, the next step is unfolding the data. MAXED maximizes the entropy using a simulated annealing optimization algorithm when unfolding the spectrometer data to simultaneously optimize several parameters. The simulated annealing optimization algorithm can be considered analogous to the physical process by which a material changes state while minimizing its energy [44]. A slow, careful cooling often results in a highly ordered crystalline state of lowest energy while a rapid cooling instead yields defects inside the material [45]. This is where the temperature reduction factor is applicable. Without the TRF, the minimization algorithm is very likely to get stuck in a metastable, local minimum. On the contrary, simulated annealing permits uphill moves under the control of a temperature parameter. At higher temperature, only the gross behavior of the cost function is relevant to the search for the global minimum. As temperature decreases, however, finer details can be developed to get a good final point. Several temperature reduction factors were evaluated to determine how they affect the resultant unfold. The results of the temperature analysis are shown in Table 8.

The requested χ^2/D.O.F. was held constant at 1.0 through all of the unfolds and the only parameter that was changed was the temperature reduction factor. Because of the problem with uniqueness, using a priori data provides a "starting point" from which to maximize entropy to determine a final spectrum that accounts for the new information contained in the measurements and that fits the data [41].

The recommended temperature reduction factor for MAXED unfolding is 0.85 [46], and these unfolding results are shown in Fig. 51. Since the incident energy spectrum of the neutrons from the DD generators can be approximated to be monoenergetic, an average energy was calculated from the output spectra of MAXED. The MAXED ouput spectra are in fluence per MeV bin (see Table 19 in Appendix K),

Table 8. DD Generator Unfolding Results

Temp. Red. Factor	AFIT		MI	
	μ(Energy)	χ^2/D.O.F	μ(Energy)	χ^2/D.O.F
.90	2.71	0.88	3.67	30.09
.85	2.66	1.58	3.15	79.79
.80	2.71	1.10	3.03	641.6
.75	2.77	1.38	3.03	47.61
.70	2.62	1.77	3.04	31.69
.65	2.75	1.19	3.82	41.14
.60	2.82	1.12	2.96	31.38
.55	2.77	1.18	2.97	93.90
.50	2.70	1.91	3.06	89.77
.45	2.80	1.42	3.17	34.74
.40	2.80	1.56	3.04	32.18
.35	2.77	1.06	5.54	186.5
.30	2.72	1.12	2.96	38.03

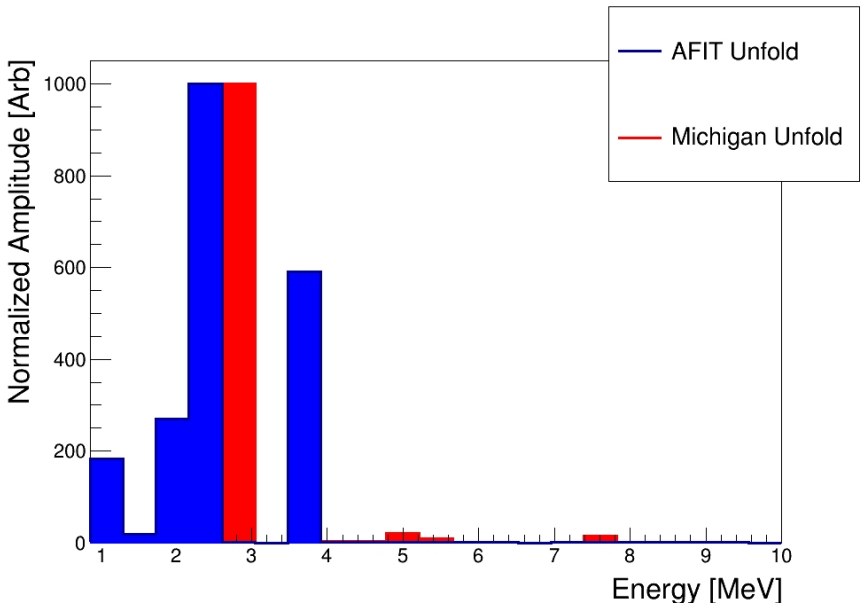

Figure 51. MAXED deconvolution of spectrometer run at both AFIT and University of Michigan using monoenergetic 2.45 MeV neutrons for a priori spectrum with TRF of 0.85.

and the average energy was computed by summing the total energy and dividing by the total fluence. Row 2 of Table 8 shows that an average energy of 2.66 MeV

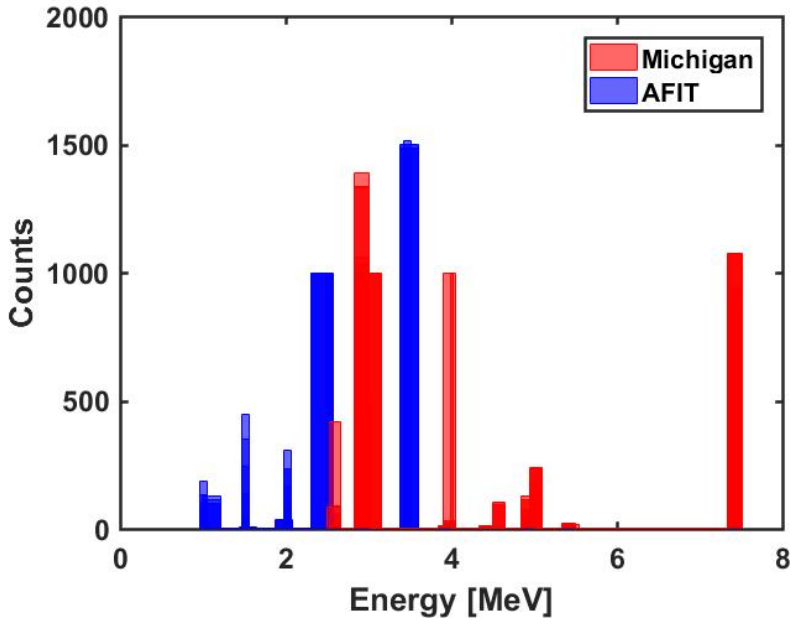

Figure 52. Results for 13 MAXED runs at various temperature reduction factors for both the AFIT and University of Michigan spectrometer tests. There is a distribution around ~2.45 MeV for both experiments, however there is a higher energy peak evident in the University of Michigan unfold results due to the higher counts obtained in layers 6 through 9 of the spectrometer.

was determined with a χ^2/D.O.F of 1.58 for the spectrometer test at AFIT, and an average energy of 3.15 MeV was obtained with a χ^2/D.O.F of 79.79 for the testing at University of Michigan. The values in row two were used since they reflect a temperature reduction factor of 0.85. A histogram of all energies unfolded for each of the 13 temperature reduction factors is shown in Fig. 52. The higher counts, from backscattered neutrons, in layers 6-9 of the spectrometer test at Michigan resulted in a higher net energy and also caused the resultant unfold results to be poor. The AFIT spectrometer test, however, shows a good distribution near 2.45 MeV, and all of the χ^2 values obtained are within one standard deviation of 1.0 on the chi-squared distribution plot. While there is no error reported for the final average energy obtained using MAXED, Tables 9 and 10 show the calculated/measured (C/M) ratio for each of the 10 Eu:LiCAF wafer detectors, and also the computed λ_k values for each of the

wafers. The simulated annealing algorithm is used to maximize the entropy S (Eqn. (29)) using the constraints in Eqns. (27) and (28), producing values for λ_k which are related to the final energy spectrum via [40]:

$$f_i = f_i^{DEF} exp\left(-\sum_k \lambda_k R_{ki}\right). \tag{13}$$

Table 9. Unfold errors and final λ values for AFIT

#	C/M Ratio	StDev(C/M) from Total Unc.	StDev(C/M) from Stat Unc.	Lambda(λ)
1	1.07786	0.1539	0.00452	8.325691E-4
2	1.05663	0.1496	0.00350	2.526442E-4
3	1.02920	0.1463	0.00293	-1.977880E-4
4	0.99848	0.1441	0.00290	-4.266265E-4
5	1.03150	0.1471	0.00323	3.820434E-6
6	0.99477	0.1454	0.00349	-4.348146E-4
7	0.98025	0.1454	0.00398	-7.553486E-4
8	1.03699	0.1526	0.00501	9.772045E-4
9	0.97084	0.1512	0.00583	-1.214619E-3
10	1.06661	0.1744	0.00944	5.422050E-3

Table 10. Unfold errors and final λ values for Michigan

#	C/M Ratio	StDev(C/M) from Total Unc.	StDev(C/M) from Stat Unc.	Lambda(λ)
1	0.79775	0.01322	0.00330	-8.837561E-5
2	0.95649	0.01409	0.00270	1.447682E-4
3	0.88382	0.01358	0.00249	3.320812E-5
4	0.94775	0.01411	0.00303	8.425696E-5
5	1.02039	0.01484	0.00399	2.320704E-4
6	1.00078	0.01504	0.00504	2.232096E-4
7	0.68469	0.01301	0.00470	-1.903631E-3
8	0.50573	0.01229	0.00502	-1.159838E-2
9	1.14281	0.02084	0.01429	1.771052E-2
10	0.84415	0.01321	0.01791	4.437544E-3

Any change of the input parameters (N_k, σ_k, f_i^{DEF}, R_{ki}, and Ω) will lead to a change in the output parameters λ_k (shown in the last column of Tables 9 and 10). The error of the resultant energy spectrum is difficult to quantify because of the correlated errors between each of the experimentally obtained counts of each layer, and also the errors in the default spectrum used for unfolding. MAXED does propagate errors, and the net standard deviation for the calculated/measured ratios are reported in the third and fourth columns of Tables 9 and 10. These are the uncertainties calculated with the assumption that the correlated errors are defined by a matrix $\mathcal{B}$:

$$\mathcal{B} = \begin{pmatrix} \sigma_1^2 & & & \\ & \sigma_2^2 & & \\ & & \ddots & \\ & & & \sigma_m^2 \end{pmatrix}$$

For changes in the measured data, the uncertainty matrix is defined by [40]:

$$U = \frac{\delta f}{\delta N} \cdot \mathcal{B} \cdot \left(\frac{\delta f}{\delta N} \right)^T . \tag{14}$$

Propagated error for the default spectrum is calculated in a similar way. Since this error does not translate into the resultant energy spectrum, an effort was made to define the uncertainty in the unfold by considering the spread of data as a result of varying the temperature reduction factor. This results in estimated average neutron spectrum energy values for the AFIT DD generator spectrum of 2.7390 $\pm$ 0.0315 MeV and a value for the University of Michigan DD generator spectrum of 3.3412 $\pm$ 0.3886 MeV.

This research indicates that, given appropriate a priori information about the spectrum and inclusive simulations (response functions), a rubberized Eu:LiCAF spectrometer equipped with portable, custom electronics can accurately identify the energy of a monoenergetic neutron source. This work also demonstrates that the over-

lapping response curves, and the sensitivity of the spectrometer to its environment make it challenging to measure neutrons with adequate resolution for all conditions.

In an effort to improve the results of the University of Michigan spectrometer tests, the data was unfolded for a second time using only the first five layers of data. Since the hypothesized backscatter is primarily evident in the last half of the spectrometer, utilizing only the first five layers was explored to reduce the effect of the scattering, and to produce a better fit to the 2.45 MeV neutrons. The results of the five-layer unfold are shown in Fig. 53. Performing the unfold with a reduced number of layers improved the fit of the Michigan data to an energy of 2.78 MeV with a χ^2/D.O.F. of 1.51. A disadvantage of the five-layer unfolding, compared to the 10 layers (although not quantified herein) is an increase in uncertainty. The reduced-layer unfold demonstrated that the spectrometer is capable of identifying the energy of a mono-energetic neutron source even in the presence of anomalies in the data. Given the ability to accurately model the testing environment, the spectrometer is excellent at differentiating thermal, epithermal, and fast neutron spectra. Future research concentrating on optimization of the HDPE layer thickness may prove to greatly increase the spectrum resolution in specific energy regions.

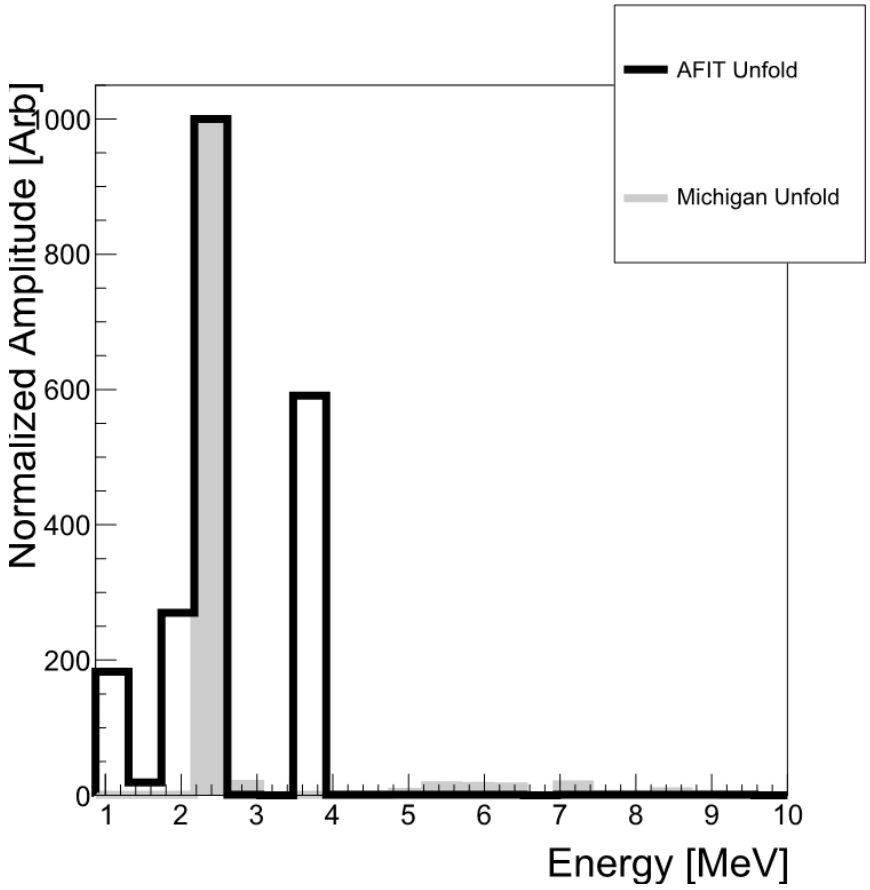

Figure 53. Results of MAXED runs at a temperature reduction factor of 0.85 for the first five layers of University of Michigan spectrometer data, versus the full 10 layer unfold of AFIT data. The incident neutron energy is deconvoluted with an a priori spectrum of monoenergetic 2.45 MeV neutrons.

VII. Conclusions and Recommendations for Future Work

This research demonstrates that Eu:LiCAF is a promising potential replacement for ^{3}He in at least some neutron applications, and shows excellent promise for neutron spectroscopy applications. While a pure Eu:LiCAF crystal was not evaluated here, the scintillation photons are easily detectable in the rubberized form with commercial off-the-shelf (COTS) SiPMs. In addition, discrimination between neutrons and gammas can be performed using simple and compact electronics which would enable man portable applications. It was also demonstrated that Eu:LiCAF shows excellent promise as a detector material for both pulse-height discrimination and pulse-shape applications. Pulse-height discrimination allowed for a simple neutron-count output where the gamma counts were below the neutron counting statistics, and a FoM of 1.03 was demonstrated using pulse-shape analysis with the DD neutron generator. The FoM with a ^{252}Cf source was calculated to be 1.17.

A portable neutron spectrometer was developed using alternating layers of rubberized Eu:LiCAF wafers and HDPE. Portability of the spectrometer was maintained by utilizing custom electronics that require only $\pm$5 V, a negative bias voltage supply of approximately 30 V, and a variable voltage supply for setting the user-defined threshold level. Eu:LiCAF is able to differentiate gammas from neutrons using pulse-height discrimination in conjunction with pulse shape filtering, and ambient photons and thermal neutrons are shielded with a light-tight box and a layer of cadmium, respectively. MAXED was used to unfold the spectrometer data into a neutron energy spectrum, and the commissioning run at the Air Force Institute of Technology yielded an average neutron energy of 2.71 MeV with a χ^2 value of 0.88/D.O.F. when fit to a monoenergetic neutron energy spectrum of 2.45 MeV.

Future testing can be done to analyze the Eu:LiCAF response to higher-energy gammas and to verify the WSF response to gammas in the absence of Eu:LiCAF.

Work can be done to increase the resolution of the spectrometer by optimizing the thickness of the HDPE layers and/or exploring spectrometers with more than 10 layers. This research can be continued in the following ways:

1. Analyze the rubberized Eu:LiCAF wafer's response to higher-energy gammas by exposing the wafer to various high-energy gamma sources and applying background subtraction. A plot of ''comparator triggers" versus gamma energy for a pre-determined exposure time would provide valuable information regarding the low gamma sensitivity of the wafers.

2. Verify Watanabe et al's experimental results regarding WSF interaction with gammas. An experiment can be done with crosshatched fibers both with and without the rubberized Eu:LiCAF present. Watanabe et al did measure a gamma response with the rubberized Eu:LiCAF wafer with embedded WSFs, but a near-identical response was also measured using only the WSFs. Repeating the experiment with neutrons would also be interesting to determine the WSF response to fast neutrons.

3. Simulation work can be done to optimize the resolution of the spectrometer in a specific energy region. Varying moderator thickness in a single spectrometer can be explored in addition to increasing the number of layers. The goal is to determine a way to increase the separation and uniqueness of the response functions.

4. Utilizing the X and Y-axis readout information of the spectrometer. The rubberized Eu:LiCAF wafers have fibers extending from both the X and Y-axes; simulation work can be done to determine if it is possible to get source position information by utilizing the WSF signal on both axes.

5. Explore the use of PhCs to improve the photon collection between the WSFs and the SiPMs.

6. Study temperature effects on the gain of the SiPMs.

Appendix A. KiCAD and LTSpice Circuit Design

This appendix shows the design files of the printed circuit board, and also the circuit simulations. The schematic used in the LTSpice simulations is shown in Fig. 57. The simulations were used to realize the values of the passive components in order to meet the filter parameter from the MATLAB analysis (Fig. 16). Figures 55 and 56 show the outputs of the simulations.

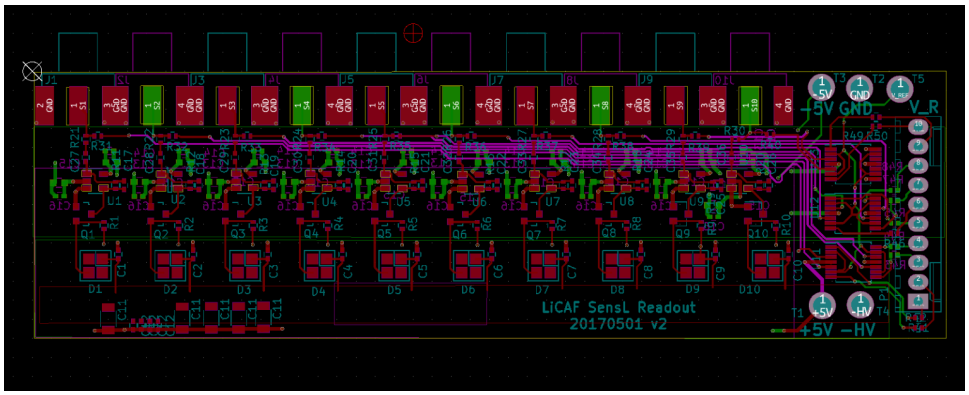

Figure 54. The design file for the printed circuit board used to turn the photons from the scintillating crystals into a digital signal. The ability to perform pulse height analysis is tied directly into the board using V_{ref}.

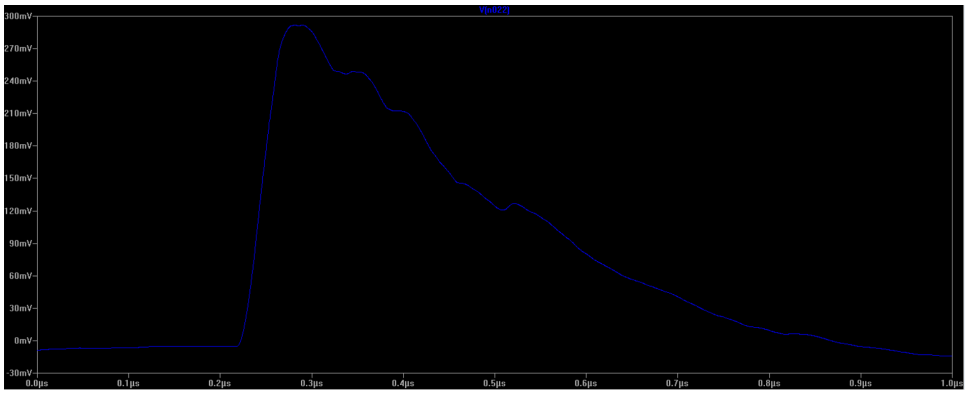

Figure 55. BGO simulated signal using LTSpice.

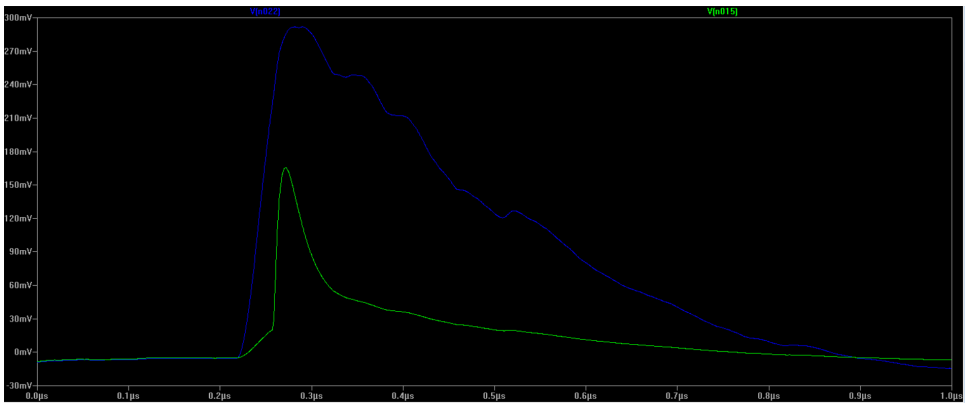

Figure 56. BGO vs WSF signal simulated signal using LTSpice.

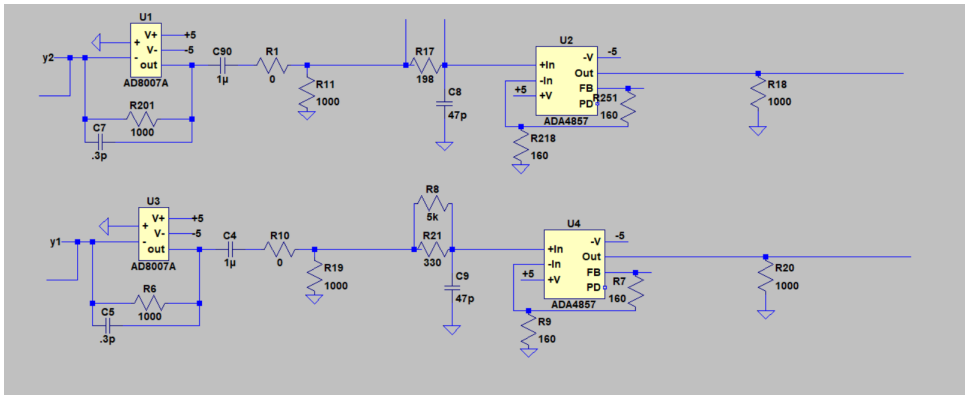

Figure 57. Circuit schematic for LTSpice simulations.

Appendix B. MATLAB Code - Butterworth/Fourier Decomposition

This code was written before the FPGA was programmed and allowed for post-analysis of the spectra by saving the data from a 12-bit Lecroy scope and importing it into MATLAB.

```
lecroy_data = 1;
WCD_data = 0;
chCRT=0;
while chCRT≠1

  chCRT = menu('CRT Data Analysis Menu',...
            'Done',...
            '',...
            'Select data file',...                %3
            '',...                                 %4
            'Change default parameter values',...        %5
            '',...
            'Start CRT analysis',...                     %7
            'Plot CRT results',...                       %8
            'Plot Pulse Shape results',...                          %9
            '');

  if chCRT==3

    % initialize default parameters
    SC_ana_options_init

    % user select file
    [fname,fnn] = CRTa_sel_lecroy();
```

```
25
26      KeysightData = 0;  LecroyData=1;
27
28      % load selected file
29      pause(0.1);          % allow display text msg (!)
30      disp([' >>>> loading ',fname]);
31      load(fname);
32
33      disp(['   LecroySamplingPerSec: ...
           ',num2str(LecroySamplingPerSec/1e9),' GS/sec']);
34      disp(['   LecroyTimeSecPerDiv: ...
           ',num2str(LecroyTimeSecPerDiv*1e9),' ns/div']);
35      disp(['   Bin2matSamplingPerSec: ...
           ',num2str(Bin2matSamplingPerSec/1e9),' GS/sec']);
36
37      % update sampling rate for data analysis
38      %=========================================
39      Fsamp = Bin2matSamplingPerSec;
40      tsamp = 1/Fsamp;
41      Fsamp_up = Fsamp;   % no up-sampling or down sampling at this ...
           point
42      Fsamp_dn = Fsamp;
43      Butt_Fs = [Fsamp,Fsamp];
44
45      % execute setups for selected dataset
46      %====================================
47      CRTa_sel_lecroy_cmd(fnn);
48
49      % put scope data into a structure
50      % (Note that channel assignments not always consistent!!!)
51      %=========================================================
52      for i = 1:4 chdat(i).amp = zeros(1,1); end
```

```
53      if exist('dataX')                          % pre 8/21/14
54         chdat(1).time = dataX; clear dataX
55         if exist('dataY1') chdat(1).amp = dataY1; clear dataY1; end
56         if exist('dataY2') chdat(2).amp = dataY2; clear dataY2; end
57         if exist('dataY3') chdat(3).amp = dataY3; clear dataY3; end
58         if exist('dataY4') chdat(4).amp = dataY4; clear dataY4; end
59
60      % 8/21/14  -- see CRTa_sel_lecroy.m for channel definitions
61      elseif exist('Xtime') & LecroyData==1
62         chdat(1).time = Xtime;                % time array in seconds
63         if exist('CH1') chdat(1).amp = CH1; clear CH1; end ...
                        % signal pulse array in volts
64         if exist('CH2') chdat(2).amp = CH2; clear CH2; end ...
                        % signal pulse array in volts
65         if exist('CH3') chdat(3).amp = CH3; clear CH3; end ...
                        % signal pulse array in volts
66         if exist('CH4') chdat(4).amp = CH4; clear CH4; end ...
                        % signal pulse array in volts
67
68         chdat = Resize_DataMat(chdat,MaxNumTrigger);
69
70
71      % 4/3/17 -- use waveform sample interpolation to align ...
            time-axis for all waveforms
72      elseif exist('Xtime_ref') & LecroyData==1
73         Xtime = Xtime_ref;
74         chdat(1).time = Xtime_ref;               % time array in ...
               seconds
75         if exist('CH1') chdat(1).amp = CH1; clear CH1; end ...
                        % signal pulse array in volts
76         if exist('CH2') chdat(2).amp = CH2; clear CH2; end ...
                        % signal pulse array in volts
```

```
77          if exist('CH3') chdat(3).amp = CH3; clear CH3; end ...
                        % signal pulse array in volts
78          if exist('CH4') chdat(4).amp = CH4; clear CH4; end ...
                        % signal pulse array in volts
79
80          chdat = Resize_DataMat(chdat,MaxNumTrigger);
81
82      % 4/3/17 -- not all waveforms digitized at the same instant: ...
            save time arrays with each pulse
83      elseif exist('LecroyTimeSecPerDiv') & LecroyData==1
84          if exist('CH1')
85              chdat(1).amp = CH1; clear CH1;      % signal waveform ...
                    amplitude in volts
86              chdat(1).t = CH1_t; clear CH1_t;    % signal waveform ...
                    time array in seconds
87          end
88          if exist('CH2')
89              chdat(2).amp = CH2; clear CH2;      % signal waveform ...
                    amplitude in volts
90              chdat(2).t = CH2_t; clear CH2_t;    % signal waveform ...
                    time array in seconds
91          end
92          if exist('CH3')
93              chdat(3).amp = CH3; clear CH3;      % signal waveform ...
                    amplitude in volts
94              chdat(3).t = CH3_t; clear CH3_t;    % signal waveform ...
                    time array in seconds
95          end
96          if exist('CH4')
97              chdat(4).amp = CH4; clear CH4;      % signal waveform ...
                    amplitude in volts
98              chdat(4).t = CH4_t; clear CH4_t;    % signal waveform ...
```

```
                time array in seconds
99          end
100
101         chdat = Resize_DataMat2(chdat,MaxNumTrigger);
102
103     % 2/25/16  -- Keysight scope data format
104     elseif exist('Xtime') & KeysightData==1
105         chdat(1).time = Xtime;                % time array in seconds
106         if exist('CH1') chdat(1).amp = CH1'; clear CH1; end ...
                            % signal pulse array in volts
107         if exist('CH2') chdat(2).amp = CH2'; clear CH2; end ...
                            % signal pulse array in volts
108         if exist('CH3') chdat(3).amp = CH3'; clear CH3; end ...
                            % signal pulse array in volts
109         if exist('CH4') chdat(4).amp = CH4'; clear CH4; end ...
                            % signal pulse array in volts
110
111         chdat = ApplyTriggerThreshold(chdat);
112         chdat = Resize_DataMat(chdat,MaxNumTrigger);
113     else
114       msgbox('ERROR in CRT_ana: unknown data format');
115       return
116     end
117
118     disp([' >>>> Ready.']);
119
120   end
121
122   if chCRT==4
123     lecroy_data = 1;
124     WCD_data = 0;
125
```

```
126     % Select data files acquired using the WCD DAQ Card Window XP ...
            system
127     %=============================================
128     WCD_dir_bin = '\\\aaa\aaa\';     %' see getdata_schottLYSO.m
129     WCD_dir_mat = pwd;
130   end
131
132   if chCRT==5
133     CRT_ana_parms;
134   end
135
136   if chCRT==7
137
138     if lecroy_data==1 & WCD_data==0
139        ana_lecroyCRT;
140     end
141
142   end
143
144   if chCRT==8
145
146     if lecroy_data==1 & WCD_data==0
147        en1min = win511_min(1);
148        en1max = win511_max(1);
149        en2min = win511_min(2);
150        en2max = win511_max(2);
151        pl_lecroyCRT;
152     end
153
154   end
155
156   if chCRT==9
```

```
157
158     if lecroy_data==1 & WCD_data==0
159        en1min = win511_min(1);
160        en1max = win511_max(1);
161        en2min = win511_min(2);
162        en2max = win511_max(2);
163       pl_pulseShapeChar;
164     end
165
166   end
167
168
169 end
170
171 pulse=CH3(1,:);
172 % pre-defined parameters
173 % N = Butt_N(ich);       % Butt_N = [1 1 1 1]; filter order
174 % f1 = Butt_f1(ich);     % Butt_f1 = [1e6 1e6 5e6 5e6]; low ...
       cut-off freq
175 % f2 = Butt_f2(ich);     % upper cut-off freq
176 % Ns = length(pulse);    % number of data samples
177 % Fs = Butt_Fs(ich);     % Butt_Fs = [50e6 50e6 50e6 50e6]; data ...
       sampling freq
178 N = 1;
179 f1 = 1e6;
180 f2 = 200e6;
181 Ns = 2000;
182 Fs = 1000e6;
183 tdat=[1:Ns]*Fs/Ns;
184 Fsamp=Fs;
185 %
186 %tt = ['Ch.',num2str(ich),':, N=',num2str(N),', ...
```

```
      f1=',num2str(f1/1e6),...
187 %      'MHz, f2=',num2str(f2/1e6),'MHz, Ns=',num2str(Ns),', ...
      Fs=',num2str(Fs/1e9),'GHz'];
188
189 % get filter parameters
190 [H,F,Bnum,Aden]=getBPfilter(N,f1,f2,Ns,Fs);
191 % This gets the filter parameters- the B and A of the transfer ...
      function
192
193 % make sure data 'pulse' has baseline removed before calling ...
      Matlab 'filter' function
194 pulseFiltered = filter(Bnum,Aden,pulse);
195 plot(pulseFiltered)
196
197 % FFT of pulse before and after filtering
198 tsamp = 1/Fs;
199 [freq1,psd1,dataFilt1,psdFilt1] = getPSD(pulse,tsamp,0,0);
200 [freq2,psd2,dataFilt2,psdFilt2] = getPSD(pulseFiltered,tsamp,0,0);
201
202
203
204
205
206 ichh = 1;
207
208 subplot(2,2,ichh);
209 plot(tdat,pulse,'b.-');
210 hold on; plot(tdat,pulseFiltered*1,'r.-'); hold off;
211 xlabel('Time (\mus)');
212 ylabel('amp (volts)');
213 legend('Original','Filtered');
214 %title(['Ch.',num2str(ich),' pulse']);
```

```
215
216 subplot(2,2,ichh+2);
217 %semilogy(freq1/1e6,psd1,'b-');
218 loglog(freq1/1e6,psd1,'b-');
219 hold on; semilogy(freq2/1e6,psd2,'r-'); hold off;
220 xlabel('Frequency (MHz)'); ylabel('PSD');
221 legend('Original','Filtered');
222 axis([1 Fsamp/1e6/2 1e-10 max(psd1)*5])
223 %title(tt);
```

Appendix C. MATLAB Code - Filter Analysis

```
clc;
clear all;
for f=1:1;
data=[];
downsample_factor = 10; % Downsampling factor
discrimination_level = .010; %Discrimination level in volts
plot_traces = 0; % PLOT ALL OF THE WAVEFORMS? THIS CAN GET MESSY...
plot_filter = 1; % plot filter analysis?
analyze =0; % just plot traces, or perform analysis?
index = 0; %iterative number
matrix_index = 1; % index for total data
maximum=[]; % peak location for each waveform
downdata_total = [];
tail_steps = 20; %number of steps to integrate tail pulse
left_steps = 5; %number of steps to integrate left
A= [1183;4053]; % [neutron;gamma]
for kk = 1:numel(A); % 1 to 12
    k = A(kk);  % Linear indexing on a 2D matrix
  if mod(k,1000) == 0;
      progress = k
  end
  index = index + 1;
  data=[data dlmread(sprintf('C2Trace%05d.dat',k))];
  downdata = downsample(data,downsample_factor);
  len_downdata = length(downdata);
  for m = 1:len_downdata
      if downdata(m,2)<0
          downdata(m,2) =0;
      end
```

```
30    end
31    downdata_total(:,matrix_index)=downdata(:,1);
32    matrix_index = matrix_index +1 ;
33    downdata_total(:,matrix_index) = downdata(:,2);
34    matrix_index = matrix_index +1;
35    max = 0;
36    for j= 1:len_downdata
37        if downdata(j,2) > max
38            maximum(index,1)= j;
39            max = downdata(j,2);
40        end
41        amplitude(index) = max;
42    end
43  Fs = 2000000000;
44  %ff = (f*.012)*1e6; % filter cutoff frequency
45  ff = 360000;
46  lpFilt = ...
        designfilt('lowpassiir','FilterOrder',2,'PassbandFrequency',ff, ...
        ...
47       'PassbandRipple',0.2,'SampleRate',Fs);
48  %fvtool(lpFilt) %to view filter response
49  y(kk,:) = filter(lpFilt,downdata(:,2));
50  plot(downdata(:,1),downdata(:,2),downdata(:,1),y(kk,:))
51  hold on
52  legend('original','filtered')
53  %wvtool(downdata(:,2)) %to view waveform response
54  clear max
55  if kk==1
56       max_n = max(downdata(:,2))
57       max_n_filtered = max(y(kk,:))
58  else
59       max_g = max(downdata(:,2))
```

```
60      max_g_filtered = max(y(kk,:))
61      orig_diff = max_n - max_g
62      filter_diff = max_n_filtered - max_g_filtered
63      filterdata(f,1) = ff;
64      filterdata(f,2) = orig_diff;
65      filterdata(f,3) = filter_diff;
66  end
67  if plot_traces == 1
68  figure(1)
69   plot(downdata(:,1),downdata(:,2))
70   set(gca,'FontSize',14)
71   ylabel('Amplitude [V]','FontSize',16,'FontWeight','bold')
72   xlabel('Time [s]','FontSize',16,'FontWeight','bold')
73   title('Waveforms','FontSize',18,'FontWeight','bold')
74   xlim([-1e-6 3e-6])
75   hold on
76  end
77   data = [];
78  end
79  end
80  ideal_filter = max(filterdata(:,3))
81  if plot_filter == 1
82  figure(10)
83   plot(filterdata(:,1),filterdata(:,2)
84   set(gca,'FontSize',14)
85   ylabel('Amplitude Difference [V]','FontSize',16,'FontWeight','bold')
86   xlabel('Frequency [Hz]','FontSize',16,'FontWeight','bold')
87   %title('LP Filter Analysis','FontSize',18,'FontWeight','bold')
88   %xlim([-1e-6 3e-6])
89   legend('Original','Filtered')
90   figure(11)
91   plot(downdata_total(:,1),downdata_total
```

```
92   set(gca,'FontSize',14)
93   ylabel('Amplitude [V]','FontSize',16,'FontWeight','bold')
94   xlabel('Time [s]','FontSize',16,'FontWeight','bold')
95   %title('LP Filter Analysis','FontSize',18,'FontWeight','bold')
96   xlim([-1e-6 4e-6])
97   legend('Neutron','Gamma')
98   figure(12)
99   plot(downdata_total(:,1),y(1,:),'x',downdata_total(:,1),y(2,:),'o')
100  set(gca,'FontSize',14)
101  ylabel('Amplitude [V]','FontSize',16,'FontWeight','bold')
102  xlabel('Time [s]','FontSize',16,'FontWeight','bold')
103  %title('LP Filter Analysis','FontSize',18,'FontWeight','bold')
104  xlim([-1e-6 4e-6])
105  legend('Neutron','Gamma')
106 end
107 if analyze ==1;
108 % at this point, index is equal to the total number of pulses
109 % at this point, len_downdata is equal to the number of points ...
       making the
110 % waveform
111 integral = zeros(index,2);
112 tail = zeros(index,1);
113 PSD = zeros(index,1);
114 prompt = zeros(index,1);
115 left_starts = zeros(index,1);
116 right_ends = zeros(index,1);
117 waveform = 2; % index of the amplitude of waveform in downdata_total
118 for i= 1:index
119     left_start = maximum(i,1) - left_steps;
120     right_end = maximum(i,1) + tail_steps;
121     left_starts(i,1) = left_start;
122     right_ends(i,1) = right_end;
```

```
123     if left_start < 1
124         left_start = 1;
125     end
126     if right_end > len_downdata
127         right_end = len_downdata;
128     end
129 
130     %for j= left_start : right_end
131      %   integral(i) = downdata_total(j,i*2) + integral(i);
132     %end
133     for j= 0 : maximum(i)-1
134         count = maximum(i) - j;
135         prompt(i) = downdata_total(count,i*2) + prompt(i);
136         if downdata_total(count,i*2) < discrimination_level
137             break
138         end
139     end
140     for j= maximum(i) : len_downdata
141         tail(i) = downdata_total(j,i*2) + tail(i);
142         if downdata_total(j,i*2) < discrimination_level
143             break
144         end
145     end
146     integral(i,1) = prompt(i) + tail(i);
147     number(i) = i;
148     PSD(i) = tail(i)/prompt(i);
149 end
150 figure(90)
151         RRR=plot(number(:),integral(:,1));
152         ax=gca;
153         ax.Box = 'off';
154         xlabel('Time [A.U.]','FontSize',14,'FontWeight','bold')
```

```
155         ylabel('Integrated Energy ...
                [A.U.]','FontSize',14,'FontWeight','bold')
156         %title('Gaussian Fit ...
                (Gamma)','FontSize',16,'FontWeight','bold')
157         ax=gca;
158         ax.FontName = 'LaTeX';
159         %ax.Title.Interpreter = 'LaTeX';
160         %ax.XLabel.Interpreter = 'LaTeX';
161         %ax.YLabel.Interpreter = 'LaTeX';
162         ax.Box = 'on';
163         ax.LineWidth = 1.5;
164         ax.FontSize = 14;
165         ax.FontWeight = 'bold';
166 % identify if the particle is neutron (2), gamma (1) or pile-up (3)
167 gamma_cutoff = 1.0; % integrated energy cutoff of gammas
168 neutron_cutoff = 8.0; %integrated energy cutoff of neutrons
169 gamma_cutoff2 = 1.4;
170 amplitude_cutoff = 0.19;
171 for i=1:index
172     if integral(i,1) ≤ gamma_cutoff
173         integral(i,2) = 1;
174     elseif integral(i,1) ≤ gamma_cutoff2 && amplitude(1,i) ≥ ...
            amplitude_cutoff
175         integral(i,2) = 1;
176     elseif integral(i,1) ≤ gamma_cutoff2 && amplitude(1,i) < ...
            amplitude_cutoff
177         integral(i,2) = 2;
178     elseif integral(i,1) > gamma_cutoff2 && integral(i,1) < ...
            neutron_cutoff
179         integral (i,2) = 2;
180     else
181         integral (i,2) = 3;
```

```
182     end
183 end
184     x_blue = amplitude(integral(:,2)==1);
185     y_blue = integral(integral(:,2)==1);
186     x_red = amplitude(integral(:,2)==2);
187     y_red = integral(integral(:,2)==2);
188     x_green = amplitude(integral(:,2)==3);
189     y_green = integral(integral(:,2)==3);
190 figure(96)
191     scatter(x_red,y_red,'.','r')
192     hold on
193     scatter(x_blue,y_blue,'.','b')
194     scatter(x_green,y_green,'.','g')
195     hold off
196     %LLLL = scatter(amplitude(:),integral(:),'.','k')
197     %LLLLL = scatter(amplitude(:),integral(:),'.','k')
198     %set(gca,'FontSize',20)
199     xlabel('Amplitude [V]','FontSize',14,'FontWeight','bold')
200     ylabel('Integrated Energy ...
            [A.U]','FontSize',14,'FontWeight','bold')
201     %title('Pulse Shape ...
            Discrimination','FontSize',16,'FontWeight','bold')
202     ylim([0 7])
203     ax=gca;
204     ax.FontName = 'LaTeX';
205     %ax.Title.Interpreter = 'LaTeX';
206     %ax.XLabel.Interpreter = 'LaTeX';
207     %ax.YLabel.Interpreter = 'LaTeX';
208     ax.Box = 'on';
209     ax.LineWidth = 1.5;
210     ax.FontSize = 14;
211     ax.FontWeight = 'bold';
```

```
212     leg = legend('NEUTRON (RED)','GAMMA (BLUE)');
213     %set(leg,'MarkerSize','20');
214
215 D1 = .7; %First place to divide histogram
216 D2 = 4.1; %Second place to divide histogram
217 figure(97)
218         [YY NN]=hist(integral(:,1),100); % YY values, NN bin centers
219         ind = NN > D1;
220         ind2 = NN > D2;
221         bar(NN(ind), YY(ind), 1, 'r'); %// for greater: use red
222         hold on %// keep graph, Or use hold(your_axis_handle, 'on')
223         bar(NN(¬ind), YY(¬ind), 1, 'b'); %// for smaller: use blue
224         hold on %// keep graph, Or use hold(your_axis_handle, 'on')
225         bar(NN(ind2), YY(ind2), 1, 'g'); %// for smaller: use blue
226         %set(gca,'FontSize',20)
227         xlabel('Integrated Energy ...
                [A.U.]','FontSize',14,'FontWeight','bold')
228         ylabel('Counts','FontSize',14,'FontWeight','bold')
229         %title('Waveform Analysis','FontSize',16,'FontWeight','bold')
230         ax=gca;
231         ax.FontName = 'LaTeX';
232         %ax.Title.Interpreter = 'LaTeX';
233         %ax.XLabel.Interpreter = 'LaTeX';
234         %ax.YLabel.Interpreter = 'LaTeX';
235         ax.Box = 'on';
236         ax.LineWidth = 1.5;
237         ax.FontSize = 14;
238         ax.FontWeight = 'bold';
239         hold on;
240 %plot(0,0,'ob');
241 %plot(0,0,'or');
242 %plot(0,0,'og');
```

```
243 leg = legend('NEUTRON','GAMMA','PILE-UP');
244 % THIS SECTION LOOKS AT THE DIVISION OF PEAKS IN THE HISTOGRAM
245
246
247 gamma_counter = 1;
248 neutron_counter = 1;
249 gamma = [];
250 neutron = [];
251 for i=1:index
252     if integral(i,1) < gamma_cutoff
253         gamma(gamma_counter) = integral(i,1);
254         gamma_counter = gamma_counter + 1;
255     elseif integral(i,1) < neutron_cutoff
256         neutron(neutron_counter) = integral(i,1);
257         neutron_counter = neutron_counter +1;
258     end
259 end
260 figure(98)
261         NNN=histfit(gamma(1,:),100);
262         ax=gca;
263         ax.Box = 'off';
264         xlabel('Integrated Energy ...
              [A.U.]','FontSize',14,'FontWeight','bold')
265         ylabel('Counts','FontSize',14,'FontWeight','bold')
266         %title('Gaussian Fit ...
              (Gamma)','FontSize',16,'FontWeight','bold')
267         ax=gca;
268         ax.FontName = 'LaTeX';
269         %ax.Title.Interpreter = 'LaTeX';
270         %ax.XLabel.Interpreter = 'LaTeX';
271         %ax.YLabel.Interpreter = 'LaTeX';
272         ax.Box = 'on';
```

```
273         ax.LineWidth = 1.5;
274         ax.FontSize = 14;
275         ax.FontWeight = 'bold';
276 figure(99)
277         OOO=histfit(neutron(1,:),100);
278         %set(gca,'FontSize',20)
279         xlabel('Integrated Energy ...
                [A.U]','FontSize',14,'FontWeight','bold')
280         ylabel('Counts','FontSize',14,'FontWeight','bold')
281         %title('Gaussian Fit ...
                (Neutron)','FontSize',16,'FontWeight','bold')
282         ax=gca;
283         ax.FontName = 'LaTeX';
284         %ax.Title.Interpreter = 'LaTeX';
285         %ax.XLabel.Interpreter = 'LaTeX';
286         %ax.YLabel.Interpreter = 'LaTeX';
287         ax.Box = 'on';
288         ax.LineWidth = 1.5;
289         ax.FontSize = 14;
290         ax.FontWeight = 'bold';
291
292
293 gamma_new= transpose(gamma(1,:));
294 neutron_new= transpose(neutron(1,:));
295 pd_gamma = fitdist(gamma_new(:),'Normal')
296 pd_neutron = fitdist(neutron_new(:),'Normal')
297 centroid_gamma = mean(gamma(1,:))
298 centroid_neutron = mean(neutron(1,:))
299 FWHM_n=pd_neutron.sigma * 2.35;
300 FWHM_g=pd_gamma.sigma * 2.35;
301 D = centroid_neutron - centroid_gamma;
302 FOM = D/(FWHM_n + FWHM_g)
```

```
303 end
304
305       0.0701
```

Appendix D. MCNP6 Simulation

```
1  FordLICAF_Spec.txt This code runs the entire spectrometer
2  c
3  c cell cards
4  100  1 -0.001255 -10 21 22 23 24 25 26 27 28 29 30 &
5                 31 32 33 34 35 36 37 38 39 40 &
6                     imp:n=1 imp:p=0 $air
7  201  2 -0.941    -21       imp:n=1 imp:p=0 $Poly cell 1
8  301  3 -1.859    -31       imp:n=1 imp:p=1 $LiCAF cell 1
9  202  2 -0.941    -22       imp:n=1 imp:p=0 $Poly cell 2
10 302  3 -1.859    -32       imp:n=1 imp:p=1 $LiCAF cell 2
11 203  2 -0.941    -23       imp:n=1 imp:p=0 $Poly cell 3
12 303  3 -1.859    -33       imp:n=1 imp:p=1 $LiCAF cell 3
13 204  2 -0.941    -24       imp:n=1 imp:p=0 $Poly cell 4
14 304  3 -1.859    -34       imp:n=1 imp:p=1 $LiCAF cell 4
15 205  2 -0.941   -25       imp:n=1 imp:p=0 $Poly cell 5
16 305  3 -1.859   -35    imp:n=1 imp:p=1 $LiCAF cell 5
17 206  2 -0.941   -26       imp:n=1 imp:p=0 $Poly cell 6
18 306  3 -1.859   -36    imp:n=1 imp:p=1 $LiCAF cell 6
19 207  2 -0.941   -27       imp:n=1 imp:p=0 $Poly cell 7
20 307  3 -1.859   -37    imp:n=1 imp:p=1 $LiCAF cell 7
21 208  2 -0.941   -28       imp:n=1 imp:p=0 $Poly cell 8
22 308  3 -1.859   -38    imp:n=1 imp:p=1 $LiCAF cell 8
23 209  2 -0.941   -29       imp:n=1 imp:p=0 $Poly cell 9
24 309  3 -1.859   -39    imp:n=1 imp:p=1 $LiCAF cell 9
25 210  2 -0.941   -30       imp:n=1 imp:p=0 $Poly cell 10
26 310  3 -1.859   -40    imp:n=1 imp:p=1 $LiCAF cell 10
27
28 999  0 10                 imp:n=0 imp:p=0 $outside
29
```

```
c SURFACE CARDS
10   rpp -10 10 -10 10 -10 100      $ problem boundary
21   rpp -5 5 -5 5 49.999 50.00     $ Poly surface #1, .001cm thick
31   rpp -5 5 -5 5 49.50 49.999     $ Licaf surface #1, 4.999mm thick
22   rpp -5 5 -5 5 48.25 49.50      $ Poly surface #2, 1.25cm thick
32   rpp -5 5 -5 5 47.75 48.25      $ Licaf surface #2, 5.0mm thick
23   rpp -5 5 -5 5 46.50 47.75      $ Poly surface #3, 1.25cm thick
33   rpp -5 5 -5 5 46.00 46.50      $ Licaf surface #3, 5.0mm thick
24   rpp -5 5 -5 5 44.75 46.00      $ Poly surface #4, 1.25cm thick
34   rpp -5 5 -5 5 44.25 44.75      $ Licaf surface #4, 5.0mm thick
25   rpp -5 5 -5 5 43.00 44.25      $ Poly surface #5, 1.25cm thick
35   rpp -5 5 -5 5 42.50 43.00      $ Licaf surface #5, 5.0mm thick
26   rpp -5 5 -5 5 41.25 42.50      $ Poly surface #6, 1.25cm thick
36   rpp -5 5 -5 5 40.75 41.25      $ Licaf surface #6, 5.0mm thick
27   rpp -5 5 -5 5 39.50 40.75      $ Poly surface #7, 1.25cm thick
37   rpp -5 5 -5 5 39.00 39.50      $ Licaf surface #7, 5.0mm thick
28   rpp -5 5 -5 5 37.75 39.00      $ Poly surface #8, 1.25cm thick
38   rpp -5 5 -5 5 37.25 37.75      $ Licaf surface #8, 5.0mm thick
29   rpp -5 5 -5 5 36.00 37.25      $ Poly surface #9, 1.25cm thick
39   rpp -5 5 -5 5 35.50 36.00      $ Licaf surface #9, 5.0mm thick
30   rpp -5 5 -5 5 34.25 35.50      $ Poly surface #10, 1.25cm thick
40   rpp -5 5 -5 5 33.75 34.25      $ Licaf surface #10, 5.0mm thick

c DATA CARDS
m1   07014 0.778   07015 0.00286  &
     8016  0.20896                                          $ air
m2   6000 2   1000 4                                        $ HDPE ...
    High Density Polyethylene
m3   3006 125.4   3007 6.6 &
     9000 264.0   20000 44.0 &
     13000 44.0   14000 61.6 &
     8016 61.6   6012 123.2 &
```

```
61      1000 369.6                                                  $ ...
           Enriched, rubberized LICAF
62
63 mode n a          $we are transporting neutrons = n
64 SDEF x=D1 y=D2 z=99 PAR=n ERG=1 VEC 0 0 -1 DIR=1     $position, ...
      type, and MeV, vector, and cosine of the angle of the cone (no ...
      cone in this case)
65 si1  H -5 5
66 sp1  0 1
67 si2  H -5 5
68 sp2  0 1
69 nps  10000000      $number of source particles
70 f4:n 400      $count # that crosses a surface, into detector
```

Appendix E. MAXED Input Deck (AFIT Data)

5.1 Data File (dat_spec_L.ibu)

```
1
2   0   *         d         cts / s
3       10     0      File dat_spec_L.ibu / reference see end of file
4   0W0          1.0       1.059E+05       3.254E+02     .310      1.0      0
5   0W1          2.0       1.732E+05       4.162E+02     .240      1.0      1
6   0W2          3.0       2.397E+05       4.896E+02     .200      1.0      2
7   0W3          4.0       2.380E+05       4.879E+02     .200      1.0      3
8   0W4          5.0       1.983E+05       4.453E+02     .220      1.0      4
9   0W5          6.0       1.633E+05       4.040E+02     .250      1.0      5
10  0W6          7.0       1.240E+05       3.521E+02     .280      1.0      6
11  0W7          8.0       8.264E+04       2.875E+02     .350      1.0      7
12  0W8          8.0       5.709E+04       2.389E+02     .420      1.0      8
13  0W9          9.0       2.399E+04       1.549E+02     .650      1.0      9
14
15
16  Dete       Diam       reading M         abs unc    % unc     % unc
17  ctor       eter      count rate            of M     of M     of R   flag
18
19  12341234----.-123456789.12345---------.12345-----.12-----.12I23456
20
21  Format line 1:
22   1000   FORMAT(20A4)
23
24  Format line 2: NOD, rdummy       NOD = number of detectors
25   1020   FORMAT( * )
26
27  Format line 3 to NOD+2
```

```
28  1030  FORMAT(2A4,F6.1,2E15.5,2F8.2,I6)
29
30
31 Make sure to change the uncertainties of the data. These are the ...
       same values that were previously used
32
33 The second zero in the second row is the data correction factor, ...
       this needs to be changed.
```

5.2 Default Spectrum (def_spec_L.flu)

```
1
2   File def_spec_L.flu (norm.  exa.3: AHB50E.S11) / 25.11.2001
3            2          1                        fluence  given in ...
                 1/cm^2/MeV
4            2         23          23   10.00E+00
5     1.000E-03  1.0000E+01   1.0000E+00
6     1.000E-02  1.0000E+01   1.0000E+00
7     1.000E-01  1.0000E+01   1.0000E+00
8     5.000E-01  1.0000E+00   1.0000E+00
9     1.000E+00  1.0000E+00   1.0000E+00
10    1.500E+00  1.0000E+00   1.0000E+00
11    2.000E+00  1.0000E+03   1.0000E+02
12    2.500E+00  1.0000E+06   3.1600E+03
13    3.000E+00  1.0000E+03   1.0000E+02
14    3.500E+00  1.0000E+00   1.0000E+00
15    4.000E+00  1.0000E+00   1.0000E+00
16    4.500E+00  1.0000E+00   1.0000E+00
17    5.000E+00  1.0000E+00   1.0000E+00
18    5.500E+00  1.0000E+00   1.0000E+00
```

```
 6.000E+00  1.0000E+00   1.0000E+00
 6.500E+00  1.0000E+00   1.0000E+00
 7.000E+00  1.0000E+00   1.0000E+00
 7.500E+00  1.0000E+00   1.0000E+00
 8.000E+00  1.0000E+00   1.0000E+00
 8.500E+00  1.0000E+00   1.0000E+00
 9.000E+00  1.0000E+00   1.0000E+00
 9.500E+00  1.0000E+00   1.0000E+00
 10.00E+00  1.0000E+00   1.0000E+00
```

5.3 Input Deck (mxfc_con_L.inp)

```
 dat_spec_L.ibu                                  File with measured data
 resp_fun_L.fmt                                  File with response ...
     functions (RF)
 afit_009                                       Name of output file
 def_spec_L.flu                                  File with default ...
     spectrum (DS)
 10.                                             Highest energy (use ...
     energy units of RF)
 1.0                                            requested final CHI^2 ...
     P.D.F.
 1.0,0.30                                       temperature, temp. ...
     reduction fact.
 3,2                                            2 = use the response ...
     energy bins, 2 = EdF/dE
 1                                              1 = scale DS
 0                                              0 = use the MAXED DS ...
     scale factor
```

5.4 Response Functions (resp_fun_L.fmt)

```
1
2         DECEM-03-2012    *** ATTENTION: This file was specially ...
             compiled for UMG33
3  Neutron Response Functions for BS with  5 enrg/decade, units: ...
      cm^2, pSv, pSv cm^2
4           23   1
5   1.000E-03 1.000E-02 1.000E-01 0.500E+00 1.000E+00 1.500E+00 ...
       2.000E+00 2.500E+00
6   3.000E+00 3.500E+00 4.000E+00 4.500E+00 5.000E+00 5.500E+00 ...
       6.000E+00 6.500E+00
7   7.000E+00 7.500E+00 8.000E+00 8.500E+00 9.000E+00 9.500E+00 ...
       10.00E+00
8           0
9           10
10  0W0        B_A*H Wgl  0d200    R-M by FORD, 03.20.2018
11   1.000E+02      cm^2         0         0    3    1    1    0
12   1.120E+06 7.904E+05 4.870E+05 2.895E+05 1.949E+05 1.513E+05 ...
       1.232E+05 1.027E+05
13   8.656E+04 7.691E+04 7.087E+04 6.483E+04 6.124E+04 5.397E+04 ...
       5.044E+04 4.766E+04
14   4.235E+04 4.091E+04 3.832E+04 3.482E+04 3.574E+04 3.407E+04 ...
       3.313E+04
15  0W1        B_A*H Wgl iso200    R-M by FORD, 03.20.2018
16   1.000E+02      cm^2         0         0    3    1    1    0
17   1.324E+06 1.033E+06 7.627E+05 5.117E+05 3.606E+05 2.822E+05 ...
       2.288E+05 1.910E+05
```

```
 1.630E+05 7.628E+04 1.314E+05 1.215E+05 1.125E+05 1.020E+05 ...
    9.449E+04 8.799E+04
 7.886E+04 6.491E+03 7.170E+04 6.517E+04 6.415E+04 6.095E+04 ...
    5.804E+04
0W2       B_A*H Wgl 90d200    R-M by FORD, 03.20.2018
 1.000E+02      cm^2         0         0    3    1    1    0
 7.144E+05 6.280E+05 5.988E+05 4.972E+05 3.855E+05 3.180E+05 ...
    2.651E+05 2.241E+05
 1.948E+05 1.691E+05 1.577E+05 1.467E+05 1.371E+05 1.253E+05 ...
    1.166E+05 1.087E+05
 9.799E+04 9.364E+04 8.862E+04 8.144E+04 7.909E+04 7.486E+04 ...
    7.159E+04
0W3       CDA*H Wgl  0d200    R-M by FORD, 03.20.2018
 1.000E+02      cm^2         0         0    3    1    1    0
 3.309E+05 3.098E+05 3.568E+05 3.775E+05 3.318E+05 2.931E+05 ...
    2.533E+05 2.190E+05
 1.966E+05 1.672E+05 1.588E+05 1.398E+05 1.420E+05 1.313E+05 ...
    1.230E+05 1.157E+05
 1.050E+05 9.834E+04 9.363E+04 8.690E+04 8.361E+04 7.977E+04 ...
    7.630E+04
0W4       CDA*H Wgl iso200    R-M by FORD, 03.20.2018
 1.000E+02      cm^2         0         0    3    1    1    0
 1.438E+05 1.396E+05 1.843E+05 2.486E+05 2.487E+05 2.379E+05 ...
    2.167E+05 1.914E+05
 1.773E+05 1.487E+05 1.437E+05 1.200E+05 1.333E+05 1.246E+05 ...
    1.174E+05 1.110E+05
 1.019E+05 9.463E+04 9.046E+04 8.586E+04 8.252E+04 7.929E+04 ...
    7.618E+04
0W5       CDA*H Wgl 90d200    R-M by FORD, 03.20.2018
 1.000E+02      cm^2         0         0    3    1    1    0
 6.096E+04 6.025E+04 8.736E+04 1.474E+05 1.695E+05 1.771E+05 ...
    1.701E+05 1.552E+05
```

```
 1.476E+05 1.217E+05 1.211E+05 9.810E+04 1.165E+05 1.106E+05 ...
    1.049E+05 1.003E+05
 9.304E+04 8.513E+04 8.137E+04 7.872E+04 7.489E+04 7.213E+04 ...
    7.031E+04
0W6       3.0INCH*H Wgl       R-M by FORD, 03.20.2018
 1.000E+02      cm^2         0         0    3    1    1    0
 2.547E+04 2.524E+04 3.873E+04 8.090E+04 1.083E+05 1.234E+05 ...
    1.248E+05 1.183E+05
 1.170E+05 9.434E+04 9.683E+04 7.484E+04 9.660E+04 9.291E+04 ...
    8.879E+04 8.583E+04
 8.036E+04 7.179E+04 6.934E+04 6.874E+04 6.544E+04 6.328E+04 ...
    6.208E+04
0W7       3.5INCH*H Wgl       R-M by FORD, 03.20.2018
 1.000E+02      cm^2         0         0    3    1    1    0
 1.023E+04 1.017E+04 1.665E+04 4.211E+04 6.509E+04 8.149E+04 ...
    8.706E+04 8.446E+04
 8.645E+04 6.851E+04 7.228E+04 7.484E+04 7.557E+04 7.301E+04 ...
    7.011E+04 6.887E+04
 6.505E+04 5.695E+04 5.527E+04 5.585E+04 5.334E+04 5.152E+04 ...
    5.075E+04
0W8       3.5INCH*H Wgl       R-M by FORD, 03.20.2018
 1.000E+02      cm^2         0         0    3    1    1    0
 4.075E+03 4.067E+03 7.005E+03 2.065E+04 3.557E+04 4.943E+04 ...
    5.484E+04 5.537E+04
 5.789E+04 4.569E+04 4.855E+04 5.146E+04 5.238E+04 5.108E+04 ...
    4.962E+04 4.940E+04
 4.720E+04 4.086E+04 3.972E+04 4.116E+04 3.913E+04 3.814E+04 ...
    3.743E+04
0W9       3.5INCH*H Wgl       R-M by FORD, 03.20.2018
 1.000E+02      cm^2         0         0    3    1    1    0
 1.548E+03 1.554E+03 2.597E+03 8.108E+03 1.545E+04 2.217E+04 ...
    2.522E+04 2.568E+04
```

```
58  2.735E+04 2.133E+04 2.332E+04 2.480E+04 2.544E+04 2.501E+04 ...
       2.483E+04 2.453E+04
59  2.332E+04 2.013E+04 1.962E+04 2.045E+04 1.964E+04 1.920E+04 ...
       1.923E+04
```

Appendix F. MAXED Input Deck (UM Data)

6.1 Data File (dat_spec_L2.ibu)

```
1
2   0   *         d         cts / s
3       10     0      File dat_spec_L2.ibu / reference see end of file
4   0W0          1.0       1.506E+05       3.881E+02     2.60      7.0      0
5   0W1          2.0       2.631E+05       5.129E+02     1.90      7.0      1
6   0W2          3.0       2.882E+05       5.368E+02     1.90      7.0      2
7   0W3          4.0       2.073E+05       4.553E+02     2.20      7.0      3
8   0W4          5.0       1.280E+05       3.578E+02     2.80      7.0      4
9   0W5          6.0       7.894E+04       2.810E+02     3.60      7.0      5
10  0W6          7.0       6.650E+04       2.579E+02     3.90      7.0      6
11  0W7          8.0       4.980E+04       2.232E+02     4.50      7.0      7
12  0W8          8.0       1.130E+04       1.063E+02     9.40      7.0      8
13  0W9          9.0       5.342E+03       7.309E+01     13.7      7.0      9
14
15
16  Dete       Diam       reading M         abs unc    % unc     % unc
17  ctor       eter      count rate            of M     of M     of R   flag
18
19  12341234----.-123456789.12345---------.12345-----.12-----.12I23456
20
21  Format line 1:
22   1000   FORMAT(20A4)
23
24  Format line 2: NOD, rdummy       NOD = number of detectors
25   1020   FORMAT( * )
26
27  Format line 3 to NOD+2
```

```
1030  FORMAT(2A4,F6.1,2E15.5,2F8.2,I6)
```

6.2 Default Spectrum (def_spec_L.flu)

```
 File def_spec_L.flu (norm.  exa.3: AHB50E.S11) / 25.11.2001
           2          1                       fluence  given in ...
               1/cm^2/MeV
           2         23          23   10.00E+00
    1.000E-03  1.0000E+01   1.0000E+00
    1.000E-02  1.0000E+01   1.0000E+00
    1.000E-01  1.0000E+01   1.0000E+00
    5.000E-01  1.0000E+00   1.0000E+00
    1.000E+00  1.0000E+00   1.0000E+00
    1.500E+00  1.0000E+00   1.0000E+00
    2.000E+00  1.0000E+03   1.0000E+02
    2.500E+00  1.0000E+06   3.1600E+03
    3.000E+00  1.0000E+03   1.0000E+02
    3.500E+00  1.0000E+00   1.0000E+00
    4.000E+00  1.0000E+00   1.0000E+00
    4.500E+00  1.0000E+00   1.0000E+00
    5.000E+00  1.0000E+00   1.0000E+00
    5.500E+00  1.0000E+00   1.0000E+00
    6.000E+00  1.0000E+00   1.0000E+00
    6.500E+00  1.0000E+00   1.0000E+00
    7.000E+00  1.0000E+00   1.0000E+00
    7.500E+00  1.0000E+00   1.0000E+00
    8.000E+00  1.0000E+00   1.0000E+00
    8.500E+00  1.0000E+00   1.0000E+00
    9.000E+00  1.0000E+00   1.0000E+00
```

```
26      9.500E+00  1.0000E+00   1.0000E+00
27      10.00E+00  1.0000E+00   1.0000E+00
```

6.3 Input Deck (mxfc_con_L2.inp)

```
1
2  dat_spec_L2.ibu                                  File with measured ...
       data
3  resp_fun_L2.fmt                                  File with response ...
       functions (RF)
4  mxfc_006                                        Name of output file
5  def_spec_L.flu                                    File with default ...
       spectrum (DS)
6  10.                                              Highest energy (use ...
       energy units of RF)
7  1.0                                             requested final CHI^2 ...
       P.D.F.
8  1.0,0.85                                        temperature, temp. ...
       reduction fact.
9  3,2                                             2 = use the response ...
       energy bins, 2 = EdF/dE
10 1                                               1 = scale DS
11 0                                               0 = use the MAXED DS ...
       scale factor
```

6.4 Response Functions (resp_fun_L2.fmt)

```
1
```

```
        DECEM-03-2012    *** ATTENTION: This file was specially ...
            compiled for UMG33
Neutron Response Functions for BS with  5 enrg/decade, units: ...
    cm^2, pSv, pSv cm^2
         23   1
 1.000E-03 1.000E-02 1.000E-01 0.500E+00 1.000E+00 1.500E+00 ...
     2.000E+00 2.500E+00
 3.000E+00 3.500E+00 4.000E+00 4.500E+00 5.000E+00 5.500E+00 ...
     6.000E+00 6.500E+00
 7.000E+00 7.500E+00 8.000E+00 8.500E+00 9.000E+00 9.500E+00 ...
     10.00E+00
          0
          10
0W0       B_A*H Wgl  0d200    R-M by WIEGEL: NEMUS005.DAT, 14.12.2000
 1.000E+02      cm^2         0         0    3    1    1    0
 1.308E+06 9.562E+05 6.353E+05 4.023E+05 2.816E+05 2.224E+05 ...
     1.827E+05 1.534E+05
 1.303E+05 1.158E+05 1.048E+05 9.425E+04 8.848E+04 7.854E+04 ...
     7.382E+04 6.938E+04
 6.177E+04 5.976E+04 5.654E+04 5.054E+04 5.122E+04 4.841E+04 ...
     4.628E+04
0W1       B_A*H Wgl iso200    R-M by WIEGEL: NEMUS005.DAT, 14.12.2000
 1.000E+02      cm^2         0         0    3    1    1    0
 1.131E+06 9.490E+05 8.464E+05 6.837E+05 5.332E+05 4.414E+05 ...
     3.706E+05 3.134E+05
 2.736E+05 2.381E+05 2.179E+05 1.999E+05 1.864E+05 1.712E+05 ...
     1.596E+05 1.482E+05
 1.334E+05 1.282E+05 1.211E+05 1.099E+05 1.065E+05 1.012E+05 ...
     9.558E+04
0W2       B_A*H Wgl 90d200    R-M by WIEGEL: NEMUS005.DAT, 14.12.2000
 1.000E+02      cm^2         0         0    3    1    1    0
```

```
22  3.638E+05 3.417E+05 3.767E+05 4.381E+05 4.160E+05 3.832E+05 ...
       3.443E+05 3.044E+05
23  2.780E+05 2.351E+05 2.235E+05 2.123E+05 2.018E+05 1.879E+05 ...
       1.767E+05 1.663E+05
24  1.510E+05 1.415E+05 1.349E+05 1.256E+05 1.210E+05 1.155E+05 ...
       1.104E+05
25 0W3       CDA*H Wgl  0d200    R-M by WIEGEL: NEMUS005.DAT, 14.12.2000
26  1.000E+02      cm^2         0         0    3    1    1    0
27  1.018E+05 9.448E+04 1.211E+05 1.932E+05 2.279E+05 2.432E+05 ...
       2.379E+05 2.219E+05
28  2.155E+05 1.773E+05 1.764E+05 1.740E+05 1.696E+05 1.617E+05 ...
       1.538E+05 1.480E+05
29  1.374E+05 1.245E+05 1.197E+05 1.168E+05 1.104E+05 1.066E+05 ...
       1.033E+05
30 0W4       CDA*H Wgl iso200    R-M by WIEGEL: NEMUS005.DAT, 14.12.2000
31  1.000E+02      cm^2         0         0    3    1    1    0
32  2.704E+04 2.555E+04 3.469E+04 6.967E+05 1.039E+05 1.289E+05 ...
       1.399E+05 1.386E+05
33  1.440E+05 1.151E+05 1.213E+05 1.245E+05 1.274E+05 1.236E+05 ...
       1.192E+05 1.173E+05
34  1.120E+05 9.740E+04 9.452E+04 9.663E+04 9.139E+04 8.900E+04 ...
       8.738E+04
35 0W5       CDA*H Wgl 90d200    R-M by WIEGEL: NEMUS005.DAT, 14.12.2000
36  1.000E+02      cm^2         0         0    3    1    1    0
37  7.027E+03 6.731E+03 9.174E+03 2.203E+05 4.134E+04 6.158E+04 ...
       7.388E+04 7.888E+04
38  8.751E+04 6.811E+04 7.626E+04 8.263E+04 8.757E+04 8.723E+04 ...
       8.586E+04 8.665E+04
39  8.431E+04 7.099E+04 6.968E+04 7.502E+04 7.107E+04 6.999E+04 ...
       6.965E+04
40 0W6       3.0INCH*H Wgl       R-M by WIEGEL: NEMUS005.DAT, 14.12.2000
41  1.000E+02      cm^2         0         0    3    1    1    0
```

```
 1.829E+03 1.792E+03 2.340E+03 6.773E+03 1.552E+04 2.676E+04 ...
    3.675E+04 4.179E+04
 5.074E+04 3.736E+04 4.541E+04 5.191E+04 5.783E+04 5.935E+04 ...
    5.901E+04 6.171E+04
 6.177E+04 4.930E+04 4.855E+04 5.543E+04 5.293E+04 5.197E+04 ...
    5.256E+04
0W7       3.5INCH*H Wgl       R-M by WIEGEL: NEMUS005.DAT, 14.12.2000
 1.000E+02      cm^2         0         0    3    1    1    0
 4.580E+02 4.450E+02 6.590E+02 1.824E+03 5.260E+03 1.120E+04 ...
    1.775E+04 2.174E+04
 2.818E+04 1.996E+04 2.576E+04 3.073E+04 3.665E+04 3.858E+04 ...
    3.883E+04 4.169E+04
 4.332E+04 3.316E+04 3.261E+04 3.938E+04 3.762E+04 3.720E+04 ...
    3.793E+04
0W8       3.5INCH*H Wgl       R-M by WIEGEL: NEMUS005.DAT, 14.12.2000
 1.000E+02      cm^2         0         0    3    1    1    0
 1.270E+02 1.230E+02 1.540E+02 5.380E+02 1.753E+03 4.394E+03 ...
    7.701E+03 1.029E+04
 1.452E+04 9.740E+03 1.368E+04 1.734E+04 2.141E+04 2.303E+04 ...
    2.380E+04 2.614E+04
 2.756E+04 1.997E+04 1.995E+04 2.536E+04 2.397E+04 2.400E+04 ...
    2.480E+04
0W9       3.5INCH*H Wgl       R-M by WIEGEL: NEMUS005.DAT, 14.12.2000
 1.000E+02      cm^2         0         0    3    1    1    0
 2.800E+01 2.600E+01 3.800E+01 1.180E+02 5.110E+02 1.343E+03 ...
    2.462E+03 3.372E+03
 5.089E+03 3.280E+03 4.754E+03 6.284E+03 8.002E+03 8.836E+03 ...
    8.965E+03 1.007E+04
 1.097E+04 7.549E+03 7.714E+04 1.003E+04 9.681E+03 9.538E+03 ...
    9.983E+03
```

Appendix G. Raw Data

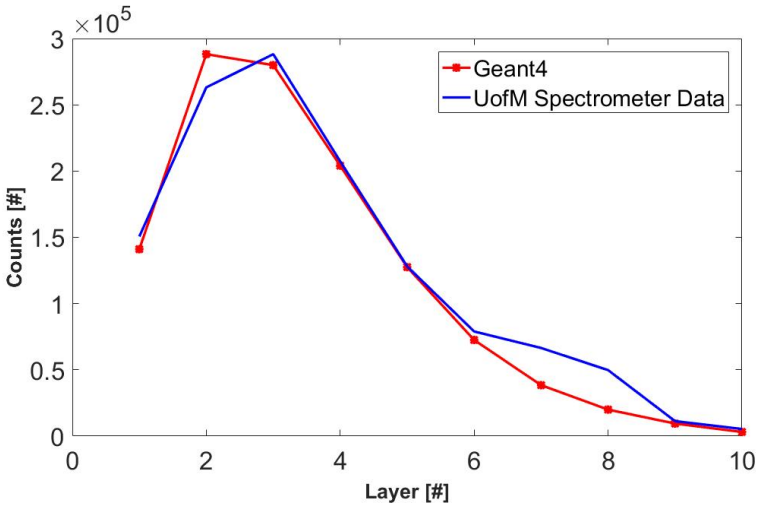

Figure 58. Comparison between Geant4 simulation and data taken after 1-hour spectrometer run at University of Michigan's DD generator.

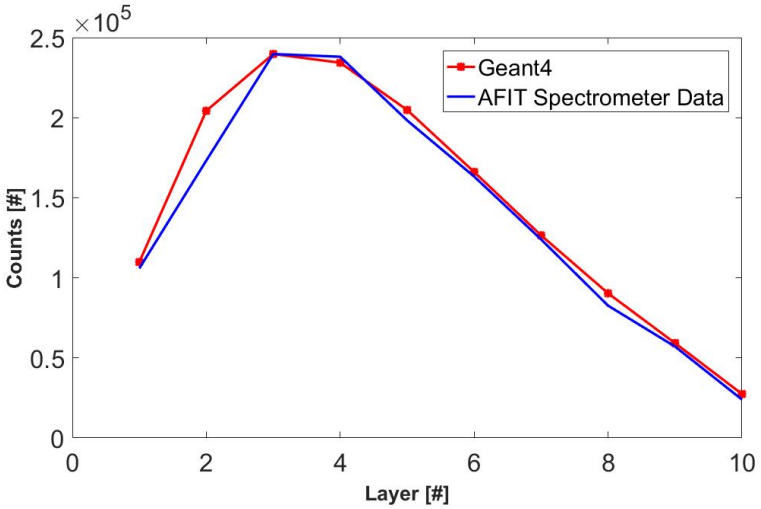

Figure 59. Comparison between Geant4 simulation and data taken after a 5-minute spectrometer run at AFIT's DD generator.

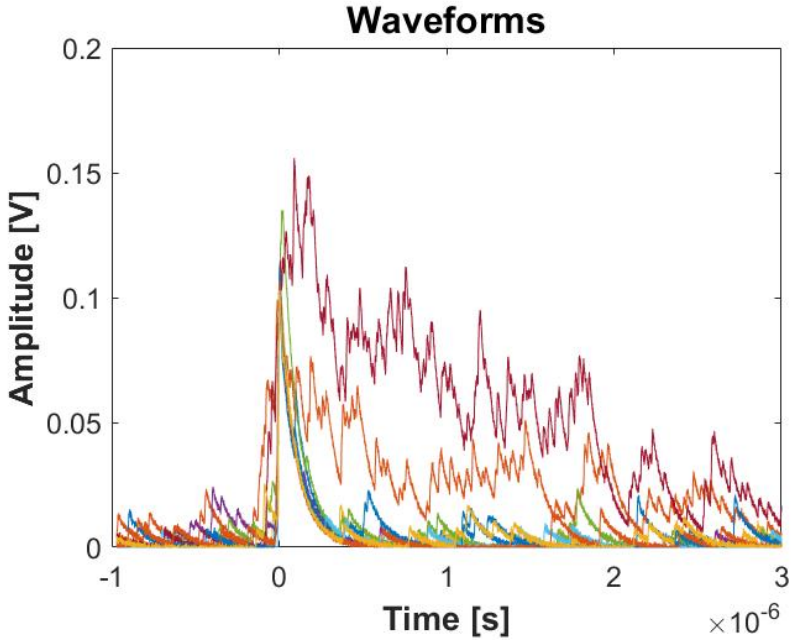

Figure 60. Raw data for spectrometer Eu:LiCAF wafer #1. This is a snapshot of the first 10 waveforms saved from the wafer during the calibration run at AFIT's DD generator.

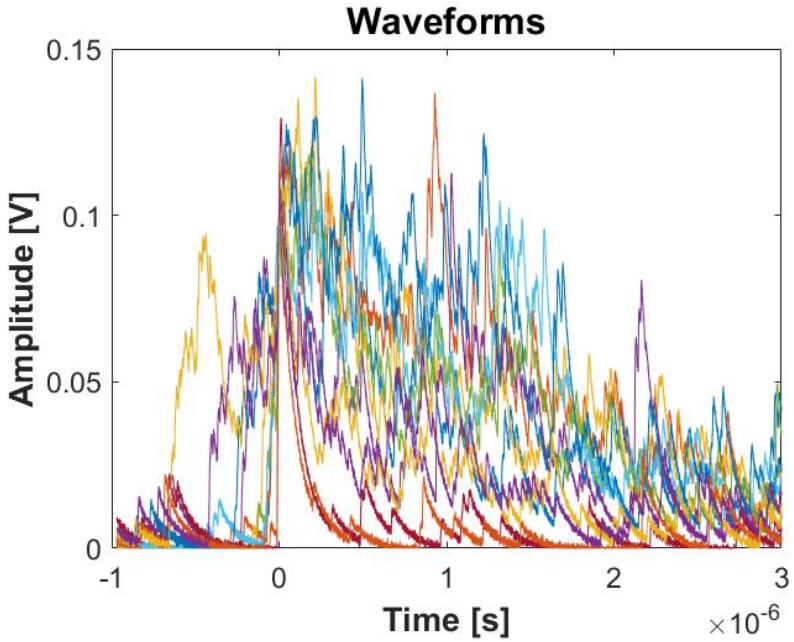

Figure 61. Raw data for spectrometer Eu:LiCAF wafer #2. This is a snapshot of the first 10 waveforms saved from the wafer during the calibration run at AFIT's DD generator.

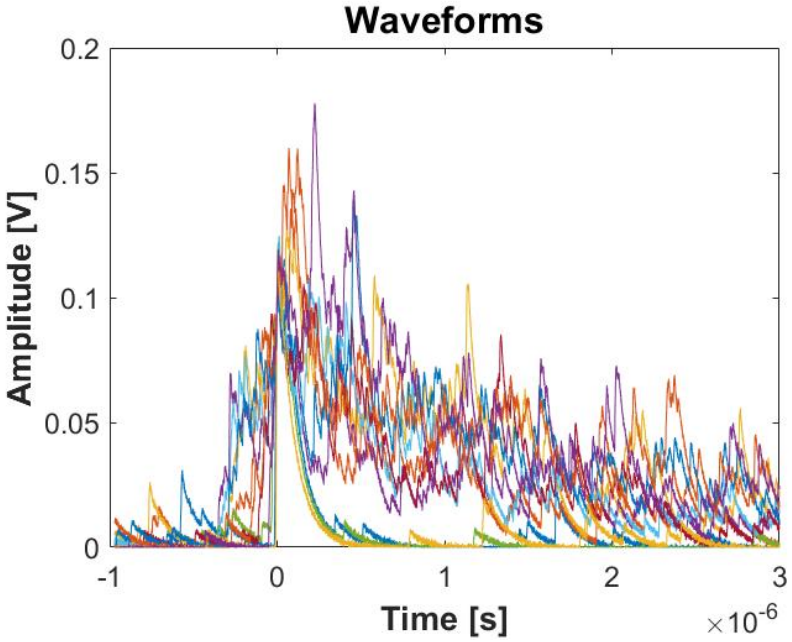

Figure 62. Raw data for spectrometer Eu:LiCAF wafer #3. This is a snapshot of the first 10 waveforms saved from the wafer during the calibration run at AFIT's DD generator.

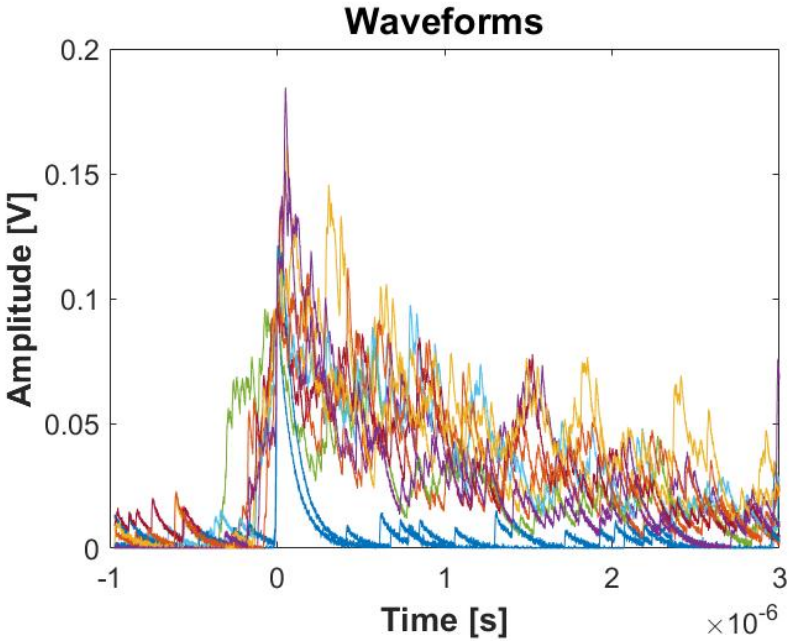

Figure 63. Raw data for spectrometer Eu:LiCAF wafer #4. This is a snapshot of the first 10 waveforms saved from the wafer during the calibration run at AFIT's DD generator.

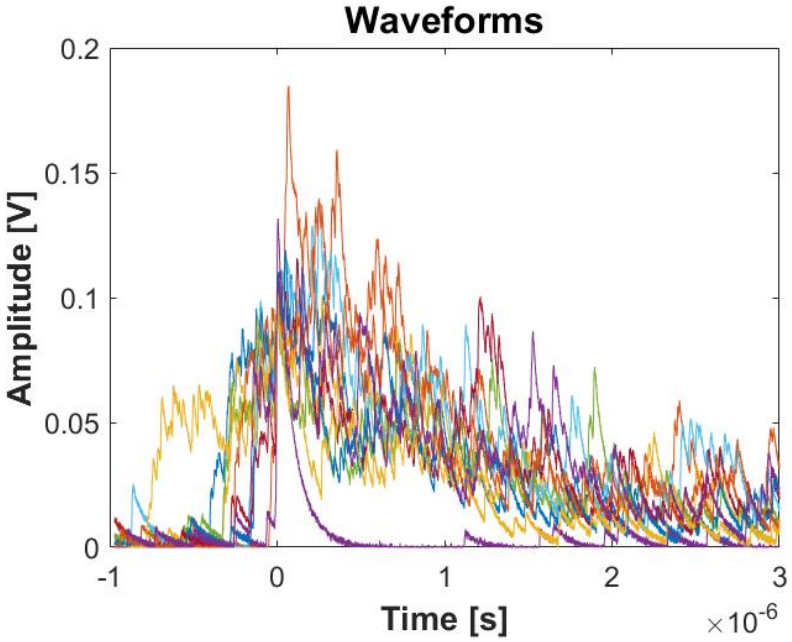

Figure 64. Raw data for spectrometer Eu:LiCAF wafer #5. This is a snapshot of the first 10 waveforms saved from the wafer during the calibration run at AFIT's DD generator.

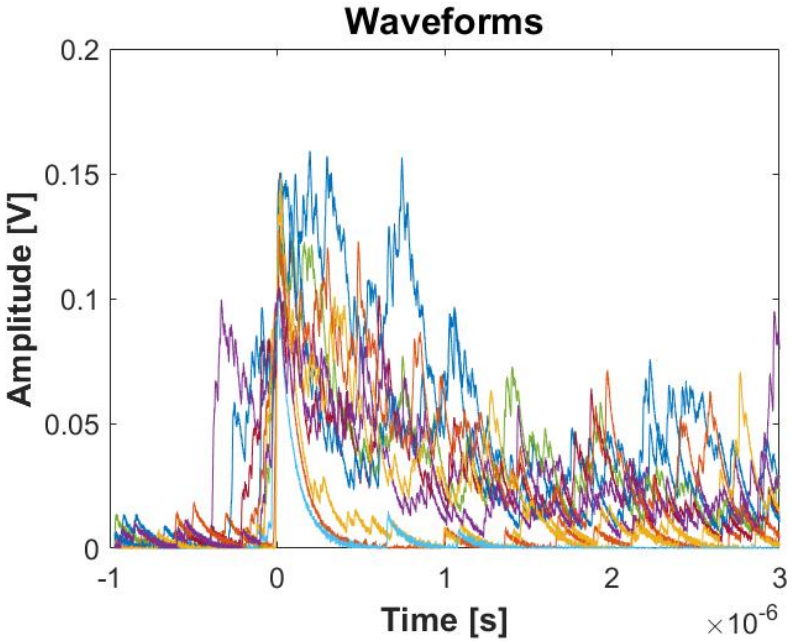

Figure 65. Raw data for spectrometer Eu:LiCAF wafer #6. This is a snapshot of the first 10 waveforms saved from the wafer during the calibration run at AFIT's DD generator.

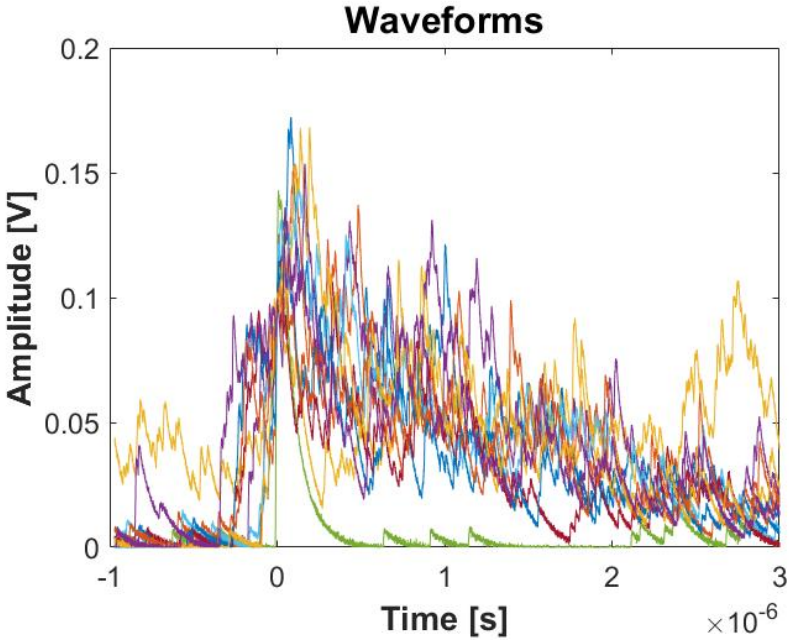

Figure 66. Raw data for spectrometer Eu:LiCAF wafer #7. This is a snapshot of the first 10 waveforms saved from the wafer during the calibration run at AFIT's DD generator.

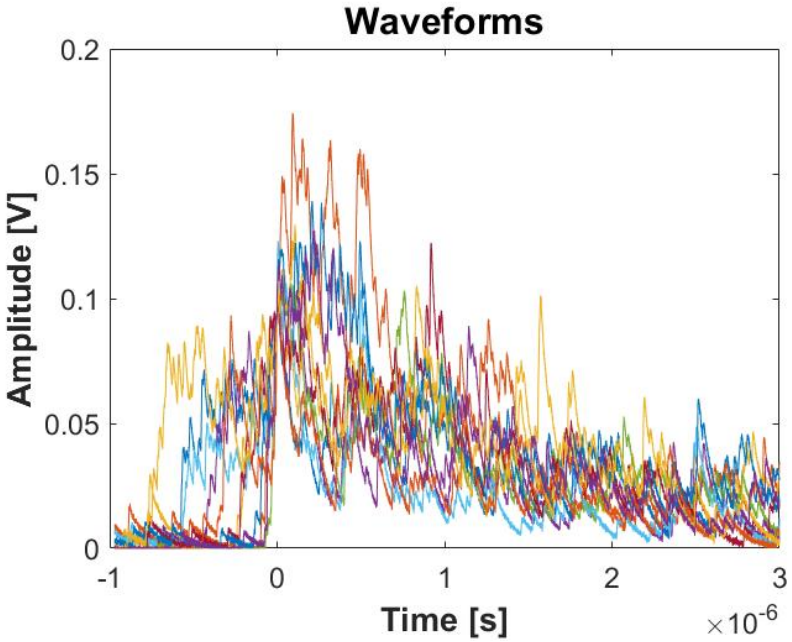

Figure 67. Raw data for spectrometer Eu:LiCAF wafer #8. This is a snapshot of the first 10 waveforms saved from the wafer during the calibration run at AFIT's DD generator.

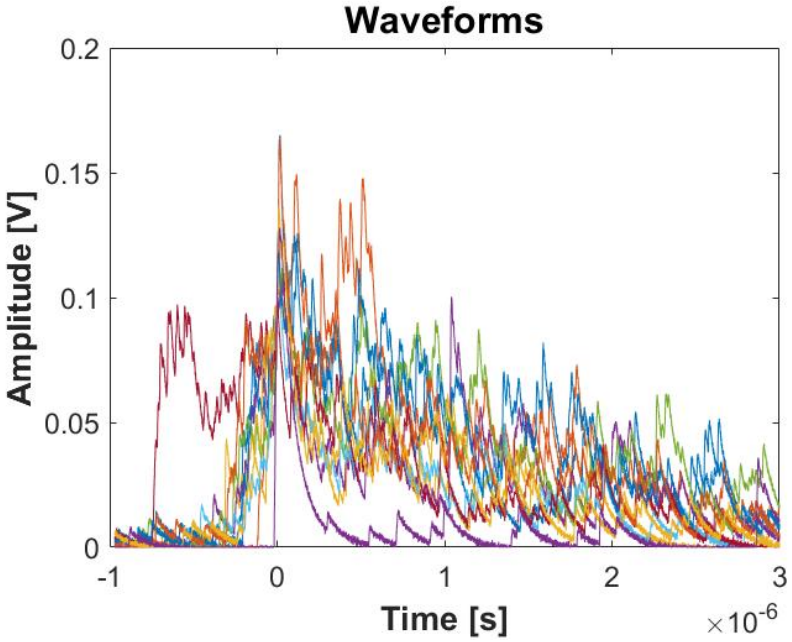

Figure 68. Raw data for spectrometer Eu:LiCAF wafer #9. This is a snapshot of the first 10 waveforms saved from the wafer during the calibration run at AFIT's DD generator.

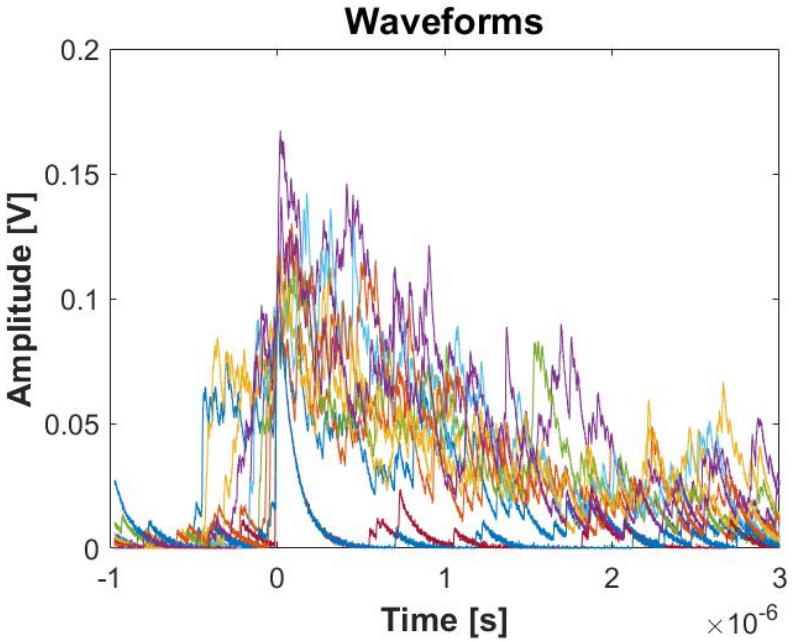

Figure 69. Raw data for spectrometer Eu:LiCAF wafer #10. This is a snapshot of the first 10 waveforms saved from the wafer during the calibration run at AFIT's DD generator.

Appendix H. Special Nuclear Material Detection

Many SNM detection challenges exist. The detection distance, or proximity of the detector to the SNM can be a challenge because of a $1/r^2$ decrease in signature as distance from the material is increased. Natural background further complicates the problem by reducing the signal-to-noise ratio. Attenuation and scattering in matter exacerbate the problem. Cosmic ray induced spallation neutron background is on the order of ≈120-150 neutrons/m^{2}s and has the ability to dominate the SNM signature [7].

Special nuclear materials of interest to the U.S. Department of Homeland Security are specific isotopes of uranium and plutonium. In particular, the interest is in materials that could be used to construct a nuclear weapon, commonly uranium- 235 (^{235}U) and plutonium-239 (^{239}Pu). ^{235}U is an isotope of uranium, making up about 0.72% of natural uranium. Unlike the predominant isotope (^{238}U), ^{235}U is fissile. ^{239}Pu is another commonly used fissile isotope, however, it is not found in nature and must be synthesized. ^{239}Pu is typically created in nuclear reactors by transmutation of individual atoms of one of the uranium isotopes. The capture of a neutron by ^{238}U creates ^{239}U, which rapidly undergoes two beta decays:

$$^{238}_{92}\mathrm{U} + ^{1}_{0}\mathrm{n} \longrightarrow ^{239}_{92}\mathrm{U} \xrightarrow[23.5min]{\beta^-} ^{239}_{93}\mathrm{Np} \xrightarrow[2.35d]{\beta^-} ^{239}_{94}\mathrm{Pu} \tag{15}$$

producing ^{239}Pu, which can then become ^{240}Pu via neutron absorption or ^{241}Pu via successive neutron absorptions. Although the SNM of interest for weapons production is ^{239}Pu, the spontaneous fission rate is often too low for this isotope to be detected from only its neutron emission. An appreciable amount of the ^{240}Pu isotope must be present in the plutonium sample for it to be detectable via spontaneous neutron emission as the neutron emission rate is ≈70,000 times larger for ^{240}Pu than it is for

^{239}Pu [7].

Detection typically boils down to targeting a unique signature of the material, acquiring particles via an interaction with the detector material, then collecting the resulting electrons (or photons) and measuring the amplitudes or timing properties of the signal to determine the type and/or amount of radiation present. With this in mind, and considering that the primary decay mode of the aforementioned isotopes is α-decay (alpha decay) [47], one would immediately consider the α-particles for the primary detection mechanism. The range of the α-particles, however, is a severe limiting factor and does not permit α-particles to be an effective SNM signature. The Bethe-Bloch equation provides a theoretical relationship between range and energy and is obtained from a quantum mechanical calculation of the collision process as a result of the Coulombic force, which has an infinite range. The calculation gives the magnitude of the energy loss per unit length, also known as the stopping power [48]. In the low-energy regime ($v^2 \ll c^2$), the stopping power is determined as:

$$\frac{d\mathrm{E}}{dx} = \frac{4\pi n z^2}{m_e v^2}\left(\frac{e^2}{4\pi\epsilon_0}\right)^2\left[\ln\left(\frac{2m_e v^2}{I}\right)\right]. \tag{16}$$

Where:

v is the velocity of the α-particle,

E is the energy of the α-particle,

x is the distance traveled,

z is the charge of the particle,

e is the electron charge,

m_e is the rest mass of the electron,

n is the electron density of the target,

I is the mean excitation potential of the target and

ϵ_0 is the vacuum permittivity.

The reciprocal of stopping power gives the distance traveled per unit of energy loss so that range can be calculated by integrating the inverse of Equation (16) over the energies of the particle:

$$R = \int_T^0 \left(-\frac{d\mathrm{E}}{dx} \right)^{-1} d\mathrm{E}. \tag{17}$$

Equation (17) can be used to determine that the 4.68 MeV α particle, resulting from the primary decay α of ^{235}U with an energy of approximately 4.68 MeV, will travel an average of only 3.18 cm in air. Using the Bragg-Kleeman rule [48]:

$$\frac{R_1}{R_0} \cong \frac{\rho_0 \sqrt{A_1}}{\rho_1 \sqrt{A_0}} \tag{18}$$

where R is the range in a specific medium, ρ the density and A the atomic weight; the range in a common material, aluminum for example (with ρ=2.70 g/cm^3 and atomic mass of 26.98 g/mol), is calculated as 9.6 μm for the 4.68 MeV α-particle. The particles can be easily stopped with common shielding materials and are hence not a good mechanism for detecting the SNM.

The next feasible option would be to consider the photons released from the SNM. There are several discrete energy γ-rays (gamma-rays) emitted from both plutonium and uranium; however, there are also prominent problems associated with their detection. According to the National Nuclear Data Center (NNDC), γ-rays in the ranges of ≈13-440 and 10-400 keV are emitted in the decay of ^{235}U and ^{239}Pu, respectively [49]. Gamma-rays interact with matter primarily through three processes: photoelectric absorption, Compton scattering and pair production. The energy ranges of the γ-rays from uranium and plutonium decays indicate that the prevalent photon interaction mechanisms are photoelectric effect and Compton scattering [48]. In the photoelectric effect, a photon is absorbed by an atom and one of the atomic electrons is released. Compton scattering is the process by which a photon scatters from

a nearly free atomic electron, resulting in a less energetic photon and a scattered electron carrying the energy lost by the photon [48]. These interactions cause an exponential decrease in the number of γ-rays that can penetrate a shielding material. A photon undergoing photoelectric absorption will disappear while the Compton scattered γ-rays will scatter until their energies are low enough to be absorbed as well. A photon mass attenuation coefficient (μ/ρ) dictates the attenuation of the γ-rays via the exponential attenuation law and is dependent upon photon energy and the density of the absorber material. The exponential attenuation law is:

$$I(x,i) = I_0 e^{-(\mu_i/\rho)\rho x} \tag{19}$$

Where I_0 is the incident number of particles in the i^{th} energy group of a narrow beam of photons penetrating a material with thickness x and density ρ. The resultant beam of photons will have I particles in the i^{th} energy group. The attenuation coefficients are well known and tabulated on the National Institute of Standards and Technology (NIST) website [50]. Considering 400 keV γ-rays and an attenuation coefficient from NIST, it can be calculated that over 99% of the γ-rays will be attenuated with less than 3 cm of aluminum shielding. The ease of shielding the γ-rays in addition to the high background levels of γ-radiation makes photons inadequate for long-range detection of SNM.

Electrons were also considered for the detection of SNM, however, problems similar to both the α-particles and γ-rays are shown to exist. Electrons interact through Coulomb scattering from atomic electrons just like alpha particles; however, there are several important distinctions. Electrons, primarily those emitted in β-decay, travel at relativistic speeds. The electrons will also suffer large deflections in collisions with other electrons causing them to follow chaotic paths [48]. A common pair of fission fragments from the fission of ^{235}U is xenon-140 and strontium-94. Xenon-140 has

a 100% β^- decay branch ratio with a Q-value of 4060 keV. Considering a highly probable β-particle of 2632 keV penetrating aluminum with a density of 2.70 g/cm^3, the average range is only 4.77 mm. While the range is significantly larger than that of alpha particles, the radiative energy loss and scattering cause them to be easily shielded.

The next, and arguably the last option for long range SNM detection, is to detect neutrons from uranium and plutonium. Referencing Table 11, it can be seen that the rate of spontaneous fission differs significantly among these isotopes. Neutrons can also be released as a result of active interrogation; where neutrons, photons, or other particles are intentionally ejected toward a target with the intention of inducing fission. Neutrons, because of their charge neutrality, do not undergo the Coulomb interaction that α-particles and electrons endure. Neutrons lose energy primarily via elastic scattering from collisions with other nuclei (not the electrons– although the interaction does occur, it is not the primary scattering mechanism). As a result, neutrons penetrate much larger distances. This penetration is valuable as it allows SNM detection at longer ranges; however, it has a side effect of creating low probability of interaction, including in the materials that detect the neutrons.

[1]Based upon average neutrons per fission of 2.44 and 2.89 for uranium and plutonium, respectively [51].

Table 11. Selected properties of common special nuclear material. Adapted from McHale [7].

Isotope	**Half Life [years]**	**Primary Decay Mode**	**Spontaneous Fission Neutron Emission Rate[1] [n/kg-sec]**
^{235}U	7.0 x 10^8	α	1.04 x 10^{-2}
^{238}U	4.5 x 10^9	α	12.6
^{239}Pu	2.4 x 10^4	α	19.9
^{240}Pu	6.5 x 10^3	α	1.38 x 10^6
^{241}Pu	14.4	α	2.20 x 10^2

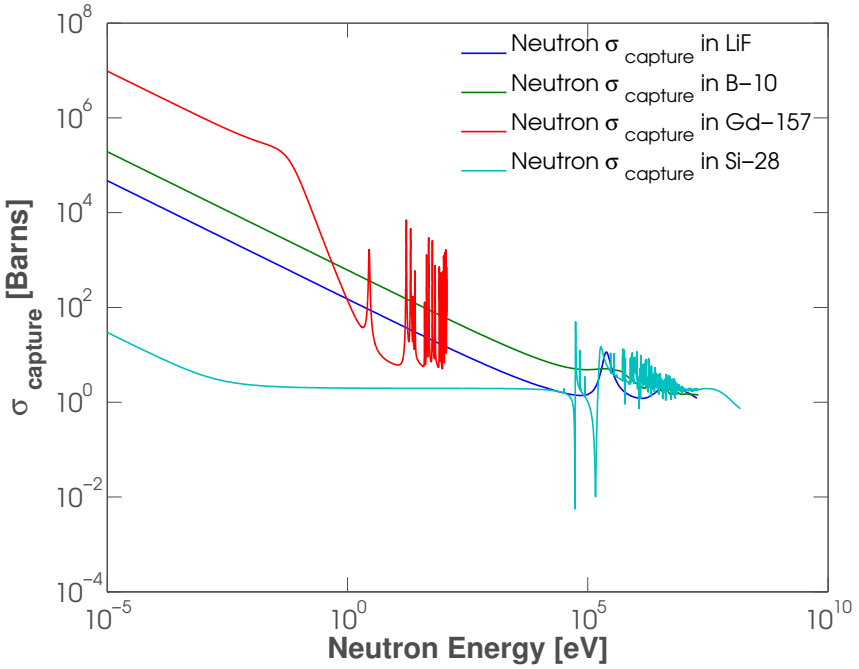

Figure 70. The energy dependent neutron capture cross sections of ^{6}Li, ^{10}B, ^{157}Gd and ^{28}Si. Compared to the thermal energy neutron absorption cross section data of silicon, the σ_{capture} are orders of magnitude higher in the lithium, boron and gadolinium.

Cross sections are important to consider whenever dealing with neutron interactions. Roughly speaking, the cross section is a measure of the relative probability for a reaction to occur. Materials with high neutron capture cross sections, and other desirable properties, can be used to detect neutrons. The most common materials in use today are particular isotopes of helium, gadolinium, boron and lithium. The energy dependent cross sections for each of these materials are shown in Fig. 70. The thermal neutron capture cross sections of lithium, boron and gadolinium are orders of magnitude higher than most other elements. For comparison purposes, the neutron capture cross sections of silicon-28 are also shown in Fig. 70. Fig. 71 additionally shows a comparison of various Tokuyama detector materials compared to ^{3}He. Each of these materials and their use for neutron detection and efficiency will be discussed later in this report.

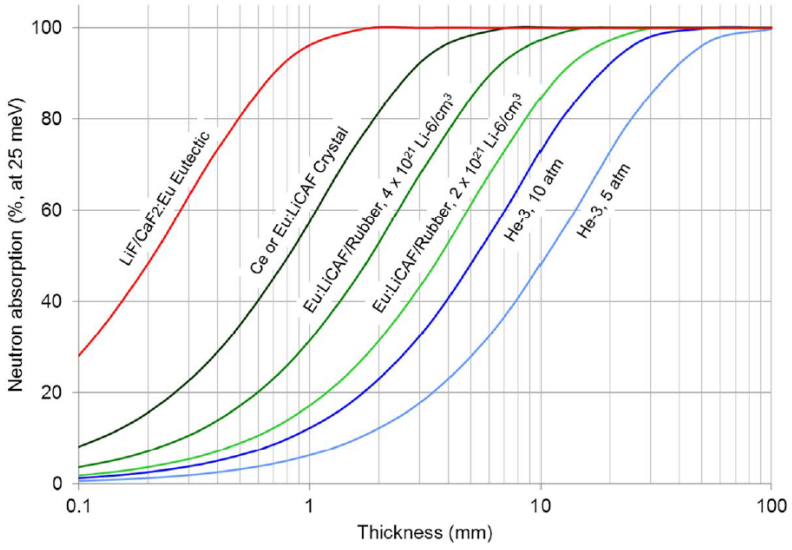

Figure 71. The detection efficiency for 25 meV neutrons for various materials [1].

In order to get a rough estimate of the number of neutrons that would hit the face of a 100 cm^2 detector (the active detection area of the Eu:LiCAF wafers) 1 meter away from 5kg of WGPu, assume the WGPu is 95% ^{239}Pu and 5% ^{240}Pu. From Table 11, the spontaneous fission rate of ^{240}Pu is 1.38 $\times 10^6$, which amounts to 345,000 neutrons/second. Now considering the spherical divergence, only 2.75 neutrons/cm^2s actually make it to the face of the spectrometer, which means that there is a total of 245 neutrons/second incident on the face of the 100cm^2 spectrometer. After accounting for all other inefficiencies (the photon detection efficiency (PDE), neutron cross section, WSF collection, etc.), the initial 245 neutrons/second can easily drop an order of magnitude and greatly increase the collection time needed to achieve good counting statistics.

Prompt fission neutrons from Uranium and Plutonium isotopes are concentrated in the energy region of ≈1.5 to 10.5 MeV [52]. Since neutron capture cross-sections are generally significantly lower for higher energy neutrons than lower energy neutrons (Fig. 70), neutrons typically scatter many times before thermalization and subse-

quent absorption. Because high energy neutrons typically scatter many times before absorption, the energy of a neutron can be determined by considering the amonut of material it penetrates before being absorbed. For example, on average, the further the neutron penetrates into a material, the higher its initial energy. This is shown in Chapter III, where the neutron spectrometer simulation results are discussed.

Appendix I. Detector Technology Overview

Over the past several decades, many researchers have examined the area of neutron detection and spectroscopy. Because neutrons produce no direct ionization events, neutron detectors must be based on detecting the secondary events produced by nuclear reactions such as (n,p), (n,α), (n,γ), (n,fission), absorption/decay, or by nuclear scattering from light charged particles, which are then detected [48]. The secondary event is necessary to create a prompt charged particle(s) (or photon) such as a proton, α-particle, etc., which can be read out via front-end electronics and processed as a signal. A variety of methods have been operative such as: gaseous detectors, scintillation detectors and semiconductor detectors. This section was written as an overview of different neutron detection techniques and can be skipped if the reader is well-read.

When determining the technology to use for a neutron detector, several factors must be considered. First, the cross section of the detection medium should be as large as possible so that efficient detectors can be built with reasonable dimensions. This is particularly important for gas detectors which typically employ large detection volumes with tubes extending upwards of 30 cm in length. For the same reason, the target nuclide should be of high isotopic abundance in the natural element, or alternatively, an economical source of artificially enriched samples should be available for detector fabrication [19]. In many applications, intense fields of γ-rays are also found with neutrons and the choice of reaction relies on the ability to discriminate against these γ-ray interactions in the detection process. Of principle importance here is the Q-value of the reaction and the α/β ratio that determines the energy liberated in the reaction following neutron capture and the number of photons created as a result of the capture interaction [19]. One typically looks for reactions with higher Q-values (MeV range) and a high α/β ratio to assist in the discrimination from γ-ray

events using only amplitude discrimination. Below is a short summary of the many methods that have been used to detect neutrons. An emphasis has been placed on slow neutrons with energies below the cadmium cutoff of ≈0.5 eV.

9.1 Gaseous Detectors

Gaseous boron trifluoride (BF_3) detectors have been widely used for detection of slow neutrons. Boron trifluoride serves as both a target for slow neutrons and also as a proportional gas in the detector. In nearly all commercial detectors, the gas is highly enriched in ^{10}B resulting in an efficiency up to five times greater than if the gas contained only naturally occurring boron [19]. The detection efficiency for a 30 cm long BF_3 tube (96% enriched in ^{10}B) filled to 80 kPa is upwards of 90% at thermal neutron energies, but drops down to 3.6% at 100 eV. A very important consideration in many applications of BF_3 tubes has been their ability to discriminate against γ-rays. Gamma-rays interacting primarily with the walls of the counter create secondary electrons that may produce ionization in the gas. Typically, this effect is easy to discriminate in low flux γ-ray environments because the stopping power for electrons in the gas is quite low, and the electrons only deposit a fraction of their energy before reaching the opposite wall. In high flux γ-ray environments, however, the problem is not so trivial; charge pile-up and even degradation of the gas has shown to exist in very high flux γ-ray environments [19].

^3He has also been used as a detection gas. ^3He has a cross section that is ≈1.39 times larger than that of boron in the thermal energy range and can be operated at much higher pressures than BF_3. ^3He is preferred over BF_3 with respect to achieving the highest detection efficiency; however, this gas is very difficult to acquire and is under very strict rationing. It is, therefore, a less viable option for the military or otherwise.

9.2 Scintillators

A disadvantage of gaseous detectors is that (typically, except for time-projection chambers, for example) the point of interaction cannot be known more precisely than 'somewhere in the tube'. In addition, typical pulse heights will have rise times that vary by as much as 3-5 μs [19]. Typical tubes are as much as 10-30 cm long in order to provide reasonable detection efficiency and therefore the path length uncertainties can be large. The limitations of gaseous detectors have been largely circumvented using scintillators. Scintillators made by fusing B_2O_3 and ZnS have found wide application in neutron time-of-flight measurements [19]. These scintillators are usually kept quite thin at 1-2 mm due to the relative opaqueness of this material to its own scintillation light and also to minimize path length uncertainty. A large problem is that these scintillators are much less effective in γ-ray background discrimination compared with BF_3 tubes. Photon production as a result of secondary electrons from γ-ray interactions is difficult to discriminate from the photon production as a result of the neutron interactions. Amplitude discrimination is no longer sufficient and pulse-shape discrimination must be employed [53].

While a lithium equivalent of the BF_3 tube is not available because a stable lithium-containing proportional gas does not exist, lithium has been very successful as a scintillating material. A common application has been in the form of crystalline lithium iodide because of its chemical similarity to sodium iodide [19]. While highly hygroscopic, a solution has been to keep it contained in hermetically sealed cans with a thin optical window. The high density of the material means that crystal sizes need not be very large for very efficient slow neutron detection. In fact, a 1 cm thick crystal prepared from highly enriched ^{6}LiI is nearly 100% efficient in capturing slow neutrons below the Cd cutoff [19].

Scintillation materials for neutron detection have been somewhat of a highlight for

the past two decades. Substantial research has been done with each of the materials previously highlighted (Li, B and Gd) [54, 53, 55, 56]. Recent studies with gadolinium aimed at loading plastic with Gd containing additives have been successful, despite the discrimination sensitivities [56]. The aim was in developing inexpensive and efficient thermal neutron detectors with low γ-ray sensitivity that can be produced in large (or complex) arrays. The study concluded with a metallo-organic compound gadolinium isopropoxide used as an additive to synthesize polystyrene-based plastic scintillators with a relative light output of 76% transmissivity with only 3% Gd (by weight). A 13 mm thick scintillator loaded with 0.5% Gd detects approximately 46% of thermal neutrons that enter the detector volume [56].

9.3 Neutron-Induced Fission Detectors

The fission cross sections of ^{233}U, ^{235}U and ^{239}Pu are relatively large at low neutron energies and thus these materials can be used as the basis of slow neutron detectors [19]. One characteristic that stands out with fission detectors is the uniquely high Q-value of $\approx$ 200 MeV, relieving many of the discrimination issues prevalent with other neutron detectors. Neutron-induced fission detectors are often ionization chambers with their inner surfaces coated with a fissile deposit, and the dimensions of the counters tend to be similar to those of α-particle detectors (the average range of the fission fragments are approximately half the range of a 5 MeV α-particle). The two fission fragments are always oppositely directed for slow-neutron-induced fission, and therefore detectors with a solid coating of fissionable material will respond only to the single fragment that is directed toward the active volume of the chamber [19]. Some fission counters have been built with extremely thin backing material underneath a thin fissile deposit so that both of the fission fragments can be detected, however, the very thin supports required for the fissile deposits are quite fragile and consequently,

this type of fission chamber is not widely used in routine neutron detection applications [19]. Problems have also been discovered with charge pile-up as a result of the primary α-decay with the fissionable materials used in the detectors.

9.4 Activation Detectors

The concept behind activation neutron detection is the use of induced activity in one of more specially chosen materials to infer the neutron flux and energy spectrum at a particular location. Activation detection has the advantages of low cost, superior physical form and ease of calibration. It is possible to find materials with linear response even to very high rates of fission reactions. This method has the primary disadvantage of being both passive and inactive; the foils must be manually checked and measured, creating a logistical nightmare in a fast-paced and incessant atmosphere of some shipping ports where their use is highly applicable.

9.5 Proton Recoil Instruments

The proton recoil method works by measuring the energy and direction of protons that have been recoiled by a neutron (generally higher energy neutrons). The material in which the recoiling takes place is typically a thin layer of hydrogenous substance. The relative accuracy with which the recoiled proton properties can be measured allows an acquisition of high resolution neutron spectra over a wide energy range. Resolutions of 1-3% are typical for 14.1 MeV neutrons [19]. Also, energies from below 1 MeV up to more than 1 GeV have been measured. The short range of the recoiled protons and the need for higher resolutions limit the possible recoil material thickness and thus reduce the detection efficiency.

9.6 Thin-Film Semiconductor Detectors

Semiconductor detectors, in their most basic application consist of a planar diode supplemented with a neutron conversion layer that has been deposited on its surface. Neutrons are captured in the converter and secondary particles are produced. The secondary charged particles create electron-hole pairs in the diode that are swept to the surface of the diode and collected as a current. A limitation to the semiconductor detector is that the efficiency depends on the thickness of the conversion layer, however, if made too thick, the conversion layer may not allow the changed particles to escape into the semiconductor to create the electron-hole pairs [57, 19]. Figure 72 shows the basic geometry of a thin-film semiconductor detector with annotation of a neutron interaction in the thin-film.

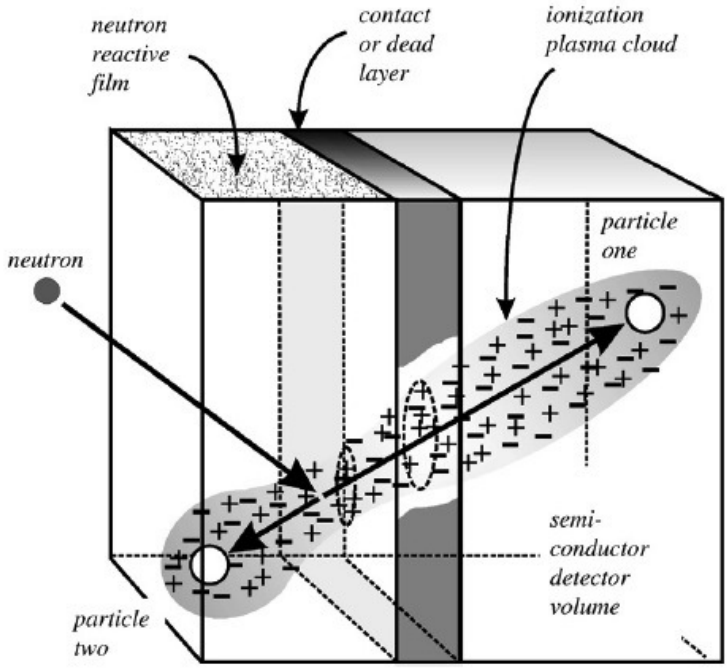

Figure 72. The fundamental approach to a thin-film coated semiconductor neutron detector. The film thickness should not exceed the maximum range of the 'long-range' reaction product. The reaction products are emitted in opposite directions [58]. ©2003 with permission from Elsevier.

Significant research has been conducted to improve the geometry of the semiconductor thin-film detector in order to improve the neutron detection efficiency. Several aspects of the semiconductor detector make it desirable, hence motivating the broad range of research being conducted. They can be built very inexpensively and be mass produced, have very low power requirements, can be built to virtually any size and are extremely rugged.

The basic configuration consists of a common Schottky barrier or p-n junction diode, upon which any of the aforementioned neutron reactive coatings is applied [57]. The current restriction to the wide-spread use of these devices is the sub-par efficiency compared to the many alternatives listed above such as scintillation detectors and gas tubes. Material choice requires a strong neutron absorbing reactive coating that emits ionizing reaction products, preferably charged particles rather than photons [57]. Some attractive materials that have been examined for solid state neutron detection include gadolinium, boron and lithium. The thermal neutron (v=2200 m/s) capture cross section for ^{157}Gd is 240,000 barns, for ^{10}B the cross section is 3840 barns and for ^{6}Li, the thermal neutron absorption cross section is 940 barns.

9.7 Common Neutron Detection Materials

Several materials have been explored as thin-film neutron conversion layer materials. The thermal neutron capture cross section for ^{157}Gd is 240,000 barns. This allows for efficient absorption of thermal neutrons in a thin-film of material. Unfortunately, gadolinium has the side effect of producing low energy internal conversion electrons, as well as a cascade of associated Auger electrons, x-rays and γ-rays ranging in energy from a few eV to several MeV making it almost impossible to discern a neutron event from background [19].

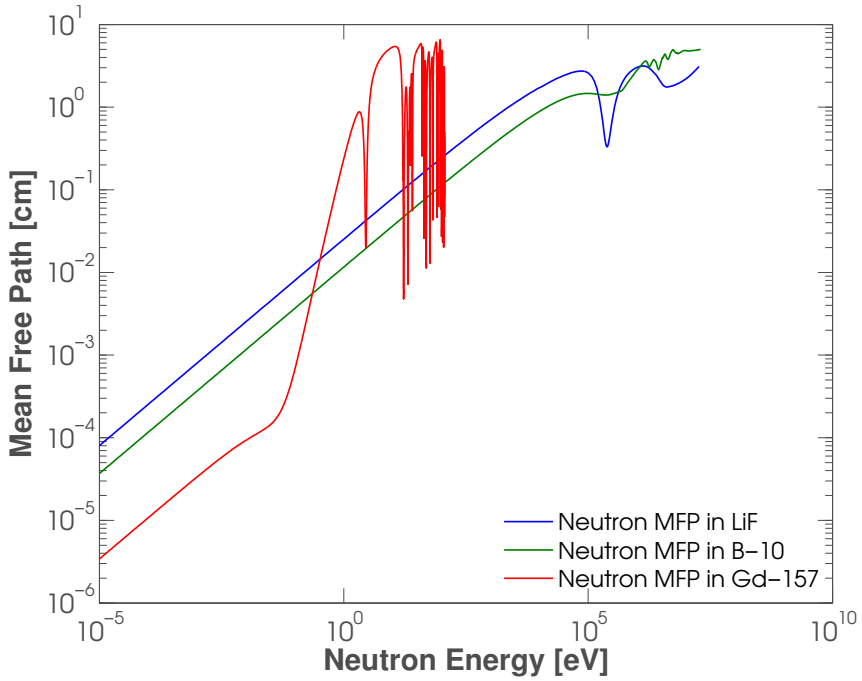

Figure 73. The mean free path (mfp) of neutrons in ^{157}Gd, ^{10}B and ^{6}Li. As the neutron's energy is increased, the mean free path is larger. At high energies, it becomes increasingly probable that the neutron will pass directly through the material and not be detected.

Boron, as a more practical substitution for gadolinium has also been applied to semiconductor detectors; the thermal neutron absorption cross section is not as high, but still respectable at 3840 barns. Boron has been used for decades with great success; however, the charged particles emitted from the ${}^{1}_{0}\mathrm{n}+{}^{10}_{5}\mathrm{B}$ reaction are lower energy than those emitted from the ${}^{1}_{0}\mathrm{n}+{}^{6}_{3}\mathrm{Li}$ reaction (and there are two reaction paths in boron, whereas there is only a single reaction in lithium).

The energy dependent mean free path in each material is shown in Fig. 73. The mean-free-path (mfp) has many qualitative applications in detectors, for example, if the mfp of the neutrons is long compared to the dimensions of the sample, it is likely that most will escape from the sample. This is an important concept in a spectrometer in relation to the thermalization of neutrons and will be discussed later in more detail. Notice that the mfp is lowest in gadolinium, as expected, due to

the significantly larger cross sections. This document will focus on the use of a ^{6}Li containing neutron conversion material, which has a cross section of 940 barns and just one neutron reaction branch. A brief description of the three most common reaction materials follows.

Gadolinium.

Gadolinium is a naturally occurring element which has two isotopes with very high thermal neutron cross-sections: ^{155}Gd (14.7% natural abundance) and ^{157}Gd (15.7% natural abundance) with 6.1x10^{4} barns and 2.6x10^{5} barns, respectively [57]. These cross sections are higher than every other isotope, which makes gadolinium an attractive material for a variety of neutron detectors. In a solid state neutron detector, one large disadvantage of gadolinium is that the absorption of a thermal neutron results in the emission of low energy internal conversion electrons, Auger electrons and an array of gamma and x-rays. Unfortunately, a majority of the products are on the low-energy end of the spectrum (below 70 keV) or high energy γ-rays, which can be easily confused with background γ-rays or escape the detector without producing secondary particles.

Boron.

The ^{10}B(n,α)^{7}Li neutron reaction yields two possible decay branches from the excited ^{11}B compound nucleus:

$$ {}^{1}_{0}\mathrm{n} + {}^{10}_{5}B \longrightarrow \begin{cases} {}^{7}_{3}\mathrm{Li}^{*}(1.4721\mathrm{MeV}) + {}^{4}_{2}\mathrm{He}(0.8398\mathrm{MeV}) & (93.7\%) \\ {}^{7}_{3}\mathrm{Li}(1.7762\mathrm{MeV}) + {}^{4}_{2}\mathrm{He}(1.0133\mathrm{MeV}) & (6.3\%) \end{cases} $$

where the Li ion in the 94% branch is ejected in an excited state and normally de-excites through the emission of a 480 keV γ-ray [19]. In either case, the Q-value of the

reaction for thermal neutron interactions is very large (2.310 or 2.792 MeV) compared with the incoming energy of the neutron. Thus, the incoming kinetic energy of the neutron is convoluted in the much larger reaction energy and it is impossible to extract any information about the initial neutron energy [19]. Also, because the incoming linear momentum is very small, the reaction products must have a net momentum of near zero. As a consequence of this, the reaction products are ejected in opposite directions with the energy of the reaction shared between them. This is demonstrated via the following equations (for the 93.7% reaction):

$$E_{\mathrm{Li}} + E_{\alpha} = Q = 2.31\mathrm{MeV} \tag{20}$$

and

$$m_{\mathrm{Li}}\nu_{\mathrm{Li}} = m_{\alpha}\nu_{\alpha}. \tag{21}$$

Using the basic equation for energy ($E = \frac{1}{2}mv^2$), this can be converted to:

$$\sqrt{2m_{\mathrm{Li}}E_{\mathrm{Li}}} = \sqrt{2m_{\alpha}E_{\alpha}}. \tag{22}$$

Solving Equations (20) and (22) simultaneously, using masses for the Li=6535.13 MeV/c^2 and α=3727.38 MeV/c^2 yields:

$$\mathrm{E_{Li}}=0.84 \text{ MeV and } \mathrm{E_{\alpha}}=1.47 \text{ MeV}.$$

^{10}B has a microscopic absorption cross section for thermal neutrons of 3840 barns (substantially less than that of Gd). With a mass density of 2.15 g cm^{-3}, the solid structure of ^{10}B has a macroscopic thermal cross section of 500 cm^{-1} and the cross section follows a $1/v$ dependence [19].

Lithium-6.

The ^{6}Li(n,t)^{4}He neutron reaction yields a single product branch emitting high energy charged particles:

$$ {}^{1}_{0}\mathrm{n} + {}^{6}_{3}\mathrm{Li} \longrightarrow {}^{3}_{1}\mathrm{H}\ (2.7276\mathrm{MeV}) + {}^{4}_{2}\mathrm{He}\ (2.0553\mathrm{MeV}). \tag{23} $$

Similar to the boron products, the triton and α-particles are ejected in exactly opposite directions. The higher energy reaction products make them easier to discriminate from background γ-rays. ^{6}Li has a relatively large thermal neutron absorption cross section of 940 barns and also follows a $1/v$ dependence [19]. A disadvantage of working with lithium is that it is highly reactive and difficult to prevent from decomposing, even when using encapsulates. It is the stable compound LiF that is often used, although other lithium-containing compounds are also being explored (such as Eu:LiCAF for this research, CLYC, and CLLC).

Appendix J. Geant4 Overview

Geant4, short for particle **GE**neration **AN**d **T**racking, was originally developed to meet an ever increasing demand for accurate and comprehensive physics simulations. The Geant4 simulation toolkit provides comprehensive detector and physics modeling capabilities embedded in a flexible C++ structure [23]. It serves primarily to simulate the passage of particles through matter and is used by a large number of experiments and projects in a variety of application domains including: high energy physics, astrophysics and space science, medical physics and radiation protection.

Geant4 was chosen as the simulation package for this research because of its flexibility and robustness. Its kernel encompasses tracking, geometry description and navigation, material specification, abstract interfaces to physics processes, management of events, run configuration, stacking for track prioritization, tools for handling the detector response and interfaces to external frameworks, graphics and user interface systems [24]. Fig. 74 is a flow chart representing the hierarchical structure of Geant4. A few of the more-important processes are described below.

The first necessary step is to define the materials and geometry of the experimental

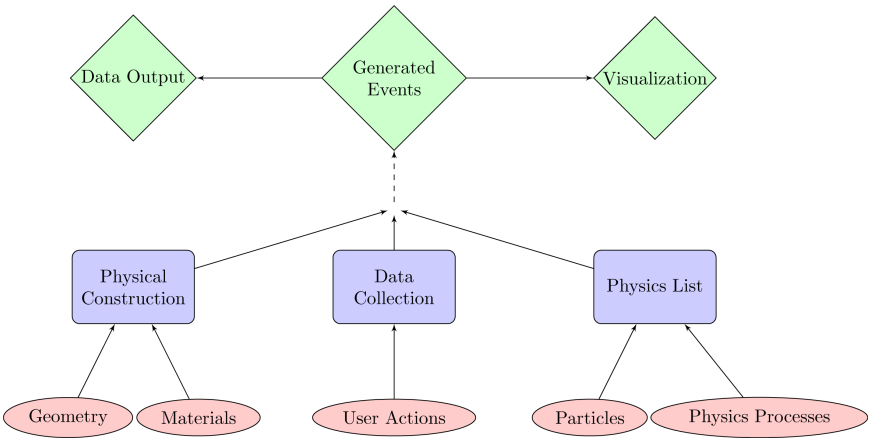

Figure 74. Flow chart representation of a Geant4 simulation. The lowest level represents the basic simulation building blocks, the second level consists of the user defined parameters, and the topmost level represents simulation execution and output [59].

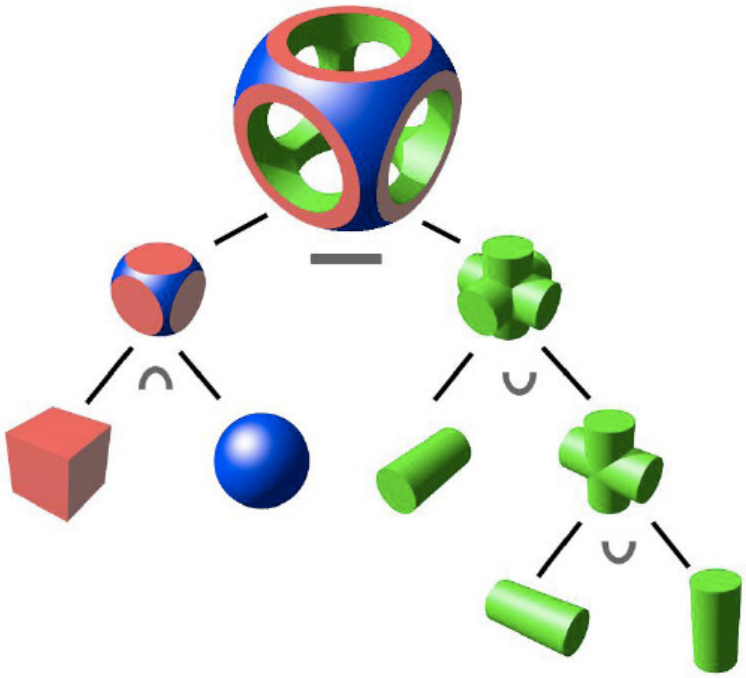

Figure 75. Boolean operations on constructive solid geometries (CSGs). The volumes on the left are combined via intersections, those on the right via union, and the final solid is a difference of the left and right [59].

setup. Constructive Solid Geometry (CSG) was used to define the apparatus, wherein volumes are described by a collection of simple three-dimensional volumes such as spheres, cubes, cones, etc. Using CSG, volumes have a much smaller memory footprint than if they were represented using Boundary Represented Solids (BREPS). BREPS and CSG are the two basic methods of describing geometries in Geant4 [60]. A representation of complex geometries that can be created using CSG is shown in Fig. 75.

Fig. 76 represents C++ script for defining a material in Geant4, which is one of the simplest things to do in Geant4. The last four lines of the script show Eu:LiCAF consisting of one atom of enriched lithium, six atoms of fluorine, one atom of calcium

```
G4double LiCAFdensity = 2.99*g/cm3;
G4Material* LiCAF = new G4Material(name="LiCAF", LiCAFdensity, ncomponents=4);
LiCAF->AddElement(ELithium, natoms=1);
LiCAF->AddElement(F, natoms=6);
LiCAF->AddElement(Ca, natoms=1);
LiCAF->AddElement(Al, natoms=1);
```

Figure 76. Example script from the 'DetectorConstruction.cc' file in Geant4. This selection of script defines the enriched LiCAF material for the simulation of the spectrometer.

and one atom of aluminum. The enriched lithium (ELithium) is composed of 95% ^{6}Li and 5% ^{7}Li. One thing to note is that the europium dopant was not added to the simulations. This is something that would be desirable in future work to increase the fidelity of the simulations. The simulation is customizable and material definitions are often necessary in order to get more accurate results that closely resemble actual testing conditions. The materials defined herein include: air, paraffin wax, cadmium, silicon, aluminum, borated polyethylene and enriched Eu:LiCAF. After assembling the simulation, the next step is specifying the necessary particles and physics processes. In contrast to MCNP, where most of the transport physics and secondary particle generation is automatic, Geant4 requires the user to explicitly define all particles and processes necessary for a particular setup; with 19 different physics models, spanning an energy range of meV up to the TeV region, not all particles and processes are valid for a given application [60]. When carefully implemented, the ability to select specific processes can substantially reduce the simulation time.

The execution of Geant4 can be broken down into four components [59].

- A *step*, which is the path of a particle between interaction and/or geometric boundaries.
- A *track* representing the sum of all steps for a particle.
- An *event* which tracks the history of a single original incident particle. This includes the tracks of any and all secondary particles.

- A *run* consisting of all events in the simulation.

Once all parameters of a simulation have been defined, Geant4 will construct the geometry and begin to simulate particle interactions as specified by the user. The particles will interact in a manner consistent with the physics defined by the user, with Geant4 calculating the steps as the particle traverses through the user defined geometries. A step is the shortest distance through the simulation that a particle travels, its length being the distance from one interaction to another. Each successive step is calculated by the particle's trajectory, with the energy, change in trajectory and other changes used to update the particle's state in order to calculate a new step. The process is iterated until zero kinetic energy remains, the particle is absorbed, or it escapes the simulation boundary [59]. It is important to consider, however, that there is not only one possible trajectory of a particle. Each successive step is determined using a Monte Carlo random sampling method. For each particle interaction, the mean free path is found from the individual cross sections and the material number density for the volume being traversed [59]:

$$\lambda_i = \frac{1}{\sigma_i N}, \tag{24}$$

where λ is the mean free path and i indicates the particular reaction. The mean free path is the average distance a particle will travel before interacting, but, there is a probability that the particle will traverse a much shorter or larger distance than the average. The true interaction distance l_i is sampled for each reaction using [60]:

$$n = 1 - e^{-\lambda_i l_i} \Rightarrow l_i = -\frac{\ln(1-n)}{\lambda_i}, \tag{25}$$

where n is a random number uniformly distributed in the range (0,1). This is done for each physics process assigned by the user; the interaction distances are then

compared, with the shortest one chosen as the step length. If the distance to the volume boundary is less than the calculated step length, the step length is reduced to the boundary distance, where a new step is calculated [60]. Each step for a particular particle in a volume can then be stored in a track, where the particle's properties can be recalled. This gives the ability to sum all energy deposited in a volume, either directly or by secondary particles of an incident particle.

The energy deposited by each original incident particle is then binned at the run level using the Abstract Interface for Data Analysis (AIDA) [61]. AIDA was initiated at the HepVis 1999 workshop in Orsay and has since evolved into a robust histogramming utility allowing output of the data in several formats, most notably in the extensible markup language (XML) that can be read by many cross-platform applications such as MATLAB®. The user must instantiate the AIDA interface, specify the number of histograms required and the parameters of the histogram(s) [59]. Data is collected using the AIDA utility, allowing easy readout by the end-user. The next section discusses the simulation results obtained using Geant4.

Appendix K. MAXED Code and Input Files

The MAXED code used here is different than the original MAXED in the following ways:

1. It can be run interactively or using a control file.

2. The main algorithm has been modified slightly. A new constraint:

$$\sum_k \frac{N_k}{\sigma_k} - \sum_{k,i} \frac{R_{ki} f_i}{\sigma_k} = 0 \tag{26}$$

   has been added. N_k is the measured counts per wafer k, σ_k is the estimate of the measurement error for wafer k, f_i is the output energy spectrum of MAXED, and R_{ki} is the response matrix. This constraint has been added to the set of conditions under which the relative entropy is maximized.

3. The algorithm used for searching for the maximum entropy has been modified slightly, and now the temperature parameter used by the simulated annealing algorithm can be set in almost all cases to 1.0 (as it was here).

4. The format of the input and output files has been modified to allow the user to run the program as part of the HEPRO package.

5. It generates an additional output file, with extension ".par", which can be used by the program IQU_FC33. IQU_FC33 is a program written to calculate integral quantities for MXD_FC33 solution spectra.

6. A new parameter for χ^2/D.O.F. allows the user to pre-define the final chi-squared per degree of freedom.

7. The user can choose whether any re-binning of spectra and/or response functions is linear with respect to energy or linear with respect to log(energy).

The code was initially written for 'unfolding' the spectrum from a multi-sphere neutron spectrometer though it is also applicable to this layered spectrometer because of the essentially identical operation of the two devices. The following section will describe the input files to run the MAXED program.

MAXED was written in Fortran 90 and compiled with the Compaq Visual Fortran compiler. The program UMGPlot, which is used to visualize the results of MAXED, was written using the programming environment ComponentOne Studio for ActiveX. MAXED has the option to run using a control file or alternatively can be run interactively. The unfolding accomplished for this report was done using a control file. The control file is 10 lines in length and specifies each of the parameters needed to successfully run MAXED; these designators are specified in Table 12 for the testing run at the Air Force Institute of Technology, and in Table 13 for the testing run at the Univerity of Michigan.

The temperature and temperature reduction factor parameters in item 07 (Table 12 and 13) are parameters used by the simulated annealing optimization subroutine. The temperature parameter can be set to 1.0 in almost all cases. The value of 0.85 is recommended for the simulated annealing temperature reduction factor parameter,

Table 12. Control file line designators (AFIT testing).

Line Number	Description	Value Used
1	Name of file with input data	dat_spec_L.ibu
2	Name of file with response functions	resp_fun_L.fmt
3	Name of output file	mxfc_005
4	Name of file with default spectrum	def_spec_L.flu
5	Highest energy of the solution spectrum	10
6	Requested final chi^2 per DOF (max.)	1.0
7	Temperature and temperature reduction factor parameters	1.0,0.85
8	Energy bin structure for unfolding, Solution spectrum bins	3,2
9	Choice of scaling the default spectrum	1
10	Choice of changing the MXD_FC33 scale factor	0

Table 13. Control file line designators (Michigan testing).

Line Number	Description	Value Used
1	Name of file with input data	dat_spec_L2.ibu
2	Name of file with response functions	resp_fun_L2.fmt
3	Name of output file	mxfc_006
4	Name of file with default spectrum	def_spec_L.flu
5	Highest energy of the solution spectrum	10
6	Requested final chi^2 per DOF (max.)	1.0
7	Temperature and temperature reduction factor parameters	1.0,0.85
8	Energy bin structure for unfolding, Solution spectrum bins	3,2
9	Choice of scaling the default spectrum	1
10	Choice of changing the MXD_FC33 scale factor	0

however a range of values will be considered here [40]. In item 08, there are several options for the energy bin structure; these options are outlined in Table 14. For record 9, the options are specified by the binary 0 or 1; '0' meaning to not apply a scale factor and '1' meaning to scale the default spectrum. Line 10 is designated equivalently to line 09 (binary).

Table 14. Available options for line 08 of the control file.

Option	Description
0	Use a fine energy bin structure
1	Four bins per decade
2	Energy bin structure of the default spectrum
3	Energy bin structure of the response functions

The control file is just the first of four necessary files to run the algorithm. A file with the spectrometer's data is supplied by the user and requires fields for the number of measurements and a description of each measurement. The file with the measured data is outlined in Table 15. Line number 03 (a-g) is repeated for each measurement (the number of measurements specified in line 2).

The '2x' in line 02 of Table 15 simply identifies two spaces. The next logical step would be to define the response functions. The method for inputting the response

Table 15. Measured data file line designators.

Line Number	Description	Value Used
1	Header (80 characters)	Spectrometer Data
2	Number of measurements and correction factor	10 2x 0
3a	8 Character ID	0W0
3b	Moderator thickness (cm)	1.25
3c	Measured data	2.878E+04
3d	Uncertainty due to statistics (absolute units)	1.696E+02
3e	Uncertainty due to statistics (percentage)	0.59
3f	Other uncertainties (percentage)	2.0
3g	A "flag" to describe the data	0

Table 16. Response functions file line designators.

Line Number	Description	Value Used
1	Header (80 characters)	Response Functions
2	Header (80 characters)	Response Functions
3	Energy bin edges in response function, units of E	23 2x 1
4	The energy bin edges in the response function	1.000E-08 2x 1.000E-07 ...
5	Dummy variable (DV)	0
6	Number of response functions	10
7a	Response function ID, comments	0W0
7b	DV, units of response function, 7 DVs	1.000E+00, 0,...,0
7c	The responses for the layer	4.784E+05 2x 3.047E+05 ...

functions is very similar to that of the measured data. The format for the file is specified in Table 16. Line 03 requires the specification of energy units (this is the first time units has come into the algorithm). Table 17 outlines the values to specify certain units of energy. A '1' was used throughout the unfolding algorithm to specify that each spectrometer measurement was defined in terms of MeV. The purpose of this file is to input the response functions for use in the unfolding procedure. Records 7a,b and c will be repeated for all response functions in this file (the number specified in line 06).

Table 17. Available options for specifying units of energy.

Option	Description
0	eV
1	MeV
2	keV

The final file describes the default spectrum. The default spectrum supplies the a priori information which is crucial for the 'few channel' case, where the number of detectors is much smaller than the number of energy bins used for the unfolding. The approach used in MAXED can be justified on the basis of arguments that originate in information theory and allows for the inclusion of a priori information in a well-defined and mathematically consistent way [46]. In addition to having a sound theoretical basis, this approach has other features that have proven to be useful from a more practical point of view: it makes use of the estimated variance for each detector's count rate in the unfolding process, appropriately weighting the data from each detector. The algorithm leads to a solution spectrum that is always a non-negative function and can be written in closed form [46]. The default spectrum file layout is outlined in Table 18.

Table 18. Default spectrum functions file line designators.

Line Number	Description	Value Used
1	Header (80 characters)	Default Function
2	Form of default spectrum, Units of energy	2,1
3	DV, number of bins, max energy	2 2x 47 2x 10.00E+00
4	Energy bin edge, bin magnitude	1.000E-08 2x 0.0E+00 ...

The 'form of the default spectrum' as specified in line 02 of the default spectrum file can be defined by several values as outlined in Table 19. The default spectrum defined for this unfolding was defined as *fluence rate per bin* since it was concentrated around the thermal and 2.45 MeV energy regions. Record 04 is repeated for each bin edge and bin. The input decks for unfolding the spectrometer data from AFIT and the University of Michigan are shown in Appendices E and F, respectively.

Table 19. Available options for specifying the 'form of the default spectrum'.

Option	Description
1	$d\phi/dE$
2	Fluence rate per bin
3	$(E\ d\phi)/dE$

11.1 The Algorithm

The MAXED algorithm used in MXD_FC33 is a maximum entropy algorithm which can be described in terms of a set of input parameters, a set of output parameters and the equations relating these quantities [62]. In practice, the algorithm is formulated in discrete terms with n energy bins that are labeled with index i. Assuming m detectors that we label with index k, a set of admissible spectra are defined using two restrictions:

$$N_k + \epsilon_k = \sum_i R_{ki} f_i \tag{27}$$

and

$$\sum_k \frac{\epsilon_k^2}{\sigma_k^2} = \Omega, \tag{28}$$

where:

N_k is the measurement,

ϵ_k is the difference between the measured and predicted value for detector k,

R_{ki} is the response function for detector k,

f_i is the solution spectrum,

σ_k is the estimated standard uncertainty and

Ω is a parameter set by the user to obtain a specific Chi-squared value.

Equation (27) is an integral equation that relates the measurement to the detector's response function and the neutron spectrum, allowing for a measurement error. Equation (28) is a constraint for handling the ϵ_k and assumes that the Chi-squared statistic of the solution is equal to a value determined a priori by the user. From the array of admissible spectra, the ideal response is one that maximizes the entropy S of the distribution:

$$S = -\sum_i \left[f_i ln \left(\frac{f_i}{f_i^{DEF}} \right) + f_i^{DEF} - f_i \right], \tag{29}$$

where f_i^{DEF} is the default spectrum that contains the a priori information. The maximization of S with constraints given by Equations (27) and (28) is equivalent to maximization of a potential function $Z(\lambda_k)$ with respect to a set of m parameters λ_k [46]. The solution spectrum f_i and the solution for ϵ_k can be written in terms of λ_k:

$$f_i = f_i^{DEF} exp\left[-\sum_k \lambda_k R_{ki}\right] \tag{30}$$

and

$$\epsilon_k = \frac{\lambda_k \sigma_k^2}{2}\left(\frac{4\Omega}{\sum_j (\lambda_j \sigma_j)^2}\right)^{1/2}. \tag{31}$$

To find the values of λ_k that maximize Z, the simulated annealing algorithm for the few-channel case is applicable here. The algorithm requires the input of N_k, σ_k, f_i^{DEF}, R_{ki} and Ω and calculates output parameters λ_k. Since the maximum entropy solution can be written in closed form, one can use Equations (27-30) to calculate the effect of small changes in the input parameters [62]. Any change in the input parameters will lead to a change in the output parameters λ_k, which in turn will lead to a change in the f_i and the ϵ_k calculated from Equations (29) and (30).

The approach used in MAXED can be justified on the basis of arguments that originate in information theory [41]. The approach allows for the inclusion of a priori information in a well-defined and mathematically consistent way which is crucial for this case where the number of detectors is much smaller than the number of energy bins used for the unfolding. The a priori information becomes an important factor. MAXED also makes use of the estimated variance for each detector's count rate in the unfolding process, appropriately weighting the data from each detector; the algorithm leads to a solution spectrum that is always a non-negative function and the solution can be written in closed form (a mathematical expression that can be evaluated in a finite number of operations) [41].

Appendix L. MATLAB Filter Analysis

Both FIR and IIR filters were modeled using MATLAB in order to determine the proper filter. The MATLAB code used is shown in Appendix D. The finite impulse response filter (FIR) uses only current and past input digital samples to obtain a current output sample value. It does not utilize past output samples. The FIR filter transfer function can be expressed as:

$$H(z) = \frac{Y(z)}{X(z}) = \sum_{n=0}^{N-1} h[n] \cdot z^{-n} \tag{32}$$

The frequency response realized in the time domain is of more interest for FIR filter realization (both hardware and software). The transfer function can be found via the z-transform of a FIR filter frequency response. FIR filter output samples can be computed using the following expression:

$$y[n] = \sum_{k=0}^{N-1} h[k] \cdot x[n-k] \tag{33}$$

where: $x[k]$ are the FIR filter input samples, $h[k]$ are the coefficients of FIR filter frequency response, and $y[n]$ are FIR filter output samples. A good property of FIR filters is that they are less sensitive to the accuracy of constraints than IIR filters of the same order. There are several types of FIR filter realizations including direct, direct transpose, and cascade which are all convenient for the hardware implementation of a filter and is applicable here since the goal is to filter the Eu:LiCAF signal using physical filters [63]

IIR filters are digital filters with infinite impulse response. Unlike FIR filters, they have the feedback and are known as recursive digital filters. IIR filters have much better frequency response than FIR filters of the same order. Unlike FIR filters, their phase characteristic is not linear which can cause a problem to the systems which need

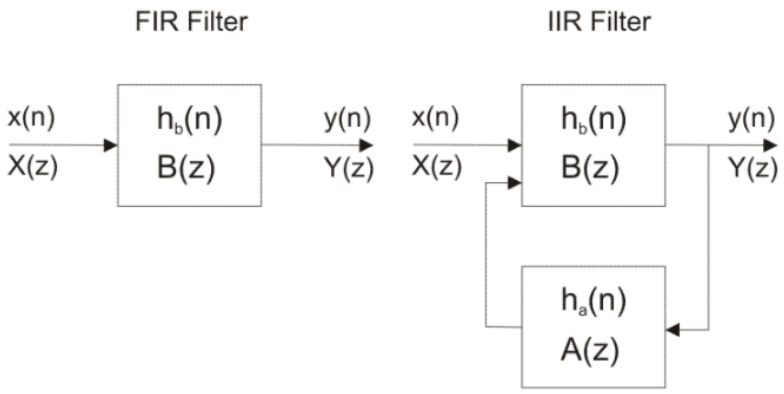

Figure 77. Block diagram of FIR and IIR filters.

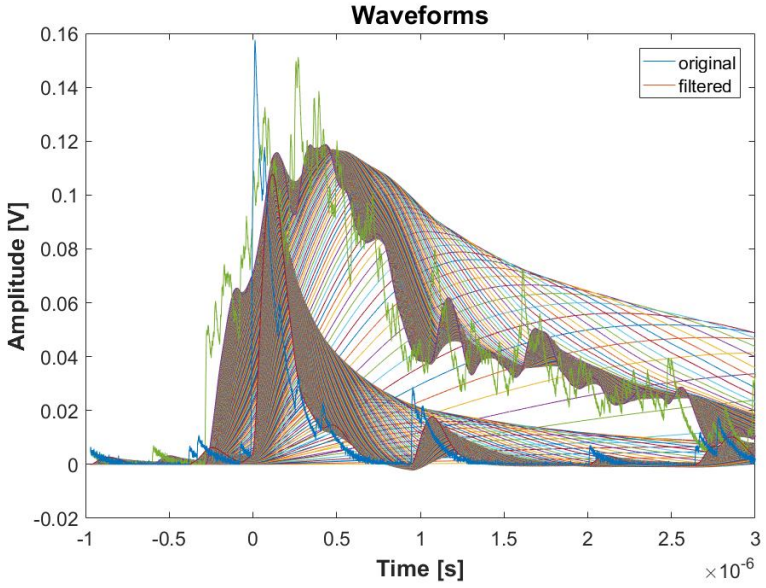

Figure 78. How the cutoff frequency of the low-pass filters affects the shape of the WSF and LiCAF pulses.

phase linearity. Otherwise, when the linear phase characteristic is not important, the use of IIR filters is an excellent solution. For this case, where differentiation of gammas and neutrons is the primary concern, phase is not important. A representation of the two filter types is shown in Fig. 77. Fig. 78 shows how changing the f_c evolves the shape of the two signals.

Appendix M. DD Generator

Because α-particles are the only heavy charged particles with low-Z conveniently available from radioisotopes, reactions involving incident protons, deuterons, and so on must rely on artificially accelerated particles [19]. Two of the most common reactions of this type used to produce neutrons are:

$$^{2}_{1}\mathrm{H} + ^{2}_{1}\mathrm{H} \rightarrow ^{3}_{2}\mathrm{He} + ^{1}_{0}\mathrm{n} + 3.26\mathrm{MeV} \qquad (D + D, 50\%) \tag{34}$$

and

$$^{2}_{1}\mathrm{H} + ^{3}_{1}\mathrm{H} \rightarrow ^{4}_{2}\mathrm{He} + ^{1}_{0}\mathrm{n} + 17.6\mathrm{MeV} \qquad (D + T). \tag{35}$$

Because the coulomb barrier between the incident deuteron and the light target nucleus is relatively small, the deuterons need not be accelerated to a very high energy in order to create a significant neutron yield. These reactions are widely exploited in neutron generators where deuterium ions are accelerated by a potential of about 100-300 kV. Since the incident particle energy is then small compared to the Q value of either reaction, all the neutrons produced have the same energy (near 2.45 MeV for DD and 14 MeV for DT). A 1 mA beam of deuterons will produce about 10^9 n/s from a thick deuterium target and about 10^{11} n/s from a tritium target. Somewhat smaller yields are produced in compact neutron generators consisting of a sealed tube containing the ion source and target, together with a portable high voltage generator [64].

An Adelphi Technology Incorporated DD108 Neutron Generator was used to produce the neutrons for the data collection and validation of the spectrometer. The system is actively vacuum-pumped and uses a continuous trickle supply of non-radioactive deuterium gas. The DD108 works well as a neutron source for testing the spectrometer because the emitted lower-energy neutrons are of the same order

of magnitude as those released by spontaneously fissioning SNM, and it additionally does not produce higher energy neutrons which may be more difficult to shield and moderate.

The system consists of three main parts: the accelerator head, a power supply and control rack, and a separate heat exchanger/chiller. The rack consists of a 2 kW high-voltage power supply running at a maximum of 120 kV with vacuum and gas controlling gauges and interface controls. The entire system is computer controlled by a user-friendly program and has optional capabilities and controls for pulsed operation where a variety of parameters can be selected by the user (pulse length, rise/fall times, dwell time, etc.). The system control unit constantly monitors the system condition and also employs many interlocks for user safety; the interlocks are both mechanical (e.g., on the doors of the generator room) and functional (e.g., if the beam current gets too high) [64]. A few primary specifications of the DD generator, as operated, are shown in Table 5.

Appendix N. Neutron Kinematics

Neutrons react with the detector medium (the moderator or the neutron reactive material) via either elastic or inelastic scattering. A collision is elastic when kinetic energy is conserved and inelastic otherwise. For example, if some of the energy has gone towards modifying the internal state of the 'target', the reaction is inelastic. In the present case, inelastic effects are mostly negligible. The primary mechanism of slowing the neutrons through the hydrogenated neutron moderator is elastic scattering. Elastic scattering has no threshold, which means that it can occur with neutrons of any energy.

Since a neutron has no charge, it can enter into the nucleus and cause a reaction easier than charged particles could (which must be accelerated or heated to very high temperatures). This is where the cross section has a large effect on the detector signal. Simply because the interaction can easily occur does not mean that it has a high probability of occurring. Neutrons interact primarily with the nucleus of an atom except in the special case of magnetic scattering where the interaction involves the neutron spin and the magnetic moment of the atom. The absorption cross section of a neutron with a nucleus is negligible unless it is slowed sufficiently.

The use of highly hydrogenated materials to slow the neutrons to thermal energies is no coincidence. The physics is well known and understood, in fact, the most efficient moderator is hydrogen because a neutron can lose up to all of its energy in a single collision with a hydrogen nucleus [19]. Below is a brief explanation of neutron kinematics. The formulas are quite elementary; however, they accurately describe the motion of a neutron as it scatters from surrounding nuclei. Some necessary symbols are:

A = mass of target nucleus/neutron mass,

E_n= incoming neutron kinetic energy (laboratory system),

E_R= recoil nucleus kinetic energy (laboratory system),

Ψ= scattering angle of the neutron in the center-of-mass coordinate system and

θ= scattering angle of the recoil nucleus in the lab coordinate system.

The laws of elastic collisions can be established using the assumptions of a purely classical mechanical problem. If the incoming neutrons are well below the relativistic speeds ($E_n << 939$ MeV), conservation of momentum and energy define the energy of the recoil nucleus as:

$$E_r = \frac{2A}{(1+A)^2}(1 - cos(\Psi))E_n. \tag{36}$$

To convert to the more familiar laboratory coordinate system in which the original target nucleus is at rest, we use the following transformation:

$$cos(\theta) = \sqrt{\frac{1 - cos(\Psi)}{2}}. \tag{37}$$

Combining Equation (37) with Equation (36) yields a new equation for the recoil nucleus energy in terms of its own angle of recoil:

Table 20. Maximum fractional energy transfer in neutron elastic scattering.

Target Nucleus	**A**	$E_{R,max}$
$^{1}_{1}$H	1	1
$^{2}_{1}$H	2	0.889
$^{3}_{2}$He	3	0.750
$^{4}_{2}$He	4	0.640
$^{12}_{6}$C	12	0.284
$^{16}_{8}$O	16	0.221
$^{208}_{82}$Pb	208	0.019

$$E_R = \frac{4A}{(1+A)^2}(cos^2\theta)E_n. \tag{38}$$

As determined by the dependence on the $cos^2\theta$, a head on collision ($\theta = 0$) of the incoming neutron will lead to a recoil in the same direction resulting in maximum energy transfer:

$$E_{R,max} = \frac{4A}{(1+A)^2}E_n. \tag{39}$$

Table 20 lists the maximum energy that can be transferred to specific target nuclei. As the mass of the target nuclei increases, the maximum amount of energy that can be transferred decreases. This is expected due to the A^{-2} dependence in Equation 39. Notice that the $E_{R,max}$ value for the ${}^{1}_{1}H$ nucleus is 1, meaning that an incoming neutron can potentially transfer all of its energy to the nucleus, immediately thermalizing it.

Many of the response libraries input into the spectrum unfolding code, MAXED, are with respect to lethargy and not neutron energy. Neutron lethargy increases as the neutron slows down, as is appropriate for the name 'lethargy'. This dimensionless quantity is also known as 'logarithmic energy decrement' and is typically denoted u. This is an important concept with neutron moderation because it shows that in order for the neutron to be thermalized it must be contained so that it can 'vibrate' and bleed off its energy. Lethargy is defined as the ratio of the energy of source neutrons to the energy of neutrons after a collision:

$$u = ln\left(\frac{E_0}{E}\right) \tag{40}$$

$$\Delta u = u_2 - u_1 = ln\left(\frac{E_1}{E_2}\right) \tag{41}$$

In a plot of E versus u ($E = E_0 \cdot exp(-u)$), an exponential decay of energy

per unit collision showing that the greatest ΔE of energy results from the early collisions. This is an important concept in neutron spectroscopy because the entire goal is to make the neutron "lethargic" enough and also keep it in the spectrometer so that it can be absorbed. Neutron spectroscopy is effective at determining neutron energy as a result of this concept. If neutrons had a linear energy loss mechanism (as opposed to exponential), it would be much more difficult to resolve the initial energy of the neutron as it would be scattered many times before thermalization. The probability of the neutron significantly deviating from its initial scattering point before being detected by a thermal neutron detector would be much higher. The number of scatters for neutron thermalization was covered in the previous section, however the mechanism behind the energy loss is primarily exponential in behavior. This concept will be further explored and implemented into the future unfolding algorithm. Many Bonner Sphere unfolding codes strictly use neutron lethargy as a "unit". A table showing lethargy of various elements/compounds is shown in Fig 79 [3]. One advantage of using lethargy is that it normalizes the neutrons from 0 to 1. In Lamarsh [3], it is shown that the average lethargy of neutrons after n collisions is equal to $n\xi$. A neutron is said to gain ξ units of lethargy, on average, at each collision. When a neutron moves the distance dx it undergoes, on the average, $\Sigma_s dx$ collisions and its lethargy increases the amount [3]:

$$du = \xi \Sigma_s dx \tag{42}$$

14.1 Age Theory

At energies above 1 eV, the average time required for a neutron to slow from one energy to another by elastic scattering in the moderating region can be done with

Table 6–1

Elastic Slowing-Down Parameters

Nucleus	Mass no.	α	ξ or $\bar{\xi}$
Hydrogen	1	0	1.000
H_2O		*	0.920
Deuterium	2	0.111	0.725
D_2O		*	0.509
Beryllium	9	0.640	0.209
Carbon	12	0.716	0.158
Oxygen	16	0.779	0.120
Sodium	23	0.840	0.0825
Iron	56	0.931	0.0357
Uranium	238	0.983	0.00838

* Not defined.

Figure 79. The elastic slowing-down parameters for various elements/compounds [3].

Age Theory. In the time dt, the lethargy is increased by:

$$du = \xi \Sigma_s v dt. \tag{43}$$

Since $du = -dE/E$,

$$\frac{-dE}{E} = \xi \Sigma_s v dt. \tag{44}$$

Using $E = \frac{1}{2}mv^2$, where m is the mass of the neutron:

$$-\frac{dv}{v^2} = \frac{1}{2}\xi \Sigma_s dt. \tag{45}$$

This can now be used to determine the amount of time a neutron spends in slowing down from an initial speed v_i to the speed v:

$$t = \int_0^t dt = -2 \int_{v_i}^{v} \frac{dv}{\xi \Sigma_s v^2}. \tag{46}$$

In general, both the Σ_s and the ξ, are functions of energy, and hence they are also functions of v. Therefore, an estimate of t can be obtained by replacing Σ_s in the integral by an appropriate average value. Now:

$$t = \frac{2}{\xi \Sigma_s} \left(\frac{1}{v} - \frac{1}{v_i} \right). \tag{47}$$

An estimate is made in Lamarsh, that since the moderated speed is so much smaller than the initial speed of the neutrons (for fission neutrons), the second term in Eqn. 47 can be neglected and the time becomes:

$$t_m = \frac{2}{\xi \Sigma_s v_m}. \tag{48}$$

Just as an approximation, using Eqn. 48, the moderation time (in μs) of H_2O is 1.0 and for graphite, it is 23. This can now be used to obtain a very ballpark figure for the distance that a neutron would travel while it is slowing down to 1 eV. It is, however, a gross overestimate because of the scattering that the neutron undergoes.

The neutron continues to slow down to thermal energies upon reaching 1 eV, however Age Theory is no longer appropriate since Age Theory assumes that the nuclei are free and only down-scattered. The rate at which neutrons slow down decreases as their energy falls below E_m. The thermalization theory will not be covered in depth here, however, the thermalization time can be approximated by [3]:

$$t_{th} = \frac{3\sqrt{\pi}}{2 v_t M_2} \tag{49}$$

where M_2 is the second moment of the scattering kernel and v_t is the speed corresponding to the energy kT. Table 21 shows values for moderation time (t_m), thermalization time (t_{th}), and diffusion time (t_d) for several moderators. Thermal diffusion time is

Table 21. Moderation, Thermalization, and Diffusion Times in μs of Moderators at Room Temperature

Moderator	t_m	t_{th}	t_d
H_2O	1.0	~ 5	210
D_2O	8.1	~ 66	1.4×10^5
Be	9.3	~ 45	3.9×10^3
BeO	12	~ 72	6.7×10^3
Graphite	23	~ 200	1.7×10^4

defined as the average time that a thermal neutron spends in an infinite system before it is captured.

14.2 Neutron Transport

The thermal neutron flux transmitted through the Eu:LiCAF as a function of distance x can be described by [53]: (single energy group, thermal)

$$I(x) = I_0 e^{-x\sigma_F N_F} = I_0 e^{-x\Sigma_F}, \tag{50}$$

where

I_0 is the initial neutron flux,

N_F is the atomic density of the neutron reactive isotope in the film,

σ_F is the microscopic thermal neutron absorption cross-section of the Eu:LiCAF and

Σ_F is the film macroscopic thermal neutron absorption cross-section.

It follows that the fraction of neutrons absorbed in the Eu:LiCAF through distance x is [53]:

$$1 - \frac{I(x)}{I_0} = 1 - e^{-x\Sigma_F}. \tag{51}$$

The neutron absorption probability per unit distance is described by [65]:

$$p(x)dx = \Sigma_F e^{-x\Sigma_F} dx. \tag{52}$$

Appendix O. Scintillation Theory

A simple mathematical model is presented here which gives a good approximation of the charge that can be expected from a single photon. While this model suggests use of a PMT, the silicon photomultiplier is analogous in that it uses microcells for amplification as opposed to dynodes [66].

$$Q = mklR^n e \tag{53}$$

where

m = number of light photons produced in crystal,
k= optical efficiency of the crystal (aka. the efficiency at which the crystal transmits light,
l= quantum efficiency of the photocathode (aka. the efficiency at which the photocathode converts light photons to electrons),
n= number of dynodes (or cascading microcells for SiPMs) and
R= dynode multiplication factor (aka. number of secondary electrons emitted by a dynode per primary electron absorbed).

Bibliography

1. K. Fukuda, "Scintillators Developed by Tokuyama for Neutron Detection Functional Fluoride Group," Tokuyama Corporation, Tech. Rep., 2014.

2. K. Watanabe, T. Yamazaki, D. Sugimoto, A. Yamazaki, A. Uritani, T. Iguchi, K. Fukuda, S. Ishidu, T. Yanagida, and Y. Fujimoto, "Wavelength-shifting fiber signal readout from Transparent RUbber SheeT (TRUST) type LiCaAlF6 neutron scintillator," *Nuclear Instruments and Methods in Physics Research Section A: Accelerators, Spectrometers, Detectors and Associated Equipment*, vol. 784, pp. 260–263, jun 2015. [Online]. Available: https://www.sciencedirect.com/science/article/pii/S0168900214014235

3. J. R. Lamarsh, "Theory of Nuclear Reactors," pp. 1–581, 1972. [Online]. Available: http://scholar.google.com/scholar?hl=en{&}btnG=Search{&}q=intitle:Introduction+to+Nuclear+Reactor+Theory{#}7

4. Tokuyama, "LiCAF for Neutron Detection," Research and Development Division, Tech. Rep., 2016.

5. J. Iwanowska, L. Swiderski, M. Moszynski, T. Yanagida, Y. Yokota, A. Yoshikawa, K. Fukuda, N. Kawaguchi, and S. Ishizu, "Thermal neutron detection with Ce3 doped LiCaAlF6 single crystals," *Nuclear Instruments and Methods in Physics Research, Section A: Accelerators, Spectrometers, Detectors and Associated Equipment*, vol. 652, no. 1, pp. 319–322, 2011.

6. GAO, "COMBATING NUCLEAR SMUGGLING DHS Research and Development on Radiation Detection Technology Could Be Strengthened," Government Accountability Office, Tech. Rep. March, 2015.

7. S. R. Mchale, "THE EFFECTS OF RARE EARTH DOPING ON GALLIUM NITRIDE THIN FILM," Ph.D. dissertation, Air Force Institute of Technology, 2011.

8. M. Woodring, R. Kouzes, M. Demboski, R. Cameron, and J. Magana, "Characterization of the Tokuyama Corporation LiCAF Neutron Detector," Pacific Northwest National Laboratory, Tech. Rep., 2015.

9. S. Lo Meo, P. Bennati, M. N. Cinti, N. Lanconelli, F. L. Navarria, R. Pani, R. Pellegrini, A. Perrotta, and F. Vittorini, "A Geant4 simulation code for simulating optical photons in SPECT scintillation detectors," *Journal of Instrumentation*, vol. 4, no. 7, 2009.

10. E. Dietz-Laursonn, "Peculiarities in the Simulation of Optical Physics with Geant4," 2016. [Online]. Available: http://arxiv.org/abs/1612.05162

11. S. Korpachev and M. Chadeeva, "Geant4 simulation of optical photon transport in scintillator tile with direct readout by silicon photomultiplier," *International Conference on Particle Physics and Astrophysics*, vol. 798, 2017.

12. S. E. Derenzo, M. S. Boswell, E. Bourret-Courchesne, R. Boutchko, T. F. Budinger, A. Canning, S. M. Hanrahan, M. Janecek, Q. Peng, Y. Porter-Chapman, J. D. Powell, C. A. Ramsey, S. E. Taylor, L.-W. Wang, M. J. Weber, and D. S. Wilson, "Design and Implementation of a Facility for Discovering New Scintillator Materials," *IEEE Transactions on Nuclear Science*, vol. 55, no. 3, pp. 1458–1463, jun 2008. [Online]. Available: http://ieeexplore.ieee.org/document/4545106/

13. J. Dolan, M. Marcath, M. Flaska, S. Pozzi, D. Chichester, A. Tomanin, and P. Peerani, "Active-interrogation measurements of fast neutrons from induced fission in low-enriched uranium," *Nuclear Instruments and Methods in Physics Research Section A: Accelerators, Spectrometers, Detectors and Associated Equipment*, vol. 738, pp. 99–105, feb 2014. [Online]. Available: https://www.sciencedirect.com/science/article/pii/S0168900213015933

14. D. a. Shea and D. Morgan, "The Helium-3 Shortage : Supply , Demand , and Options for Congress," *Congressional Research Service*, 2010. [Online]. Available: www.crs.gov

15. L. Viererbl, V. Klupák, M. Vinš, M. Koleška, J. Šoltés, A. Yoshikawa, and M. Nikl, "LiCaAlF 6 scintillators in neutron and gamma radiation fields," *International Journal of Modern Physics: Conference Series*, vol. 44, p. 1660234, 2016. [Online]. Available: http://www.worldscientific.com/doi/abs/10.1142/S2010194516602349

16. R. T. Kouzes, J. H. Ely, A. T. Lintereur, E. K. MacE, D. L. Stephens, and M. L. Woodring, "Neutron detection gamma ray sensitivity criteria," *Nuclear Instruments and Methods in Physics Research, Section A: Accelerators, Spectrometers, Detectors and Associated Equipment*, vol. 654, no. 1, pp. 412–416, 2011. [Online]. Available: http://dx.doi.org/10.1016/j.nima.2011.07.030

17. D. Sugimoto, K. Watanabe, K. Hirota, A. Yamazaki, A. Uritani, T. Iguchi, K. Fukuda, S. Ishidu, N. Kawaguchi, T. Yanagida, Y. Fujimoto, A. Yoshikawa, H. Hasemi, K. Kino, and Y. Kiyanagi, "Neutron TOF Experiments Using Transparent Rubber Sheet Type Neutron Detector with Dispersed Small Pieces of LiCaAlF6 Scintillator," *Physics Procedia*, vol. 60, pp. 349–355, jan 2014. [Online]. Available: https://www.sciencedirect.com/science/article/pii/S187538921400594X

18. R. T. Kouzes, J. R. Ely, A. T. Lintereur, and D. L. Stephens, "Neutron Detector Gamma Insensitivity Criteria," *Pacific Northwest National Laboratory*, vol. PNNL-18903, pp. 1–18, 2009.

19. G. F. Knoll, *Radiation Detection and Measurement*. New York: Wiley, 1979.

20. SensL, "C-Series Low Noise , Fast , Blue-Sensitive Silicon Photomultipliers," SensL Corporation, Tech. Rep., 2014.

21. J. Sæterstøl, "Characterization of Scintillation Crystals for Positron Emission Tomography," no. June, 2010.

22. N. Technology and N. Science, "Characterization of the new scintillator Cs 2 LiYCl 6 :Ce 3+ *," no. 11575145.

23. J. Allison, K. Amako, J. Apostolakis, H. Araujo, P. A. Dubois, M. Asai, G. Barrand, R. Capra, S. Chauvie, R. Chytracek, G. A. P. Cirrone, G. Cooperman, G. Cosmo, G. Cuttone, G. G. Daquino, M. Donszelmann, M. Dressel, G. Folger, F. Foppiano, J. Generowicz, V. Grichine, S. Guatelli, P. Gumplinger, A. Heikkinen, I. Hrivnacova, A. Howard, S. Incerti, V. Ivanchenko, T. Johnson, F. Jones, T. Koi, R. Kokoulin, M. Kossov, H. Kurashige, V. Lara, S. Larsson, F. Lei, F. Longo, M. Maire, A. Mantero, B. Mascialino, I. McLaren, P. M. Lorenzo, K. Minamimoto, K. Murakami, P. Nieminen, L. Pandola, S. Parlati, L. Peralta, J. Perl, A. Pfeiffer, M. G. Pia, A. Ribon, P. Rodrigues, G. Russo, S. Sadilov, G. Santin, T. Sasaki, D. Smith, N. Starkov, S. Tanaka, E. Tcherniaev, B. Tomé, A. Trindade, P. Truscott, L. Urban, M. Verderi, A. Walkden, J. P. Wellisch, D. C. Williams, D. Wright, H. Yoshida, and M. Peirgentili, "Geant4 developments and applications," *IEEE Transactions on Nuclear Science*, vol. 53, no. 1, pp. 270–278, 2006.

24. D. H. Wright, "Geant4 - A Simulation Toolkit," *Research Gate*, no. May 2016, 2002. [Online]. Available: http://www.osti.gov/servlets/purl/799992-t13L8o/native/

25. D. B. Pelowitz, "MCNPX User'S Manual Version 2.6.0," *Los Alamos National Laboratory*, 2008.

26. W. R. Leo, *Techniques for Nuclear and Particle Physics Experiments: A How-to Approach*. Springer Berlin Heidelberg, 2012. [Online]. Available: https://books.google.com/books?id=yc4qBAAAQBAJ

27. SensL, "How to Evaluate and Compare Silicon Photomultiplier Sensors," SensL Corporation, Tech. Rep. October, 2015.

28. M. Foster and D. Ramsden, "A compact neutron detector based on the use of a SiPM detector," *IEEE Nuclear Science Symposium Conference Record*, pp. 1882–1886, 2008.

29. J. B. Mosset, A. Stoykov, U. Greuter, M. Hildebrandt, N. Schlumpf, and H. Van Swygenhoven, "Evaluation of two thermal neutron detection units consisting of ZnS/ 6LiF scintillating layers with embedded WLS fibers read out with a SiPM,"

Nuclear Instruments and Methods in Physics Research, Section A: Accelerators, Spectrometers, Detectors and Associated Equipment, vol. 764, 2014.

30. A. Stoykov, J. B. Mosset, U. Greuter, M. Hildebrandt, and N. Schlumpf, "A SiPM-based ZnS:$ˆ6$LiF scintillation neutron detector," aug 2014. [Online]. Available: http://arxiv.org/abs/1408.6119http://dx.doi.org/10.1016/j.nima.2015.01.076

31. S. Gnecchi and C. Jackson, "A 1 16 SiPM Array for Automotive 3D Imaging LiDAR Systems," *International Image Sensor Society*, pp. 133–136, 2017.

32. SensL, "J-Series High-Density Fill Factor Silicon Photomultipliers," SensL Corporation, Tech. Rep., 2015.

33. C. Thalhammer, "Improving the Light Yield and Timing Resolution of Scintillator-based Detectors for Positron Emission Tomography," 2015.

34. M. Integrated, "General Description Rail-to-Rail I / O Comparators Benefits and Features MAX987 / MAX988 / MAX991 / Rail-to-Rail I / O Comparators Electrical Characteristics (Note 1)," Maxim Integrated, Tech. Rep., 2017.

35. N. Rhodes, "Scintillation Detectors," *Neutron News*, no. 23, p. 26, 2012.

36. Z. Hu, Z. Chen, X. Peng, T. Du, Z. Cui, L. Ge, W. Zhu, Z. Wang, X. Zhu, J. Chen, G. Zhang, X. Li, J. Chen, H. Zhang, G. Zhong, L. Hu, B. Wan, G. Gorini, and T. Fan, "Experimental determination of the response functions of a Bonner sphere spectrometer to monoenergetic neutrons," *Journal of Instrumentation*, vol. 12, no. 6, 2017.

37. Adelphi, "DD108 Neutron Generator Adelphi Technology." [Online]. Available: http://www.adelphitech.com/products/dd108.html

38. Thermo Scientific, "Thermo Scientific MP 320 Lightweight, Portable Neutron Generator Thermo Scientific MP 320 Neutron Generator." [Online]. Available: https://assets.thermofisher.com/TFS-Assets/CAD/Specification-Sheets/D10497{~}.pdf

39. M. A. Ford, B. E. O'Day, J. W. Mcclory, S. K. Manish, and A. Danagoulian, "Evaluation of Eu : LiCAF for neutron spectroscopy using SiPMs and portable electronics," *Nuclear Instruments and Methods in Physics Research Section A: Accelerators, Spectrometers, Detectors and Associated Equipment*, vol. pending, 2018.

40. ORNL, "RSICC Peripheral Science Routine Collection - Monteburns 2.0 - Psr-455," Oak Ridge National Laboratory, Tech. Rep., 2003.

41. M. Reginatto, P. Goldhagen, and S. Neumann, "Spectrum unfolding, sensitivity analysis and propagation of uncertainties with the maximum entropy deconvolution code MAXED," *Nuclear Instruments and Methods in Physics Research, Section A: Accelerators, Spectrometers, Detectors and Associated Equipment*, vol. 476, no. 1-2, pp. 242–246, 2002.

42. M. Reginatto, "Overview of spectral unfolding techniques and uncertainty estimation," *Radiation Measurements*, vol. 45, no. 10, pp. 1323–1329, 2010.

43. J. R. Taylor, *An Introduction to Error Analysis: The Study of Uncertainties in Physical Measurements*, 2nd ed., Ann McGuire, Ed. Sausalito: University Science Books, 1982. [Online]. Available: http://faculty.kfupm.edu.sa/phys/aanaqvi/Taylor-AnIntroductiontoErrorAnalysis.pdf

44. W. L. Goffe, G. D. Ferrier, and J. Rogers, "Global optimization of statistical functions with simulated annealing," *Journal of Econometrics*, vol. 60, no. 1-2, pp. 65–99, jan 1994. [Online]. Available: https://www.sciencedirect.com/science/article/pii/0304407694900388

45. A. Corana, , and M. C. Martini and S. Ridella, "Corrigenda: Minimizing Multimodal Functions of Continuous Variables with the Simulated Annealing' Algorithm," *ACM Transactions on Mathematical Software*, vol. 15, no. 3, p. 287, 1989. [Online]. Available: http://portal.acm.org/citation.cfm?doid=66888.356281

46. M. Reginatto and P. Goldhagen, "MAXED, A Computer Code For the Deconvolution of Multisphere Neutron Spectrometer Data Using The Maximum Entropy Method," US Department of Energy, Tech. Rep., 1998.

47. S. El-Mongy and W. El-Gamal, "Determination of Pu-239 for Nuclear Material Safeguards Verification Purposes," *IEEE Transactions on Nuclear Science*, 1999.

48. K. Krane, *Introductory Nuclear Physics*, 2nd ed. John Wiley and Sons, Inc., 1988.

49. N. N. D. Center, "Chart of the Nuclides," 2017. [Online]. Available: http://www.nndc.bnl.gov/chart/chartNuc.jsp

50. U. D. of Commerce, "National Institute of Standards and Technology," 2017. [Online]. Available: http://www.nist.gov/index.html

51. C. J. Bridgman, *Introduction to the Physics of Nuclear Weapon Effects*, 2001, vol. 2, no. August.

52. J. P. Lestone and E. Shores, "Uranium and Plutonium Average Prompt-fission Neutron Energy Spectra (PFNS) from the Analysis of NTS NUEX Data," *Nuclear Data Sheets*, vol. 119, pp. 213–216, 2014. [Online]. Available: http://www.sciencedirect.com/science/article/pii/S0090375214005936

53. P. Rinard, "Neutron interactions with matter," *Passive Nondestructive Assay of Nuclear Materials, Los Alamos Technical Report NUREG/CR-5550, LA-UR-90-732*, pp. 357–377, 1991. [Online]. Available: https://fas.org/sgp/othergov/doe/lanl/lib-www/la-pubs/00326407.pdf

54. R. J. Hu, J. H. Kim, S. H. Ahn, B. Hong, S. J. Hong, M. Ito, T. I. Kang, B. I. Kim, H. C. Kim, K. B. Lee, K. S. Lee, S. Park, M. S. Ryu, and K. S. Sim, "Characteristics of Boron-Loaded Plastic Scintillators for Neutron Measurements," *Journal of the Korean Physical Society*, vol. 50, no. 95, p. 1482, 2007. [Online]. Available: http://www.kps.or.kr/jkps/abstract{_}view.asp?articleuid=58E6F741-B834-40CE-A1C4-DCAFB6B8C0BD

55. A. N. Caruso, "The physics of solid-state neutron detector materials and geometries." *Journal of physics. Condensed matter : an Institute of Physics journal*, vol. 22, no. 44, p. 443201, 2010.

56. L. Ovechkina, K. Riley, S. Miller, Z. Bell, and V. Nagarkar, "Gadolinium loaded plastic scintillators for high efficiency neutron detection," *Physics Procedia*, vol. 2, no. 2, pp. 161–170, 2009. [Online]. Available: http://dx.doi.org/10.1016/j.phpro.2009.07.008

57. D. S. McGregor, S. L. Bellinger, D. Bruno, W. L. Dunn, W. J. McNeil, E. Patterson, B. B. Rice, J. K. Shultis, and T. Unruh, "Perforated diode neutron detector modules fabricated from high-purity silicon," *Radiation Physics and Chemistry*, vol. 78, no. 10, pp. 874–881, 2009.

58. D. S. McGregor, M. D. Hammig, Y. H. Yang, H. K. Gersch, and R. T. Klann, "Design considerations for thin film coated semiconductor thermal neutron detectors - I: Basics regarding alpha particle emitting neutron reactive films," *Nuclear Instruments and Methods in Physics Research, Section A: Accelerators, Spectrometers, Detectors and Associated Equipment*, vol. 500, no. 1-3, pp. 272–308, 2003.

59. J. Clinton, "Optimization and Characterization of a Novel Self Powered Solid State Neutron Detector by," PhD, Rensselaer Polytechnic Institute, 2011.

60. ——, "Optimization and Characterization of a Novel Self-Powered Solid State Neutron Detector," PhD, Rensselaer Polytechnic Institute, 2011.

61. AIDA, "Abstract Interfaces for Data Analysis," 2001. [Online]. Available: http://aida.freehep.org/index.thtml

62. S. Maeda, H. TOMITA, J. KAWARABAYASHI, and T. IGUCHI, "Fundamental study on neutron spectrum unfolding using maximum entropy and maximum likelihood method," *Progress Nucl Sci Technol*, vol. 1, pp. 233–236, 2011. [Online]. Available: http://www.aesj.net/pnst001/233.pdf{%}5Cnhttp://www.aesj.or.jp/publication/pnst001/data/233.pdf

63. MikroElektronika, "Finite Impulse Response FIR-filter-design-methods MikroElektronika." [Online]. Available: https://www.mikroe.com/ebooks/digital-filter-design/finite-impulse-response-fir-filter-design-methods

64. Adelphi, "DD108 Neutron Generator," Adelphi Incorporated, Tech. Rep., 2012. [Online]. Available: http://adelphitech.com/products/dd108.html

65. C. R. Wuest, "TART Calculations of Neutron Attenuation and Neutron-induced Photons on 5 % and 20 % Borated Polyethylene Slabs," Lawrence Livermore National Laboratory, Tech. Rep., 1992.

66. K. Maher, "Basic Physics of Nuclear Medicine/Scintillation Detectors." [Online]. Available: https://en.wikibooks.org/w/index.php?title=Basic{_}Physics{_}of{_}Nuclear{_}Medicine/Scintillation{_}Detectors{&}oldid=2753422

REPORT DOCUMENTATION PAGE

Form Approved
OMB No. 0704–0188

1. REPORT DATE *(DD–MM–YYYY)*	2. REPORT TYPE	3. DATES COVERED *(From — To)*
28–07–2018	Ph.D. Dissertation	Sep 2015 — Sep 2018

4. TITLE AND SUBTITLE

NEUTRON SPECTROSCOPY
USING RUBBERIZED Eu:LiCAF WAFERS

5a. CONTRACT NUMBER

5b. GRANT NUMBER

5c. PROGRAM ELEMENT NUMBER

6. AUTHOR(S)

Ford, Michael A., Captain, USAF

5d. PROJECT NUMBER

5e. TASK NUMBER

5f. WORK UNIT NUMBER

7. PERFORMING ORGANIZATION NAME(S) AND ADDRESS(ES)

Air Force Institute of Technology
Graduate School of Engineering and Management (AFIT/EN)
2950 Hobson Way
WPAFB OH 45433-7765

8. PERFORMING ORGANIZATION REPORT NUMBER

AFIT-ENP-DS-18-S-024

9. SPONSORING / MONITORING AGENCY NAME(S) AND ADDRESS(ES)

Defense Threat Reduction Agency
POC: MAJ Andrew Decker
(andrew.decker.mil@mail.mil)
2950 Hobson Way
Wright Patterson AFB, OH 45433

10. SPONSOR/MONITOR'S ACRONYM(S)

DTRA

11. SPONSOR/MONITOR'S REPORT NUMBER(S)

12. DISTRIBUTION / AVAILABILITY STATEMENT

Distribution Statement A. Approved for Public Release; Distribution Unlimited

13. SUPPLEMENTARY NOTES

14. ABSTRACT

With the increasing cost and decreasing availability of ^{3}He, there have been many efforts to find alternative neutron detection materials. Lithium calcium aluminum fluoride (LiCAF) enriched to 95% ^{6}Li doped with europium was evaluated here as a replacement material for ^{3}He, based on the absorption of thermalized neutrons by the ^{6}Li and subsequent energy release of the ^{6}Li(n,t)^{4}He reaction. Wafers 0.5 cm thick, consisting of LiCAF crystals in a rubberized matrix, were embedded with wavelength shifting fibers (WSF) and mated to silicon photo-multipliers (SiPMs) to measure the photon response in a flux of neutrons from a DD neutron generator. Excellent discrimination was realized between neutrons and gammas, and both pulse-height discrimination and pulse-shape analysis were explored. A portable ten-layer neutron spectrometer was fabricated from the rubberized wafers and demonstrated that Eu:LiCAF is a promising potential replacement for ^{3}He and shows excellent promise for neutron spectroscopy applications.

15. SUBJECT TERMS

Neutron, Detection, Spectroscopy, Spectrometer

16. SECURITY CLASSIFICATION OF:			17. LIMITATION OF ABSTRACT	18. NUMBER OF PAGES	19a. NAME OF RESPONSIBLE PERSON
a. REPORT	b. ABSTRACT	c. THIS PAGE			COL Buckley O'Day, AFIT/ENP
U	U	U	UU	196	19b. TELEPHONE NUMBER *(include area code)* (937) 255-3636, x4438; buckley.o'day@afit.edu